The Astrophysical Journal, 983:66 (44pp), 2025 April 10 https://doi.org/10.3847/1538-4357/adbbd9

Surveying the Giant H II Regions of the Milky Way with SOFIA. VII. Galactic Center Regions Sgr B1, Sgr B2, and Sgr C

James M. De Buizer[1], Wanggi Lim[2], James T. Radomski[3], and Nicole Karnath[4]
[1] Carl Sagan Center for Research, SETI Institute, 339 Bernardo Avenue, Suite 200, Mountain View, CA 94043, USA; jdebuizer@sofia.usra.edu
[2] IPAC, Mail Code 100-22, Caltech, 1200 East California Boulevard, Pasadena, CA 91125, USA
[3] SOFIA-USRA, NASA Ames Research Center, Mail Stop 232-12, Moffett Field, CA 94035, USA
[4] Space Science Institute, 4765 Walnut Street, Suite B, Boulder, CO 80301, USA
Received 2025 January 9; revised 2025 February 24; accepted 2025 February 27; published 2025 April 7

Abstract

This study examines the mid-infrared properties of Giant H II (GH II) regions in the Milky Way's Central Molecular Zone (CMZ)—Sgr B1, Sgr B2, and Sgr C—using SOFIA-FORCAST imaging at 25 and 37 μm. It compares these mid-infrared data with previous multiwavelength observations to explore their present star formation activity and global properties. The study identifies 77 massive young stellar object (MYSO) candidates in and around the three regions. Sgr B2 appears to host the youngest MYSOs and have much higher extinction than the other regions, containing several radio sources not detected in the mid-infrared even at 37 μm. Meanwhile, cm radio continuum regions of Sgr B1 shows remarkable correspondence to its mid-infrared emission. Sgr C has fewer confirmed MYSOs, and it seems to have a higher fraction of low-mass young stellar objects and contamination from more evolved interloper/foreground stars. Derived MYSO densities are consistent with GH II regions elsewhere in the Galactic plane, though the CMZ GH II regions appear to have less prolific present star formation overall. Unlike Sgr B2, the cm continuum emission in Sgr B1 and Sgr C GH II regions appears to be absent cold dust and molecular gas, suggesting environmental differences, possibly driven by turbulence and rapid dynamical changes near the Galactic center. Furthermore, unlike typical GH II regions, Sgr B1 and Sgr C are significantly ionized by evolved interloper stars, which likely did not form within these regions. In these ways, Sgr B1 and Sgr C deviate from classical GH II region behavior, thus potentially representing a new category of GH II region or challenging their classification as GH II regions.

Unified Astronomy Thesaurus concepts: H II regions (694); Infrared sources (793); Star formation (1569); Infrared astronomy (786); Star forming regions (1565); Massive stars (732); Young star clusters (1833); Protostars (1302)

1. Introduction

Giant H II (GH II) regions are home to extremely massive young and forming OB stellar clusters. They contain a significant fraction of the most massive stars in a galaxy and therefore can dominate a galaxy's thermal emission (F. P. Israel 1980). The study of GH II regions is not only important in understanding and interpreting observations of external galaxies, but they are crucial to the understanding of the formation and evolution of massive stars and their environments.

Massive stars provide critical insights into the processes of stellar evolution. Their strong winds and radiation influence the interstellar medium (e.g., P. S. Conti & R. McCray 1980), triggering star formation (e.g., A. P. Whitworth et al. 1994) and shaping the structure of galaxies (e.g., B. Lee et al. 2013). Understanding how massive stars form and evolve can shed light on the initial mass function and star formation theories. This knowledge helps in understanding the overall population of stars in different galactic environments.

To understand GH II regions and their evolution, as well as their population of presently forming massive young stellar objects (MYSOs), we have embarked on a survey of GH II regions within the Milky Way using observations obtained from the Stratospheric Observatory For Infrared Astronomy (SOFIA) and its mid-infrared instrument FORCAST. The images from FORCAST are the highest spatial resolution (nonsaturated) mid-infrared observations of the entirety of these GH II regions yet obtained at wavelengths beyond $\sim$10 μm (i.e., $\lesssim$3″). Most GH II regions are optically obscured, and radio continuum observations do not have the ability to trace the very earliest stages of massive star formation or nonionizing sources. Furthermore, because of typically high levels of extinction, the extended emissions of the GH II regions—as well as the stars forming within them—are often undetectable at even near-infrared wavelengths. For these reasons, the mid-infrared data from FORCAST are crucial to our analyses.

Our first three papers on W51A (W. Lim & J. M. De Buizer 2019, hereafter Paper I), M17 (W. Lim et al. 2020, hereafter Paper II), and W49A (J. M. De Buizer et al. 2021, hereafter Paper III) covered three of the top eight most powerful GH II regions in the Milky Way and established the analyses that would be applied throughout the rest of the papers in this survey, allowing us to compare and contrast regions effectively. Our previous papers have focused on understanding the massive stellar content of the presently forming generation of stars in GH II regions and trying to understand the internal evolution of the GH II regions as well as their origins.

The original source list for our survey came from P. S. Conti & P. A. Crowther (2004), who performed an analysis of all-sky observations of bright and large cm-wavelength radio continuum sources which they cross-correlated with Midcourse Space Experiment (MSX) mid-infrared imaging data as well as

Infrared Astronomical Satellite (IRAS) data. In order to be classified as a bona fide GH II region (according to P. S. Conti & P. A. Crowther 2004), a source had to have a Lyman continuum photon rate in excess of 10^{50} photons s^{-1} (as derived from its radio continuum emission) and stand out as a bright region in the mid-infrared. In order to try to understand the population of GH II regions as a whole, we wanted to compare and contrast the properties of the most powerful GH II regions (as covered in Paper I–PaperIII) to those that were more modest. In J. M. De Buizer et al. (2022, hereafter Paper IV), we investigated the properties of two GH II regions (Sgr D and W42) that we believed were near the Lyman continuum photon rate cutoff. However, we found out that distance measurements that had been updated since the publication of the P. S. Conti & P. A. Crowther (2004) survey placed both objects much closer to the Earth, disqualifying them from being classified as legitimate GH II regions. Motivated by this, in this same paper we reinvestigated all the GH II regions from P. S. Conti & P. A. Crowther (2004), pouring through the intervening two decades of literature and extracting new data on the distances and electron temperatures of each source. This led to a new updated list of 31 legitimate Galactic GH II regions and 11 candidate GH II regions.

In J. M. De Buizer et al. (2023, hereafter Paper V), we were finally able to properly chose two modest GH II regions just above the 10^{50} photons s^{-1} Lyman continuum photon rate cutoff criteria (DR7 and K3-50) to compare to the most powerful GH II regions of our previous studies. In this work, we discovered that perhaps the biggest difference between GH II regions was not necessarily the Lyman continuum photon rate itself, but the contribution to the overall Lyman continuum photon rate by the presence (or lack) of a revealed stellar OB cluster from an earlier epoch of star formation. Those GH II regions dominated by older OB clusters tended to carve cavities in their host molecular cloud, and the Lyman continuum photons predominantly arise from these ionized cavity walls instead of from internally ionized H II or compact H II regions surrounding nascent massive stellar clusters or individual MYSOs. In light of this, we introduced in J. M. De Buizer et al. (2024, hereafter Paper VI) two GH II morphological types, one characterized by dispersed radio subregions (i.e., "distributed-type") and the other marked by contiguous cavity structures (i.e., "cavity-type"), with both types being most easily discernible in their mid-infrared emission.

That brings us to the present paper, where we have chosen to compare and contrast our previous observations of GH II regions to Sgr B and Sgr C, two regions residing in the Milky Way's Galactic center. Sgr B and Sgr C lie at 100 and 90 pc, respectively, from our Galaxy's supermassive black hole (Paper IV) and exist in an environment quite distinct from the GH II regions farther out in the spirals arms of the Galactic disk. Massive stars forming in GH II regions create swift-moving shock and ionization fronts and produce turbulence from powerful winds and outflows, leading to their classification as "extreme star formation environments." However, the overall environmental conditions in the Galaxy's Central Molecular Zone (CMZ) are even more extreme. Gas temperatures are high in the CMZ ($\gtrsim$50 K; Y. Ao et al. 2013; A. Ginsburg et al. 2016), as are thermal pressures ($\sim 10^{-10}$ erg cm^{-3}; M. Morris & E. Serabyn 1996). With values measured ranging between $\sim$10 μG to $\gtrsim$1 mG, the CMZ is pervaded by a stronger magnetic field than that of the Galactic disk, which is typically $\sim$few μG (A. Mangilli et al. 2019; K. Ferrière 2009). With the addition of tidal forces, shearing forces, crossing orbits from material streams, and much higher overall levels of turbulence in the CMZ, this means that stars forming in these Galactic center GH II regions experience the most extreme conditions anywhere in the Galaxy. These turbulent motions translate to large line widths (i.e., σ) varying from 0.6 to 20 km s^{-1} over size scales of 0.2–2 pc (E. A. C. Mills et al. 2018), which may affect how we can apply our evolutionary analyses that rely (in part) on these values. Additionally, metallicity ($Z_{\odot}$) is higher in the CMZ by almost a factor of two (J. D. Henshaw et al. 2023; D. S. Balser et al. 2011), which affects a GH II region's electron temperature. Therefore, armed with the analysis tools and results from our prior work in this series of papers, our goal in this paper is to investigate the properties of the GH II regions in Sgr B and Sgr C and compare and contrast them to the GH II regions we have studied that exist out in the relatively calm backwaters of our Galaxy.

2. Observations and Data Reduction

The SOFIA data used for this study were originally taken as part of the SOFIA/FORCAST Galactic Center Legacy Survey, and not taken as part of our GH II region observing program. The details regarding the data acquisition, reduction, and calibration are all described in M. J. Hankins et al. (2020). However, the observational techniques and data reduction processes employed on the data were, for the most part, identical to those that we have utilized in all of our GH II survey papers to date (see, e.g., Paper I). That being said, we will highlight below some of observation and reduction details specific to these particular observations.

Data were taken with SOFIA's FORCAST instrument in its dual-channel mode, which utilizes an internal dichroic to simultaneously observe at two mid-infrared wavelengths at once. Unlike the majority of the observations of our GH II region survey, in which data were taken simultaneously at 20 and 37 μm, the Galactic Center Legacy Survey used a setup that took simultaneous data at 25 and 37 μm. The slight wavelength difference between 20 and 25 μm should have no appreciable affect on our analyses or our ability to compare and contrast the results with the other GH II regions we have already studied in our previous papers. The final FORCAST Galactic Center Legacy maps were made by mosaicking individual fields (or "pointings") together. While most fields in our GH II survey had typical exposure times between 180 and 300 s, the Galactic Center Legacy data were typically deeper exposures, varying from 200 to 600 s. The nominal spatial resolutions of the 25 and 37 μm data are 2.″6 and 3.″4, respectively.[5] M. J. Hankins et al. (2020) have stated that the astrometry of the final SOFIA mosaic of the entire Galactic center is at worst $\sim$2″, which is slightly higher than but similar to the quoted astrometric accuracy of our previous GH II region studies (i.e., 1.″5). The slightly higher error is due to the large size of the FORCAST Galactic center mosaic map, as astrometric errors tend to compound for larger mosaics.

Our maps of Sgr B were cropped from the final FORCAST Galactic Center Legacy maps from M. J. Hankins et al. (2020). We had to apply a slight positive flux offset to the cropped

[5] From the FORCAST Handbook for Archive Users, available at IRSA: https://irsa.ipac.caltech.edu/data/SOFIA/docs/instruments/forcast/.

images (15 mJy pixel^{-1} at 25 μm and 13 mJy pixel^{-1} at 37 μm) in order to avoid having multiple areas with negative backgrounds. For Sgr C, additional data were taken as part of that SOFIA/FORCAST Galactic Center Legacy Survey but not incorporated into the final published map. Therefore, for Sgr C, we reduced the data ourselves to create the final image mosaics used in this study, again in a manner very similar to that described in Paper I. Data for Sgr C were combined using the last released public version of SOFIA Redux software.[6] However, all FORCAST data presently in the NASA/IPAC Infrared Science Archive (IRSA) were reduced with a newer version of the software than this. In particular, the last released public version does not contain the latest calibration values (CALFCTR) corrected for precipitable water vapor, so for Sgr C, the values had to be updated based on CALFCTR values from the header keywords in the data in the IRSA archive from when the data was initially processed. All images were obtained by the FORCAST instrument by employing the standard chop-nod observing technique used in ground-based thermal infrared observing, with chop throws of up to 5.′75 and nod throws of up to 7′ in order to be sufficiently large enough to sample clear off-source sky regions uncontaminated by the extended emission of Sgr C. The mid-infrared emitting area of Sgr C was mapped using four pointings. Each of these fields had an average on-source exposure time of between 240 and 400 s at both 25 and 37 μm. The SOFIA Data Pipeline software produced the final mosaicked images (Level 4 data products) from the individual pointings, and these final mosaicked images are presented and used here in this work. For Sgr C, these final mosaics also had their astrometry absolutely calibrated using Spitzer data by matching up the centroids of point sources in common between the Spitzer and SOFIA data using the Aladin Sky Atlas.[7] Absolute astrometry of the final Sgr C SOFIA data is assumed to be better than 1.″5, which is slightly better than the Sgr B astrometric accuracy quoted above. Flux calibration for the Sgr C data was provided by the SOFIA Data Cycle System pipeline, and the final total photometric errors in the images were derived using the same process described in Paper I. It is assumed that the photometric errors are the same for Sgr B and Sgr C, and these errors are discussed more in Section 4.1.

In addition to the SOFIA data, we also utilize science-ready imaging data from the Spitzer Space Telescope and Herschel Space Telescope archives, which we will discuss more in Section 4.1. For Sgr B, we also utilized the 6 cm maps of D. M. Mehringer et al. (1992) and D. M. Mehringer et al. (1995), and downloaded additional 6 cm and 20 cm data from the Very Large Array (VLA) archive, with respective spatial resolutions of 19.″0 and 2.″9. For Sgr C, we used the 6 and 20 cm radio data, also from the VLA archive, which have respective spatial resolutions of 4.″5 and 11.″0.

3. Comparing SOFIA Images to Previous Imaging Observations

As we have done in previous papers in this series, below we will review the (mainly qualitative) comparisons between the SOFIA mid-infrared images and those from prior infrared, radio, and/or submillimeter observations. However, in those previous studies we also dedicated a section that went into detail about each of the individual sources and subregions with each GH II region, using the new and old observations to try to gain a better understanding of the nature of each individual source. Most of those previous papers concentrated on a single GH II region, and since we are covering three GH II regions in this work, we will not cover each at that same level of detail. Below, we discuss the large-scale comparisons of each region and forgo much of the background discussion of individual sources.

3.1. Sgr B

At radio wavelengths, Sgr B is the second-brightest region in the Galactic center, with only Sgr A being brighter (D. I. Jones et al. 2011). Sgr B is composed of two main subregions: Sgr B1 and Sgr B2 (see Figures 1, 2, and 3). The radio continuum emission from Sgr B1 mainly comes from diffuse H II emission from many large and elongated bar-like and shell-like structures, though it does contain a number of modestly bright compact components. Sgr B2, by comparison, is dominated by several dozens of compact H II regions (R. A. Gaume et al. 1995; F. Meng et al. 2022), with only a modest amount of extended radio continuum emission linking them together. D. M. Mehringer et al. (1992) define a third region, G0.6-0.0, which lies between the peaks of Sgr B1 and Sgr B2 (Figures 1, 2, and 3), and displays components with velocities ($v_{lsr} \sim 55$ km s^{-1}) between the average velocities of Sgr B1 and Sgr B2 ($\sim$45 and $\sim$65 km s^{-1}, respectively; D. Downes et al. 1980). In reality, higher-resolution observations, like those of D. M. Mehringer et al. (1992), show that regions like Sgr B1 are made up of multiple concentrations of molecular material with a wide range of velocities (-40 to $+80$ km s^{-1}), which complicates the interpretation. Given the fact that these velocity measurements have similar values and/or have overlapping velocity ranges, the claim by D. M. Mehringer et al. (1992) that G0.6-0.0, Sgr B1, and Sgr B2 are all likely physically related is still valid.

It appears that there is much less extinction toward Sgr B1 than Sgr B2, leading to speculations that Sgr B2 may be located just behind Sgr B1 (J. Bieging et al. 1980) and/or that Sgr B1 is more evolved and has had time to disperse much of its molecular material (D. M. Mehringer et al. 1995). That said, there are more recent claims that Sgr B1 is just behind Sgr B2 (A. I. Harris et al. 2021; J. P. Simpson et al. 2021). Maser activity is thought to be linked to star formation activity, and in agreement with the idea that Sgr B2 is younger than Sgr B1, Sgr B2 harbors much more intense maser activity than Sgr B1 (D. M. Mehringer et al. 1993a).

Sgr B2 has more than twice the 6 cm radio continuum flux of Sgr B1 (53.9 versus 25.5 Jy; D. Downes et al. 1980) and has a slightly larger emitting extent (4.′5 versus 4.′1). Interestingly, however, Sgr B1 is included in our list of bona fide GH II regions (Paper IV) while Sgr B2 is not. This is because our list is a refinement of the compilation of GH II regions made by P. S. Conti & P. A. Crowther (2004), which cross-correlated the all-sky radio continuum surveys of T. A. Kuchar & F. O. Clark (1997) with MSX mid-infrared imaging data at 12 and 22 μm (as well as IRAS data at 25, 60, and 100 μm). Though Sgr B2 is included as a bright radio continuum source in both the T. A. Kuchar & F. O. Clark (1997) and D. Downes et al. (1980) radio surveys, it did not make the cut in the P. S. Conti & P. A. Crowther (2004) compilation of GH II regions. The reason why Sgr B2 specifically was not in their final source list was not reported by P. S. Conti &

[6] https://sofia-usra.github.io/sofia_redux/sofia_redux/index.html
[7] https://aladin.cds.unistra.fr

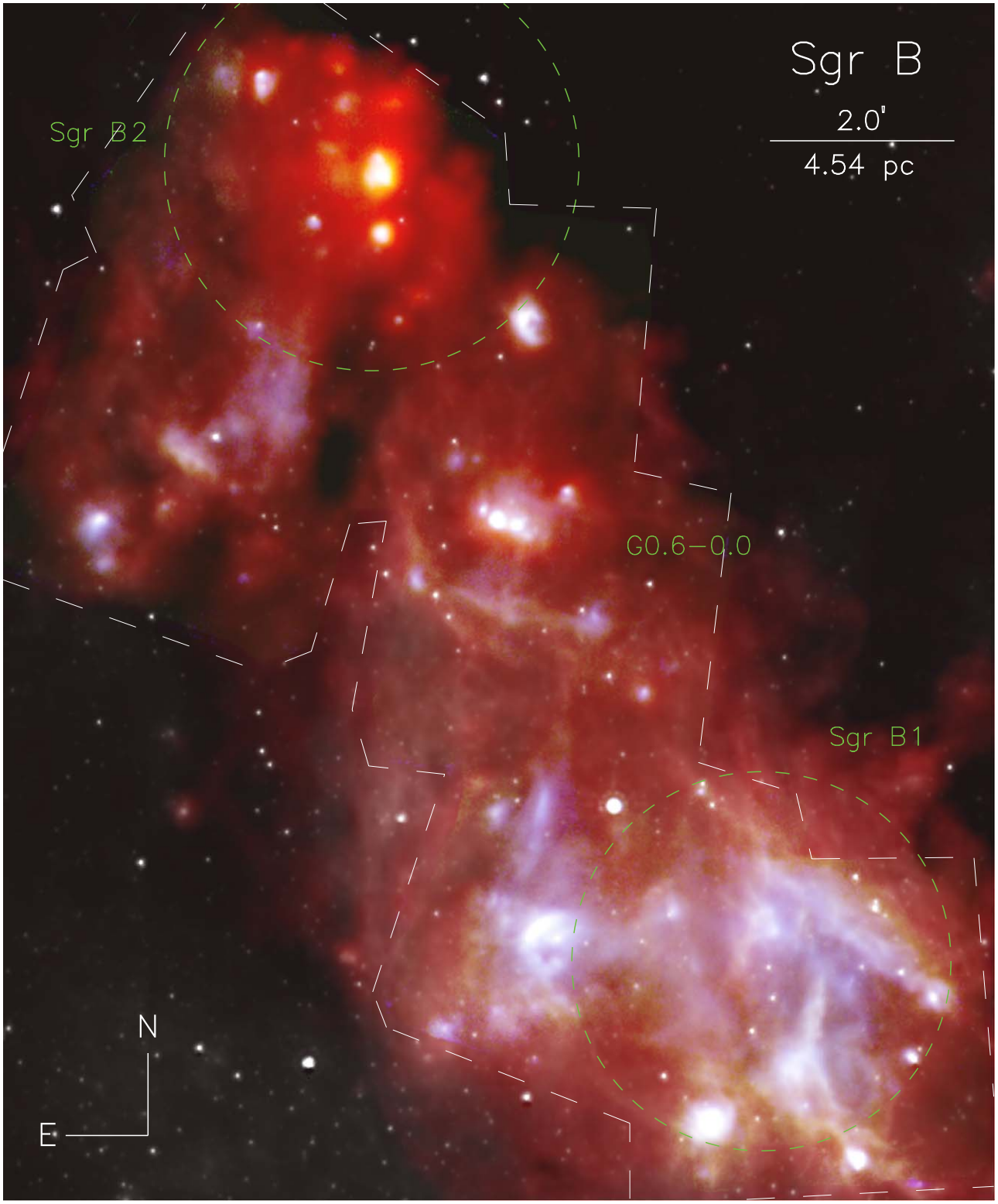

Figure 1. A four-color image of the central ∼10.′8 × 13.′0 (24.5 × 29.5 pc) region of Sgr B. Blue is the SOFIA-FORCAST 25 μm image, green is the SOFIA-FORCAST 37 μm image, and red is the Herschel-PACS 70 μm image. Overlaid in white is the Spitzer-IRAC 8.0 μm image, which traces the revealed stars within Sgr B, field stars, and hot dust. The green dashed circles denote the locations and extent of the Sgr B1 and Sgr B2 H II radio continuum regions as reported in D. Downes et al. (1980). The emission extending between Sgr B1 and B2 is called G0.6-0.0. The white dashed lines denote the areas covered by the SOFIA mid-infrared map.

P. A. Crowther (2004), though it was likely due to Sgr B2's lack of strong and extended infrared emission. In fact, at 22 μm in the MSX images, Sgr B2 is not discernible as an extended infrared region and the total infrared flux of the few detectable sources (510 Jy) within its radio emitting region is 7× fainter than the total infrared flux of Sgr B1 (3550 Jy) within its smaller radio emitting region. However, based upon the radio flux of Sgr B2 alone, we calculate that the Lyman continuum photon rate would be $\log(N_{\rm LyC}) = 51.04 \pm 0.22\,{\rm s}^{-1}$, which would make it tied with G338.398+0.164 (see Paper IV) as the

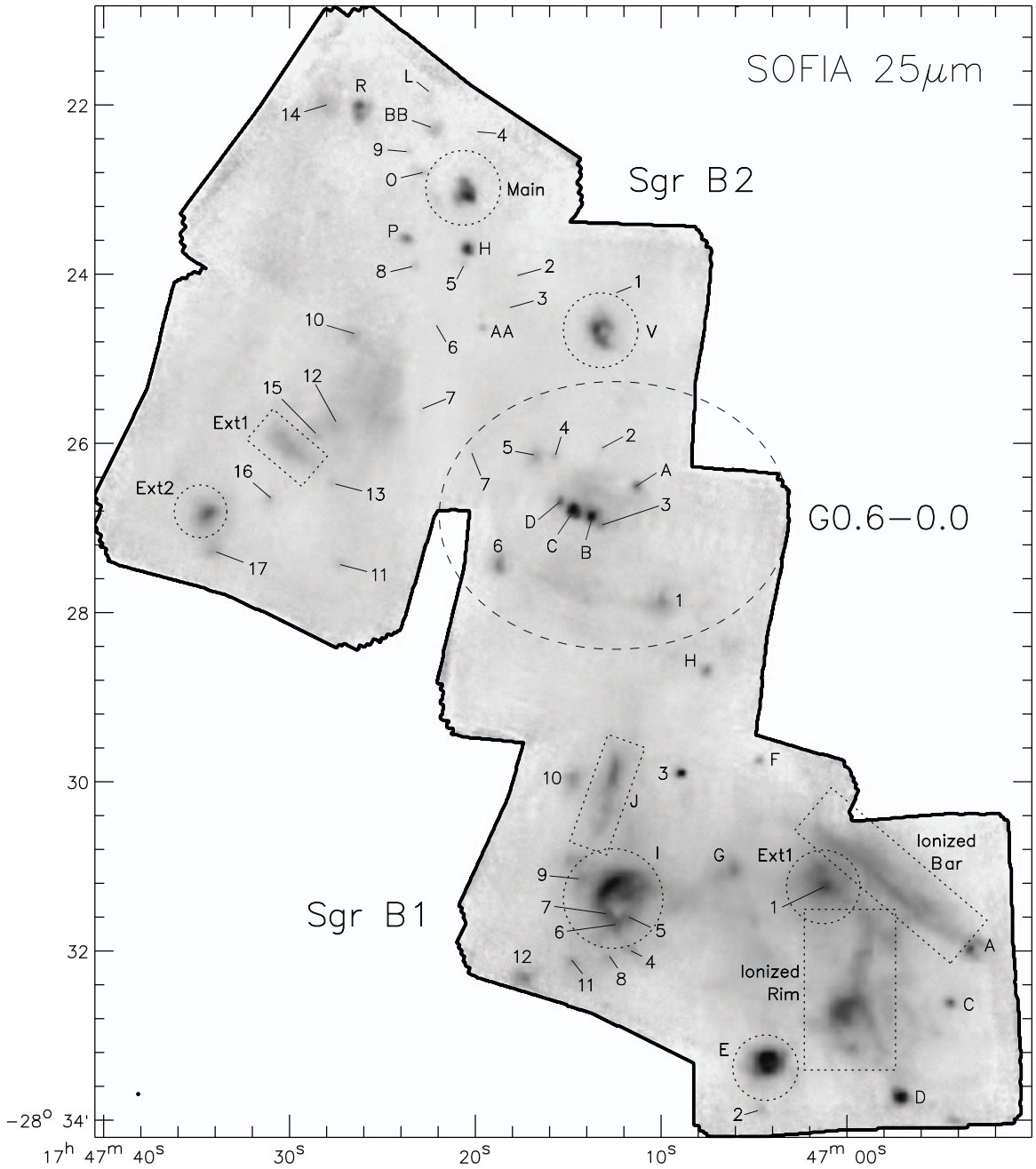

Figure 2. Sgr B image mosaic taken at 25 μm by SOFIA shown in inverse color (i.e., brighter features are darker in color). The locations of radio continuum sources are labeled with letters and are from D. M. Mehringer et al. (1992) and D. M. Mehringer et al. (1993b). Sources labeled with numbers are the mid-infrared compact sources identified in this work. Extended infrared and/or radio sources are encompassed by dotted lines and are labeled in bold. A dashed ellipse surrounds the region known as G0.6-0.0. Sgr B2 lies north and east of this region, and Sgr B1 lies to the south. The black dot in the lower left indicates the resolution of the image at this wavelength.

sixth most powerful GH II region in the Galaxy (Sgr B1 at $\log(N_{\rm LyC}) = 50.87\,{\rm s}^{-1}$ is twelfth). As we will touch on below (and discuss in more detail in Section 4.2.2), we believe that Sgr B2 is likely to be a genuine GH II region, and so we will study it in the same depth as Sgr B1 and Sgr C.

3.1.1. Sgr B1

M. J. Reid et al. (2009) determined the distance to the Sgr B cloud using trigonometric parallax observations of masers, finding a value of $7.8^{+0.8}_{-0.7}$ kpc. Though this distance was actually measured toward Sgr B2 specifically, Sgr B1 and Sgr B2 are believed to be physically related (D. M. Mehringer et al. 1992; J. P. Simpson et al. 2021) since they have similar v_{lsr} velocity ranges, and thus it is assumed here that the maser distance applies to Sgr B1 as well.

D. M. Mehringer et al. (1992) made some of the first high-resolution ($\sim$3″−6″) radio continuum observations of Sgr B1 at 3.6 and 6 cm. Their observations reveal that the radio morphology of Sgr B1 is quite complex, and they identify several elongated and/or ridge-like features, including those they labeled as Ridges 1[8] and 2, the Ionized Bar, and the

[8] Ridge 1 is not covered by our SOFIA maps, and it is a weaker radio continuum feature that lies $\sim$1.2 west of radio source C.

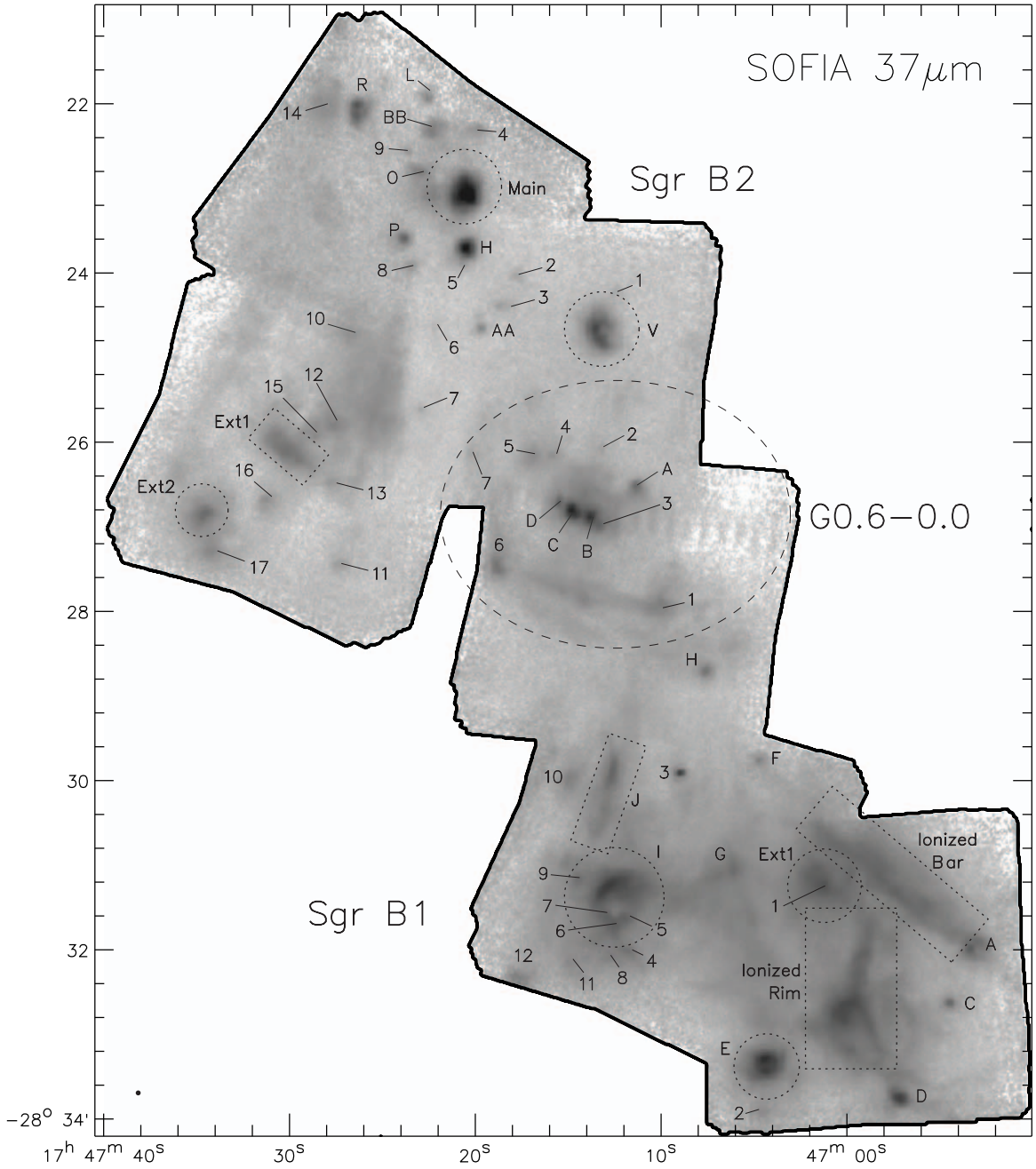

Figure 3. Sgr B image mosaic taken at 37 μm by SOFIA. See caption of Figure 2 for explanation of symbols and figure annotation.

Ionized Rim (see Figure 4). Apart from these large ridge/rims structures, the radio regions E and I appear to be ionized partial shells with diameters of 0.55 and 1.4 pc, respectively. D. M. Mehringer et al. (1992) also point out several compact sources or bright peaks, like A, C, D, and H. Interspersed among these larger structures and compact sources is considerable diffuse, extended radio continuum emission. D. M. Mehringer et al. (1992) claim that roughly 75% of the radio flux density in Sgr B1 comes from the diffuse and extended emission.

As can be seen in Figure 4, the extended radio continuum emission and the extended mid-infrared continuum emission as seen by SOFIA are fairly well-matched, with some minor differences. A couple of the peaks in the radio do not match the peaks seen in the mid-infrared SOFIA data (i.e., sources G and I) and no radio emission is seen at the location of the prominent mid-infrared source Sgr B1 3 (Figure 4). The morphological similarities between radio and infrared emission also extends to the IRAC 5.8 and 8.0 μm imaging data (whereas the emission from Sgr B1 in the IRAC 3.6 and 4.5 μm images is highly extinguished and this area of sky instead appears to be dominated by field stars).

While this correspondence between the radio continuum emission and the mid-infrared is in good agreement, J. P. Simpson et al. (2021) point out that Sgr B1 is "barely noticeable in molecular gas tracers or very cold dust." They also observed that the warm dust emission (as traced by IRAC, SOFIA, and even Herschel 70 μm data) does not seem to be associated with molecular line emission, and therefore Sgr B1 may lack a parent molecular cloud. In particular, they point out

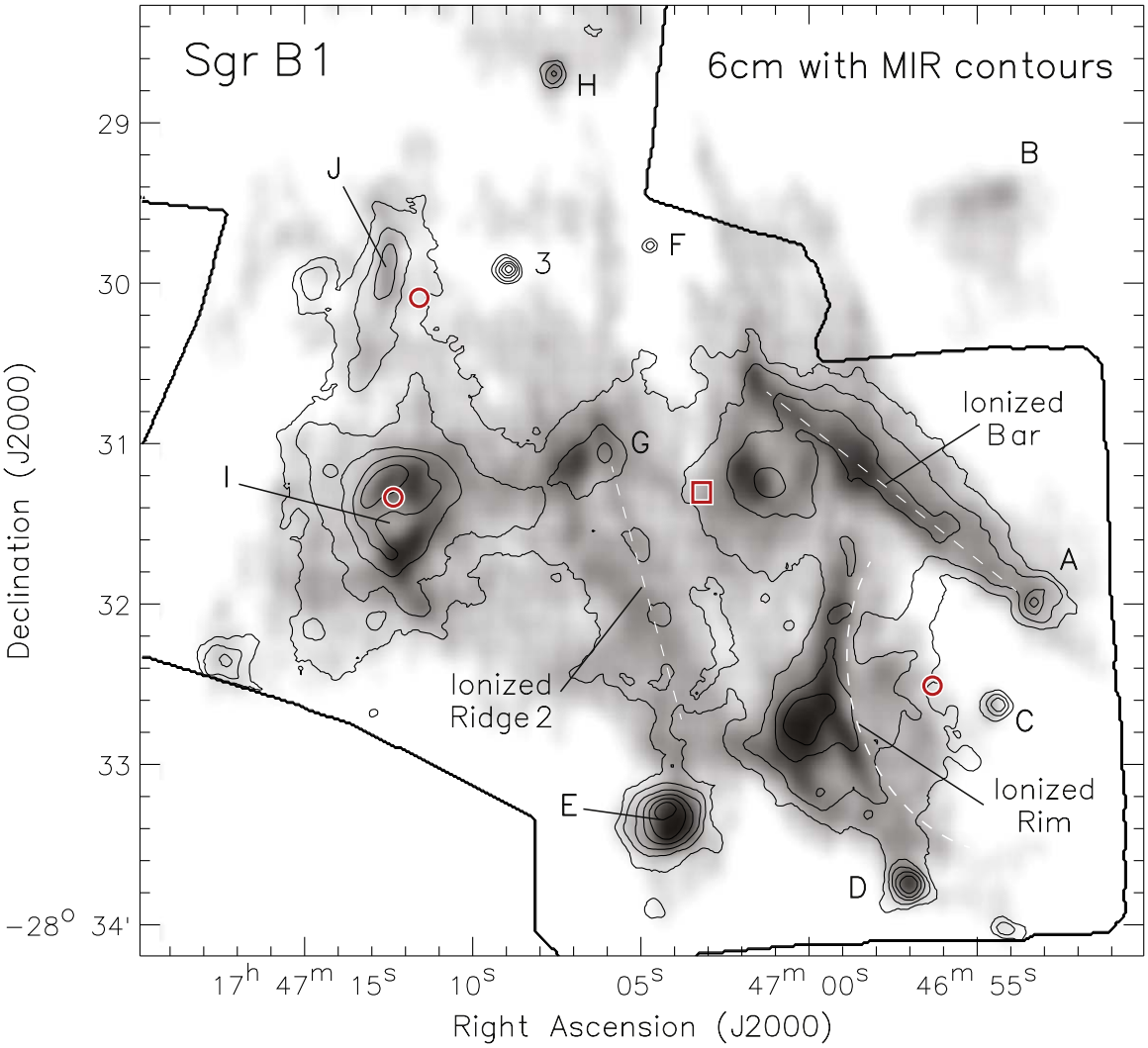

Figure 4. The 6 cm radio continuum image from D. M. Mehringer et al. (1993a) with the SOFIA 25 μm contours overlaid. Labels indicate the Sgr B1 radio sources identified by and discussed in D. M. Mehringer et al. (1992), except for the source marked 3, which is a prominent infrared source with no detectable cm radio emission. The red circles denote the locations of the three Wolf–Rayet stars, and the red square denotes the location of the O supergiant, all of which were identified by J. C. Mauerhan et al. (2010). The dark lines around the 25 μm contours show the field covered by the SOFIA data.

that many of the bright rims and bars within Sgr B1 are not correlated with high-density gas tracers. They therefore deduce that the infrared and radio structures are not tracing dense and optically thick volumes of material, but instead they are likely to appear bright because of a large amount of optically thin material spread out along the line of sight. Consistent with this idea, when looking at the Herschel 160–500 μm data (Figure 5), we see that there are no sources/structures corresponding to those seen in the radio and at wavelengths $\leqslant$70 μm. The 800 μm maps for Sgr B1 and B2 by D. C. Lis & J. E. Carlstrom (1994) are also similar to the Herschel 160–500 μm data and show that, while Sgr B2 has copious submillimeter continuum, Sgr B1 is largely absent in the map. Furthermore, the ^{13}CO maps by Y. Sofue (2024) paint the picture of Sgr B1 existing within the center of a bubble of molecular material.

That being said, Sgr B1 is not completely devoid of molecular gas, as there are still modest levels present that allow something of its molecular nature to be discerned. For instance, D. M. Mehringer et al. (1995) say that, although much of the molecular gas in Sgr B1 appears to have dispersed, their observations of formaldehyde in absorption show that some of the ionized material on the eastern side of Sgr B1 is more distant than that on the western side.

3.1.2. Sgr B2

There is some minor uncertainty about the distance to Sgr B2. As stated above, we adopted the value of $7.8^{+0.8}_{-0.7}$ kpc, which comes from the maser parallax and proper motion studies of M. J. Reid et al. (2009). In that work, they also claim that Sgr B2 is $\sim$130 pc closer to Earth than Sgr A*. This result is consistent with other more recent studies that also place Sgr B2 in front of Sgr A* (J. M. D. Kruijssen et al. 2015; M. G. L. Ridley et al. 2017). However, T. Oka & T. R. Geballe (2022) claim that Sgr B2 lies $\sim$90 pc farther away than Sgr A*, based upon spectroscopic measurements. As these differences are all within the margin of error of the trigonometric parallax observations, and since these relatively small distance differences do not considerably change the assessments we are making in this study, we will use the 7.8 kpc value here.

The first high-angular resolution radio continuum maps ($<1''$) produced of the Sgr B2 region were from J. M. Benson & K. J. Johnston (1984), who observed the region at 2 and

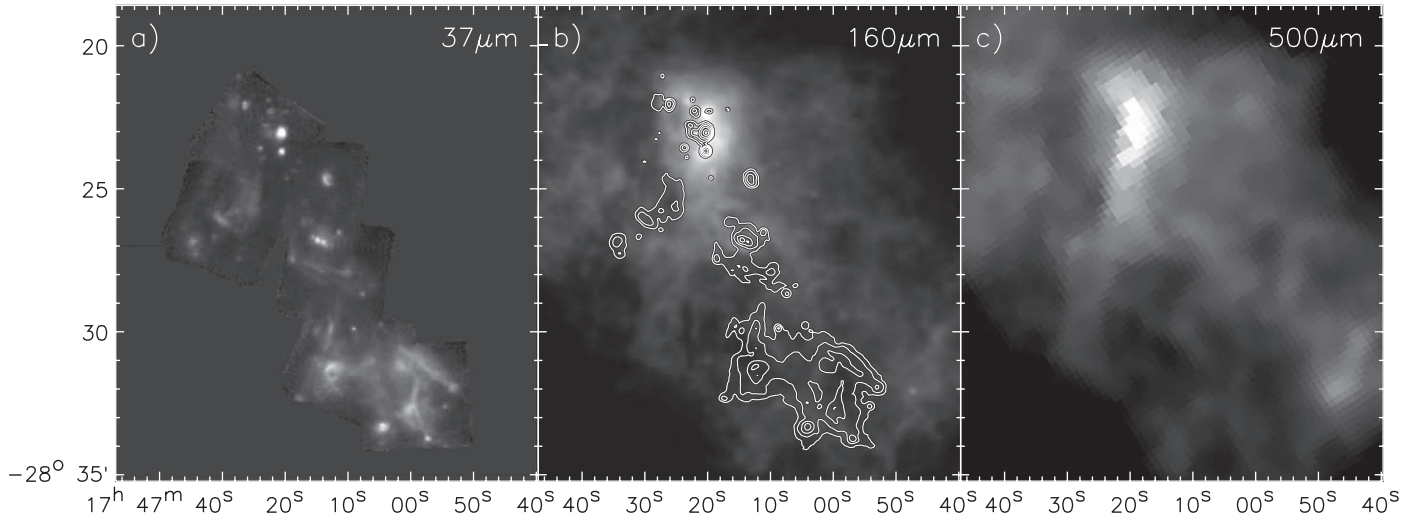

Figure 5. Sgr B region at (a) 37 μm, (b) 160 μm (with 37 μm contours), and (c) 500 μm. The morphology of Sgr B appears very similar to the 37 μm image for wavelengths from 8 to 70 μm. The morphology is also very similar from 160 to 500 μm, but very different than the morphology from 8 to 70 μm. Most of the emitting regions seen at 37 μm appear to be devoid of cold dust at 160–500 μm, except for the central region of Sgr B2. In particular, the entire Sgr B1 GH II region appears to have no 37 μm emission source or feature that is also emitting at 160 μm or longer.

6 cm. They identified the radio sources A–L, and they were able to resolve Sgr B2 Main into multiple compact radio components for the first time. This work and the later work of R. A. Gaume & M. J. Claussen (1990) established the radio emission in Sgr B2 as coming from many compact H II regions. Most recently, F. Meng et al. (2022), using subarcsecond 5 cm imaging, found 54 ultracompact H II regions in the central $4' \times 4'$ of Sgr B2. In the central 2 pc of Sgr B2, there are two well-known and well-studied hot cores, Sgr B2 Main and Sgr B2 K (a.k.a. Sgr B2 North in more recent studies), which F. Meng et al. (2022) claim contain at least 70 high-mass stars with spectral types from B0 to O5. These two cores are embedded in a larger molecular clump ~40 pc in diameter that contains 99% of the mass of Sgr B2. Indeed, the first ~1′ observations at far-infrared to millimeter wavelengths (50 and 100 μm from P. M. Harvey et al. 1977 and I. Gatley et al. 1978; 1 mm from W. E. Westbrook et al. 1976), as well as molecular lines (^{13}CO from N. Z. Scoville et al. 1975) show a similarly shaped north–south elongated clump present here, centered near the position of Sgr B2 Main. Recently, at 3 mm using ALMA with ~0.″5 resolution, A. Ginsburg et al. (2018) identified 271 compact cores across Sgr B2. Though F. Meng et al. (2022) claim that there is no direct evidence of the existence of high-mass stars embedded in these 3 mm cores, we do find two of them to coincide with SOFIA mid-infrared sources (Sgr B2 4 and Sgr B2 5). However, as pointed out by F. Meng et al. (2022), the reason for such a low detection rate in the infrared may be the high levels of extinction present.

In Figure 6, we present the 20 cm radio continuum image from D. M. Mehringer et al. (1993b) with the SOFIA 37 μm contours overlaid. Like the case for Sgr B1, we see that there is generally good morphological agreement between the two wavelengths, but there are several exceptions. Extinction appears to be extremely high to the west of Sgr B2 Main, and we do not see mid-infrared emission from prominent radio sources like K, U, W, Y, and Z. We also see that the diffuse radio continuum emission region south of AA (referred to as Sgr B2 Deep South, or DS, in recent studies; e.g., A. Ginsburg et al. 2018) is not present in the mid-infrared, and the diffuse mid-infrared region east of it has no radio continuum emission. A possible factor contributing to the nondetection of mid-infrared emission from Sgr B2 DS is that F. Meng et al. (2019) show the region to have widespread and diffuse nonthermal radio emission, which M. Padovani et al. (2019) claim may be due to thermal electrons getting accelerated up to relativistic energies within the H II region. Modest radio continuum emission is present at the locations of Sgr B2 Ext1 and mid-infrared source Sgr B2 17. Sgr B2 V also looks similar at both wavelengths; however, as pointed out by D. M. Mehringer et al. (1995), it exhibits a significantly higher velocity ($+99$ km s^{-1}) compared to the 55–80 km s^{-1} velocities observed in the rest of Sgr B2, suggesting that it is likely not directly associated with the region.

At 160–500 μm, the region centered approximately on Sgr B2 Main and having a radius of 1.′5 appears very similar to the radio (and mid-infrared) morphologically. At wavelengths of 350 μm and longer, the radio region south of AA, Sgr B2 DS, begins to appear as well. This colder material running north–south at this location is designated as an infrared dark cloud (IRDC) by F. Yusef-Zadeh et al. (2024). It runs through the region occupied by the diffuse radio region south of AA and runs north, passing to the west of Sgr B2 Main. This extended cold dust structure is also seen in the 1.3 mm observations of D. C. Lis et al. (1991), which displays two prominent peaks near Sgr B2 K and Sgr B2 Main with emission extending ~1.′3 north of K, and ~3.′3 south of Sgr B2 Main. At 160–500 μm, there is no apparent emission from mid-infrared regions Sgr B2 Ext1 and Sgr B2 Ext2, signifying that these sources lack cold dust and possibly dense molecular material (analogous to most of Sgr B1).

In the Spitzer IRAC data, at 8 μm, we see evidence of the IRDC (due to the lack of emission), and the majority of what is visible at this wavelength is from scattered diffuse emission and sources east of the IRDC location. That being said, some emission is seen coming from Sgr B2 Main, as well as H, BB, O, P, and R. Most of the sources seen at SOFIA wavelengths (including Sgr B2 Main) have emission components at the shorter 3.6 and 4.5 μm wavelengths, signifying either a steep change in extinction across the Sgr B2 region from west to east or that these sources lie just in front of the IRDC.

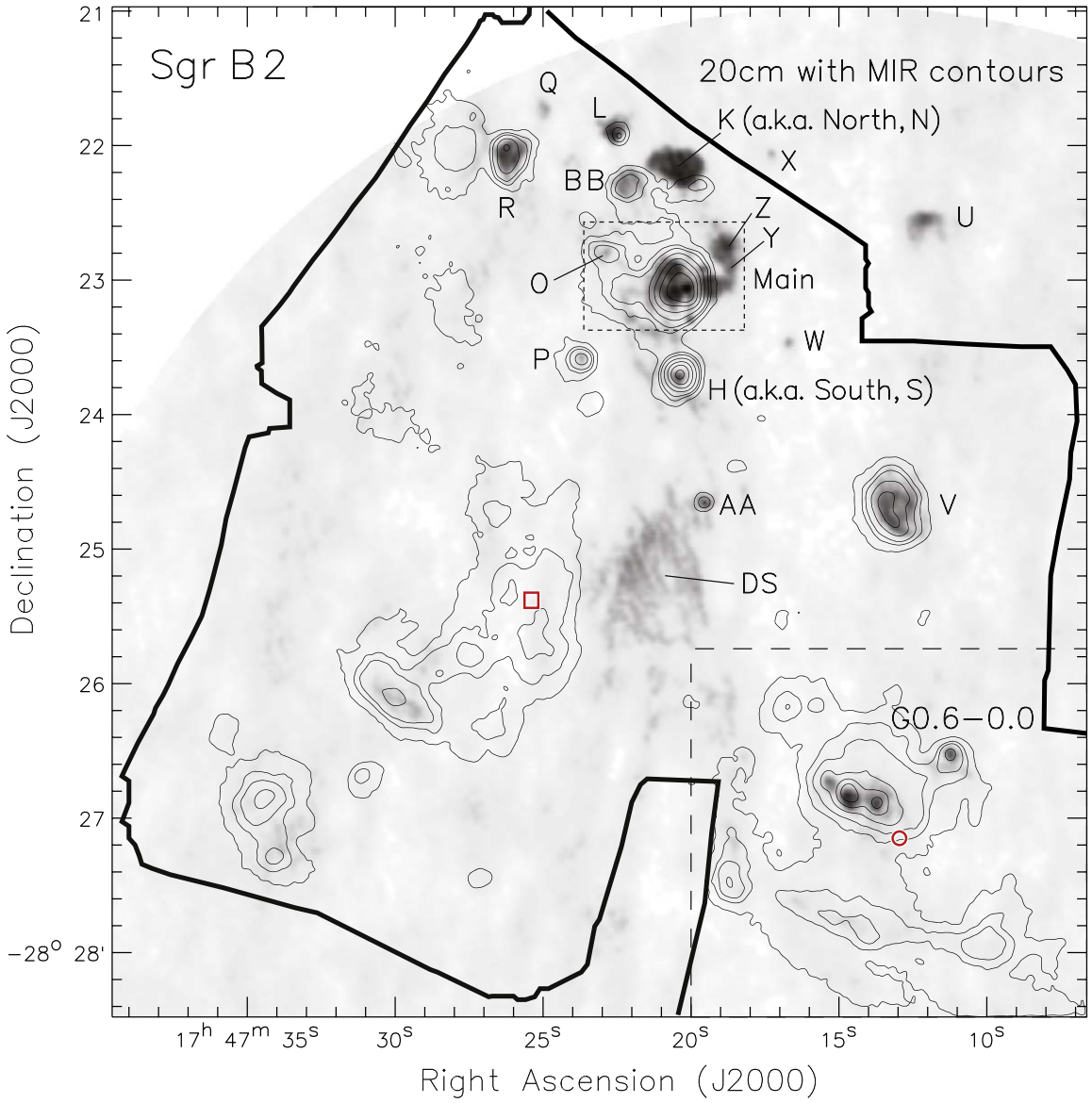

Figure 6. The 20 cm radio continuum image from D. M. Mehringer et al. (1993b) with the SOFIA 37 μm contours overlaid. Labels indicate the Sgr B2 radio sources identified by and discussed in D. M. Mehringer et al. (1993b). The dark lines around the 37 μm contours show the field covered by the SOFIA data. The dotted region is Sgr B2 Main, which itself is broken up into many smaller radio sources, but all of them are either unresolved or undetected in the SOFIA data. The region designated G0.6-0.0 is encompassed in the dashed area of the lower right of the image. The red circles denote the locations of the Wolf–Rayet star in G0.6-0.0, and the red square denotes the location of the O supergiant in Sgr B2, both taken from J. S. Clark et al. (2021).

F. Yusef-Zadeh et al. (2009) further points out that Sgr B2 has the highest density of sources in the Galactic center with excess emission in the IRAC 4.5 μm band (a.k.a. extended green object, or EGO, emission), and this emission tends to be directly associated with high-mass star formation (C. J. Cyganowski et al. 2011; J. M. De Buizer & W. D. Vacca 2010).

3.2. Sgr C

There are three main components to Sgr C: a ~10 pc H II region, an infrared dark cloud, and a prominent nonthermal radio filament. As pointed out by S. Kendrew et al. (2013), Sgr C is the only known star-forming region in the western CMZ. Nonetheless, there are relatively few studies dedicated to Sgr C at any wavelength. Save for a few studies concentrating on radio emission from Sgr C, most data that cover Sgr C are included in studies of the entire CMZ of the Galactic center.

Sgr C was first mapped in the infrared at 100 μm by W. F. Hoffmann et al. (1971) at 6′ resolution, and then identified as an H II region at 3 and 6 cm radio continuum with $\lesssim$1.3′ resolution by D. Downes et al. (1979). Much higher spatial resolution radio continuum observations of Sgr C were made by H. S. Liszt & R. W. Spiker (1995), at 18.5 cm with ~5″ resolution, resolving the structure of the H II region and its nearby ionized environment.

In the infrared, I. Gatley et al. (1978) imaged Sgr C at 30, 50, and 100 μm, and showed that the emission peaks at wavelengths shorter than 100 μm. This was later confirmed by ISO spectra (E. Peeters et al. 2002), which showed a peak in brightness for Sgr C at ~50 μm, falling drastically to relatively small flux values by 150 μm. Extremely low-resolution (4′) images of the entire CMZ were obtained using the IRAS Satellite at 12, 25, 60, and 100 μm (T. N. Gautier et al. 1984;

P. Cox & R. Laureijs 1989), where Sgr C can clearly be seen at all wavelengths, and S. J. Little & S. D. Price (1985) obtained at 4–27 μm observations of Sgr C using rocket-borne instruments with $\sim$3.′5 resolution. The first subarcminute infrared images of Sgr C were the MSX data presented in P. S. Conti & P. A. Crowther (2004). Spitzer images with $\sim$3″ resolutions have been presented of Sgr C, again in images showing the whole of the CMZ, e.g., by F. Yusef-Zadeh et al. (2009) and C. M. Koepferl et al. (2015), in which it is hard to see details. Very recently, S. Crowe et al. (2024) have published James Webb Space Telescope (JWST) NIRCam observations of Sgr C, creating subarcsecond images from 1 to 5 μm that cover most, but not all, of the GH II region. In a contemporaneous companion paper, J. Bally et al. (2024) present JWST-NIRCam Br α images, that show exquisite detail within the large ($r \sim 1'$) Sgr C H II region and reveal that it is pervaded with filamentary structures. In our SOFIA 25 and 37 μm images at $\sim$3″ resolution (Figures 7, 8, and 9), we see the dominant emission is from the Sgr C H II region, which appears clumpy in our images. The overall morphology and size of the Sgr C H II region appears very similar to the cm radio continuum emission (Figure 10), conspicuously bending around but avoiding the location of the IRDC. Several fainter infrared sources lie spread through the rest of our SOFIA field, including in a region $\sim$3.′5 south of the Sgr C H II region that we call G359.38–0.08, another region $\sim$4.′0 to the west that we call G359.42–0.02, and yet another region $\sim$4.′2 to the northeast that we call G359.50-0.09 (Figures 7, 8, and 9).

D. C. Lis et al. (1991) observed Sgr C at 1.3 and 0.8 mm with 0.5′ resolution, and they were likely the first to isolate and resolve the IRDC component. This IRDC is also the dominant feature in the 350 μm observations of J. Staguhn et al. (2004). The location of the H II region, however, appears to be devoid of cold dust traced by these wavelengths, in agreement with the conclusions of I. Gatley et al. (1978) who, based upon the low measured far-infrared optical depths, claimed that the Sgr C H II region is not embedded in a dense molecular cloud. This is further backed by a host of data from molecular lines, such as CS (C. Kramer et al. 1998; P. A. Jones et al. 2013) and ^{13}CO (H. S. Liszt & R. W. Spiker 1995). Like Sgr B1, when we look at Herschel imaging data tracing the location of cold dust, we once again see that the mid-infrared and radio emitting regions lie in far-infrared emission voids at wavelengths $\gtrsim$160 μm (Figure 11).

The vast majority of the present star formation appears to be going on in or near the IRDC (Figures 8, 9, and 11). The IRDC is shaped like a finger that protrudes into the side of the H II region from the east. S. Kendrew et al. (2013) speculate that the enhanced star formation at this specific location in the IRDC may be due to it being close to the interface of a cloud–cloud collision or feedback from the H II region. The western tip of the IRDC is rich in tracers of present star formation. The subarcsecond radio continuum observations of J. R. Forster & J. L. Caswell (2000) were the first to find a UCH II region here (G359.436-0.102; see Figure 10) coincident with H_2O maser emission, as well as nearby OH masers (to within $\sim$3″). Additional intense maser activity has been found by others, including X. Lu et al. (2019a), who find CH_3OH and H_2CO masers here. They argue that H_2CO masers are thought to trace a very short period in high-mass star formation, and the occurrence of these masers in Sgr C means there is an ongoing burst of star formation. They further state that Sgr C is one of the most maser-rich sites in the entire Galaxy. Additionally, the tip of this IRDC is now known to house as many as 19 millimeter cores (S. Kendrew et al. 2013; X. Lu et al. 2019a) and several UCH II regions (X. Lu et al. 2019b). X. Lu et al. (2020), X. Lu et al. (2021) also found multiple mm cores and molecular outflows from sources throughout the IRDC using data obtained with ALMA. Furthermore, F. Yusef-Zadeh et al. (2009) showed with IRAC data that there was 4.5 μm EGO emission at the location of the stars forming in the tip of the IRDC. Again, this EGO emission is thought to be a tracer of predominantly massive star formation, and S. Crowe et al. (2024) interpret this entire region as a blueshift outflow lobe. In our SOFIA data, this IRDC appears as a bright region in the reverse intensity of Figures 8 and 9, and we clearly detect several of the UCH II regions present in the tip of the IRDC.

Despite all of the evidence for star formation occurring in Sgr C, the present generation of star formation is predominantly confined to the IRDC. Consequently, S. Kendrew et al. (2013) claim that, when looking at the whole Sgr C region, it appears to be relatively inactive compared to Galactic disk molecular clouds that exhibit similar physical conditions. However, F. Yusef-Zadeh et al. (2009) found several point sources throughout the Sgr C region using Spitzer-MIPS 24 μm imaging data, and claimed that they were YSO candidates. Based upon their infrared spectra, several of these sources were later ruled out as YSOs by D. An et al. (2011), and C. M. Koepferl et al. (2015) speculated that many could be main-sequence stars in a high-extinction environment. Further analysis by F. Yusef-Zadeh et al. (2022) found four YSOs in Sgr C. However, two are only seen in Spitzer-IRAC data (i.e., not in MIPS 24 μm), and all four lie off our covered SOFIA field. We find several sources that are MYSO candidates in the SOFIA data in and around the Sgr C H II region, which we will discuss further in Section 4, as well as others in G359.38-0.08, G359.42-0.02, and G359.50-0.09, which are presented in Appendix C.

Unsurprisingly, the majority of the prominent nonthermal radio filament does not radiate emission at any infrared wavelength we studied. The exceptions may be Sgr C 6 and Sgr C 15 (and perhaps also Sgr C 16) just north of the Sgr C H II region and some faint extended emission in between them (see Figure 10), which appear coincident with the location of the nonthermal filament. Since detectable infrared emission is not expected from nonthermal radio filaments, these two infrared sources and/or the extended faint emission seen at 25 and 37 μm, may be indicating an interaction between the filament and the H II region.

Unfortunately, unlike Sgr B2, we do not have any parallactic or other high-precision distance measurements directly of Sgr C. As pointed out by S. Kendrew et al. (2013), the v_{lsr} of Sgr C is very similar to those of sources in the Near 3 kpc Arm at a distance of $\sim$5.5 kpc, which complicates kinematic interpretations of its distance. That being said, measured v_{lsr} values, like those (-60.0 ± 1.0 km s^{-1} from the measured H109α+H110α transitions) of J. L. Caswell & R. F. Haynes (1987) yield tangent point kinematic distances of $8.34^{+0.15}_{-0.17}$ kpc (Paper IV). Historically, Sgr C has been assumed to be at the same distance as Sgr A*, and interestingly, the distance to Sgr C just quoted agrees with more rigorous calculations of the distance to the Galactic center of $R_o = 8.34 \pm 0.16$ kpc by M. J. Reid et al. (2014). We adopt the 8.34 kpc value here for Sgr C.

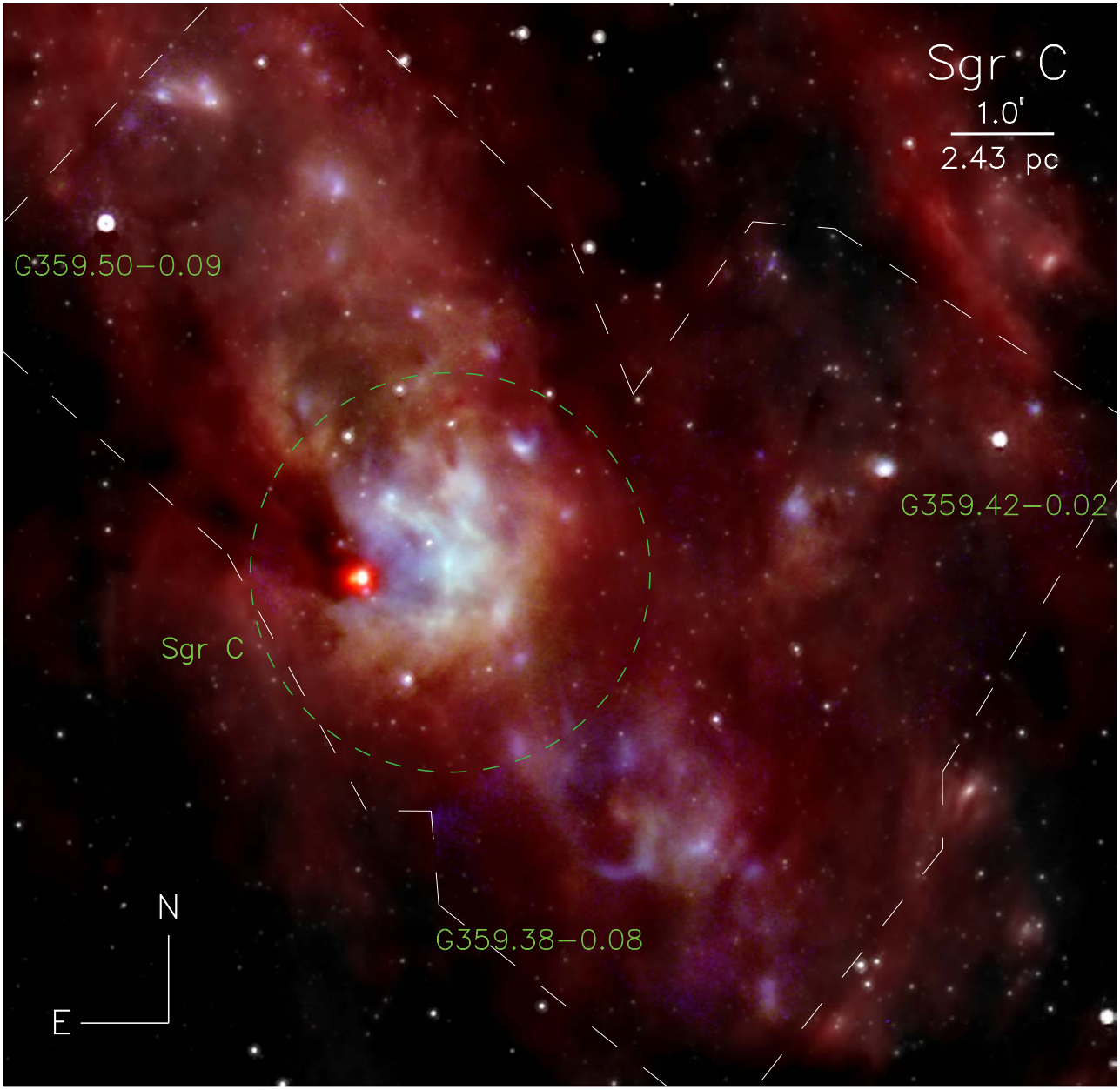

Figure 7. A four-color image of the central ∼10.′4 × 10.′1 (25.3 × 24.5 pc) region of Sgr C. Blue is the SOFIA-FORCAST 25 μm image, green is the SOFIA-FORCAST 37 μm image, and red is the Herschel-PACS 70 μm image. Overlaid in white is the Spitzer-IRAC 8.0 μm image, which traces the revealed stars within Sgr C, field stars, and hot dust. The green dashed circle denotes the location and extent of the H II radio continuum region as reported in D. Downes et al. (1980). The white dashed lines denote the areas covered by the SOFIA mid-infrared map.

4. Data Analysis and Results

As we have done in our other papers in this survey, we classify the infrared emission sources within the GH II regions of our survey into two groups: compact sources and extended subregions. The compact sources are believed to be star-forming cores (typically $\lesssim$0.3 pc in size), while the extended subregions are thought to be larger star-forming molecular clumps. As we have done previously for the compact sources, we will fit SED models to their multiwavelength photometry to estimate their physical properties and identify potential MYSOs.

For the extended subregions, our ability to follow what we have done in our previous papers breaks down. Previously, we have assessed the evolutionary state of each subregion by measuring both their luminosity-to-dust mass (L/M) ratio (derived from the infrared SEDs of the radio/mid-infrared subregions), as well as the virial parameter of their gas components from ^{13}CO data. However, as we have mentioned briefly in the discussion of Sgr B1 and Sgr C in Section 3, while the cm radio continuum and infrared at wavelengths $<$160 μm match in morphology, none of these features appear to have cold dust (250–500 μm) or definitive molecular CO components. For these reasons, we cannot apply the same L/M and virial analyses to these GH II regions. In our previous papers, extended sources had their 3–160 μm photometry reported along with the descriptions of their evolutionary analyses; however, in this paper, since we will not be performing those analyses, we chose to list the extended source photometry at these wavelengths in the same tables as

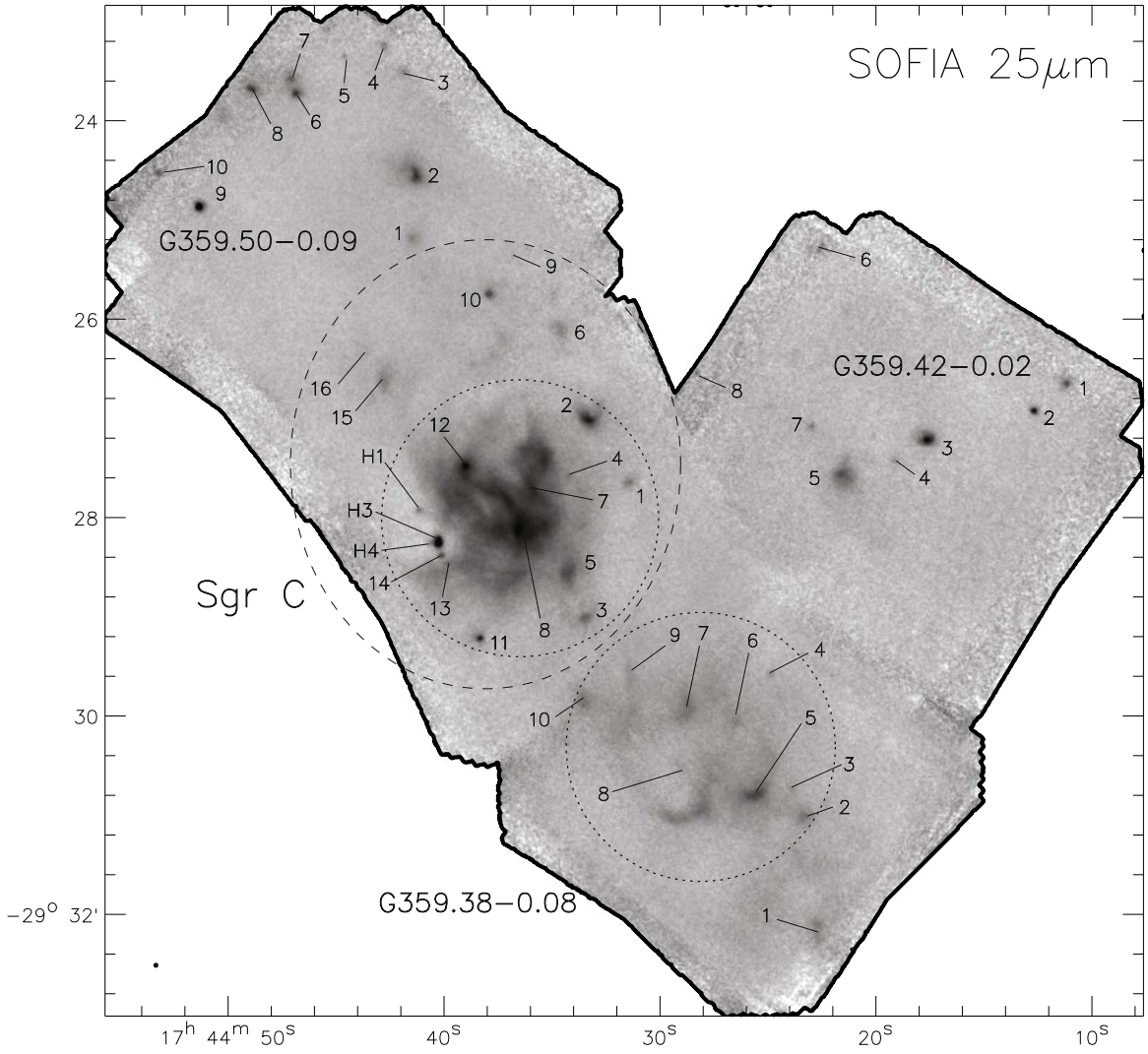

Figure 8. Sgr C image mosaic taken at 25 μm by SOFIA shown in inverse color (i.e., brighter features are darker in color). We break up the region into several subregions: Sgr C (whose bounds are shown by the dashed ellipse), G359.42-0.02 to the west, G359.38-0.08 to the southwest, and G359.50-0.09 to the northeast. The dotted circles denote the apertures used to measure the extended Sgr C H II and G359.38-0.08 H II emission regions. The black dot in the lower left indicates the resolution of the image at this wavelength.

the compact sources (i.e., Tables 1–3). We will discuss this lack of correspondence between the hot and ionized component versus the cold and molecular component in these Galactic center GH II regions and the ramifications in Sections 4.2.1 and 4.2.2.

4.1. Physical Properties of Compact Sources: SED Model Fitting and Determining MYSO Candidates

We define a compact source as one that exhibits a distinct peak which remains consistent in location across different wavelengths and is detected at multiple wavelengths. Therefore, compact source candidates are first identified as resolved sources or peaks in the SOFIA data, and then cross-referenced with Spitzer-IRAC, Herschel-PACS, and cm radio data to check for spatial coincidences. We define compact sources as having physical sizes less than ∼0.4 pc, consistent with the typical size of molecular cores, around 0.1 pc (e.g., H. Zinnecker & H. W. Yorke 2007). We identified 53 compact infrared sources in the SOFIA-mapped area containing Sgr B, 18 of which are associated with the Sgr B1 GH II region and 24 with Sgr B2. In the data covering the areas in and around Sgr C, we find 47 compact infrared sources, with 19 being associated directly with the Sgr C GH II region. Tables 1–3, for Sgr B1, Sgr B2, and Sgr C, respectively, provide details on the compact source positions, radii used for aperture photometry, and the background-subtracted flux densities measured at both SOFIA wavelengths (similar information is provided for all other compact sources on the SOFIA fields in Appendix C). We used the same optimal extraction technique as used in our previous studies (see Paper I), to determine the best aperture for photometry, and similarly performed background subtraction using background statistics from an annulus outside the optimal extraction radius having the least environmental contamination.

We conducted additional aperture photometry for all compact sources using archival Spitzer-IRAC data at 3.6, 4.5, 5.8, and 8.0 μm, as well as Herschel-PACS data at 70 and 160 μm. We applied the same optimal extraction technique to these data as we did to the SOFIA data to obtain the four near-infrared and two far-infrared photometry values. The measured Spitzer and Herschel photometry data for Sgr B1, Sgr B2, and Sgr C are given in the tables in Appendix C.

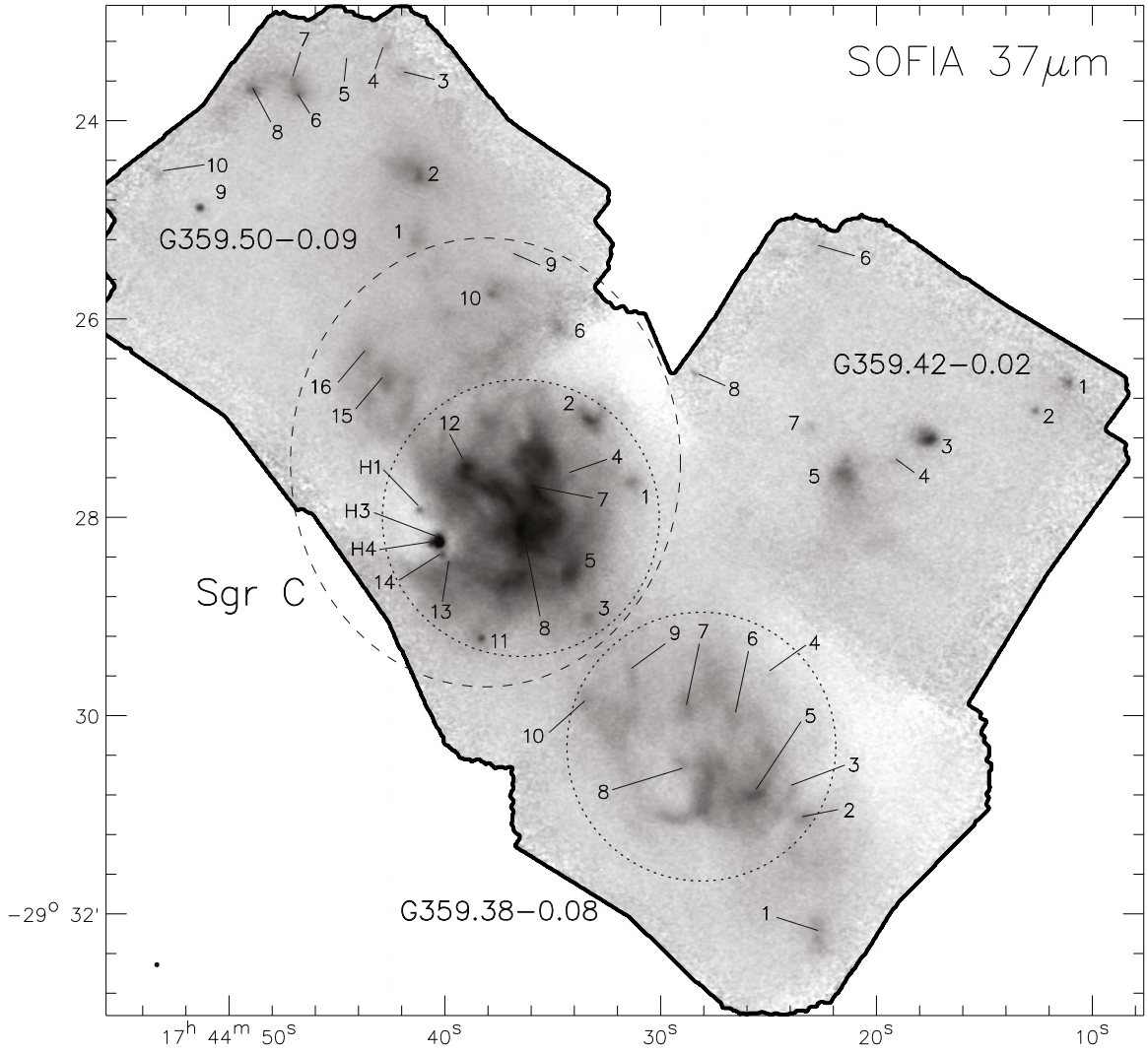

Figure 9. Sgr C image mosaic taken at 37 μm by SOFIA. See caption of Figure 8 for explanation of symbols and figure annotation.

To determine how to handle the Spitzer-IRAC photometry data in the construction of our SEDs, we first assessed the potential for flux contamination in the 3.6, 5.8, and 8.0 μm bands from polycyclic aromatic hydrocarbons (PAHs) emission and in the 4.5 μm band from shock-excited molecular hydrogen emission. As discussed in Paper I, a color–color diagram using Spitzer-IRAC data (3.6–4.5 μm versus 4.5–5.8 μm) can identify sources with flux densities highly contaminated by shock emission and/or PAH emission.

For the Sgr B region, we see from Figure 12 that none of the compact sources are classified as "shock emission dominated"; however, 21 are "PAH emission dominated" sources. In particular, 11 sources in Sgr B1, 6 in Sgr B2, and 4 in G0.6-0.0 are PAH emission dominated. For the Sgr C region, we deduce from Figure 13 that there are also no shock-excited sources, but there are six PAH emission sources: three in Sgr C, one in G359.38-0.08, and two in G359.50-0.09. For the PAH emission dominated sources, their 3.6, 5.8, and 8.0 μm IRAC fluxes are treated as upper limits in the photometry used for constructing the SEDs. The numbers of compact sources plotted in Figures 12 and 13 are not the same as those reported in Tables 1–3, because there are compact sources for which there are only IRAC 3.6, 4.6, or 5.8 μm upper limits (due to saturation, nondetection, or being unresolved from other nearby sources). Of the three GH II regions in the study, this is especially the case for Sgr C, where more than half of the sources (11 of 19) are missing at least one IRAC photometry value. Consequently, for these compact sources where one or more of the IRAC bands have nondetections or are saturated, the color–color analysis cannot be performed. In these cases, we conservatively assume that the sources are PAH-contaminated (i.e., we only treat the 4.5 μm data point as a nominal value, while the rest of the IRAC data points are upper limits).

When constructing the SEDs for our compact sources, we further consider the Herschel-PACS fluxes as upper limits due to the significant and uncertain contamination from the surrounding extended emission, as well as the blending of sources due to poorer angular resolution, which complicates accurate isolation of the 70 and 160 μm flux densities for the compact sources.

Finally, for a couple of compact sources, the Spitzer or Herschel photometry apertures included saturated pixels. In these cases, we use the saturation limit for a point source as a lower limit in the SED fitting.

As for the errors associated with the photometry data, in keeping with our previous methodology (e.g., Paper I), we set the upper error bars on our photometry values as the subtracted background flux value, since background subtraction can vary

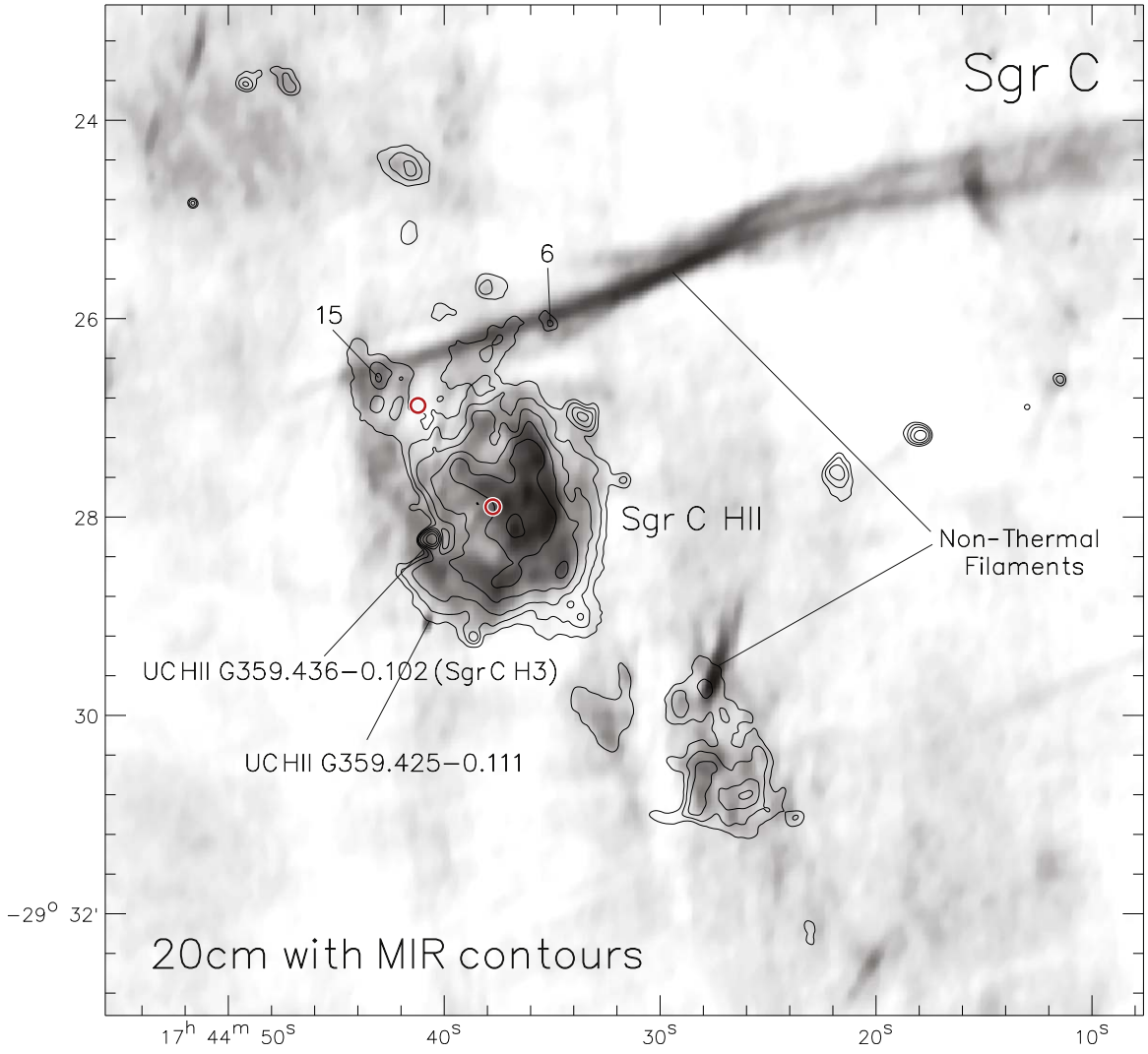

Figure 10. The 20 cm radio continuum image over overlaid with SOFIA 25 μm contours. The two ultracompact H II regions from J. R. Forster & J. L. Caswell (2000) are labeled, as are the locations of some nonthermal filaments. The red circles denote the locations of Wolf–Rayet stars from J. S. Clark et al. (2021).

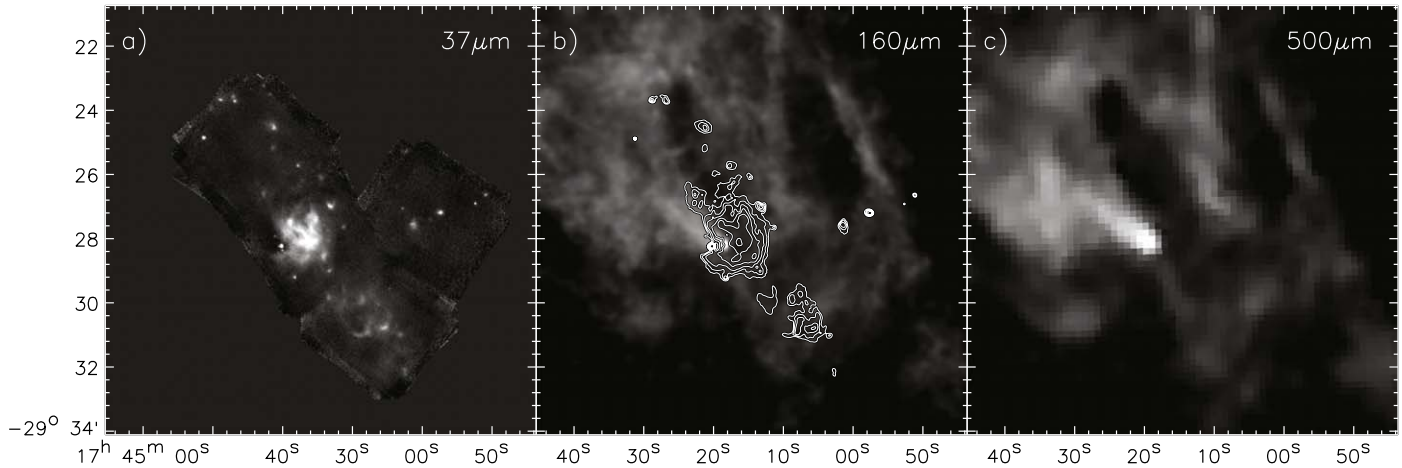

Figure 11. Sgr C region at (a) 37 μm, (b) 160 μm (with 37 μm contours), and (c) 500 μm. The morphology of Sgr C appears very similar to that of the 37 μm image for wavelengths from 8 to 70 μm. The morphology is also very similar from 160 to 500 μm, but very different than the morphology from 8 to 70 μm. Most of the emitting regions seen at 37 μm appear to be devoid of cold dust at 160–500 μm, except for the IRDC finger protruding into the H II region from the east.

significantly but is never larger than the amount subtracted. The lower error bar values for all sources are based on the average total photometric error at each wavelength, set to 20%, 15%, and 10% for the 4.5, 25, and 37 μm bands, respectively. We assume the photometric errors of the Spitzer-IRAC 3.6, 5.8, and 8.0 μm fluxes to be 20% for sources not contaminated by

Table 1
SOFIA Observational Parameters of Sources in Sgr B1

Source	R.A. (J2000)	Decl. (J2000)	25 μm			37 μm			Aliases
			R_{int} (arcsec)	F_{int} (Jy)	$F_{int\text{-}bg}$ (Jy)	R_{int} (arcsec)	F_{int} (Jy)	$F_{int\text{-}bg}$ (Jy)	
Compact Sources									
Sgr B1 A	17 46 53.28	−28 32 00.5	6.1	30.9	25.2	6.1	59.9	46.1	SSTGC726327[a]
Sgr B1 C	17 46 54.36	−28 32 38.8	8.4	26.1	15.3	9.2	46.1	27.1	...
Sgr B1 D	17 46 57.04	−28 33 45.6	10.0	106	87.8	10.7	190	131	...
Sgr B1 1	17 47 01.09	−28 31 15.7	10.0	126	75.9	10.0	236	126	...
Sgr B1 2	17 47 04.56	−28 33 55.3	8.4	13.8	4.77	9.2	40.0	13.6	...
Sgr B1 F	17 47 04.63	−28 29 46.2	6.9	7.22	5.99	9.2	28.8	15.8	...
Sgr B1 G	17 47 06.04	−28 31 04.8	8.4	41.3	18.6	8.4	103	41.3	...
Sgr B1 H	17 47 07.53	−28 28 42.6	9.2	21.3	11.4	10.0	47.2	28.9	SSTGC760679[a]
Sgr B1 3	17 47 08.88	−28 29 55.5	6.1	33.5	28.4	7.7	55.0	41.7	OH 0.548-0.059[b]
Sgr B1 4	17 47 11.65	−28 32 00.6	7.7	25.7	5.87	7.7	62.2	16.8	...
Sgr B1 5	17 47 11.82	−28 31 37.6	6.1	36.9	7.05	6.1	68.0	13.0	...
Sgr B1 6	17 47 12.34	−28 31 42.9	6.1	33.8	17.4	6.1	73.3	34.3	...
Sgr B1 7	17 47 12.81	−28 31 36.0	6.1	47.1	10.2	6.1	75.5	14.6	...
Sgr B1 8	17 47 12.87	−28 32 06.7	7.7	21.6	3.57	7.7	48.2	3.81	SSTGC772981[a]
Sgr B1 9	17 47 14.26	−28 31 10.6	6.1	24.4	4.73	6.9	57.1	12.1	...
Sgr B1 10	17 47 14.65	−28 30 00.7	11.5	42.6	20.7	12.3	84.1	32.5	...
Sgr B1 11	17 47 14.74	−28 32 09.7	10.0	33.6	8.50	10.7	68.3	15.2	...
Sgr B1 12	17 47 17.25	−28 32 21.1	11.5	48.6	33.7	11.5	58.5	48.3	SSTGC782872[a]
Extended Sources									
Ionized Bar	17 46 57.59	−28 31 07.4	143 × 40	801	582	143 × 40	1950	1850	...
Ionized Rim	17 46 59.72	−28 32 27.6	64 × 114	1190	908	64 × 114	3000	2880	...
Sgr B1 Ext1	17 47 01.23	−28 31 14.8	26.0	476	394	26.0	1070	1030	...
Sgr B1 E	17 47 04.28	−28 33 22.9	23.0	435	362	23.0	822	723	...
Sgr B1 I	17 47 12.39	−28 31 22.9	35.0	1100	938	35.0	1920	1780	...
Sgr B1 J	17 47 12.75	−28 30 10.0	28 × 80	283	207	28 × 80	505	410	...

Notes.
[a] From D. An et al. (2011).
[b] Known AGB (OH/IR) star; see S. Shiki et al. (1997).

PAH features. Additionally, as in Paper I, we assume error bars of 40% and 30% for the Herschel 70 and 160 μm data points, respectively.

Using the SOFIA, Spitzer, and Herschel photometry data and their uncertainties, we constructed near- to far-infrared SEDs for all compact sources. These SEDs were then fed into an algorithm developed by Y. Zhang & J. C. Tan (2011), where they were fit with theoretical SED models of MYSOs (referred to as ZT MYSO SED models). Each model fit provides a normalized minimum chi-squared value (the so-called $\chi^2_{\rm nonlimit}$) as an indication of the goodness of fit. As in previous studies, we selected a group of models that show $\chi^2_{\rm nonlimit}$ values similar to the best-fit model and distinguishable from the next group of models showing significantly larger $\chi^2_{\rm nonlimit}$ values. Sometimes, the first or first few best fits have significantly lower $\chi^2_{\rm nonlimit}$ values than those that come after, and in such cases we will include those first fits with the first grouping so that we always have at least five best-fit models.

In Figure 14 for Sgr B1, Figure 15 for Sgr B2, and Figure 16 for Sgr C, the ZT MYSO SED model fits are presented as solid lines (black for the absolute best model fit and gray for the other best-fit models) over the measured photometry points and error bars for each individual source (with SED plots for all sources in G0.6-0.0, G359.38-0.08, G359.42-0.02, and G359.50-0.09 provided in Appendix C). Table 4 for Sgr B1 and Sgr B2 and Table 5 for Sgr C list the physical properties of the MYSO SED model fits. For each source, Column 2 presents the observed bolometric luminosity, $L_{\rm obs}$, of the best model, while column 3 shows the true total bolometric luminosity, $L_{\rm tot}$ (corrected for foreground extinction and outflow viewing angle). The extinction and stellar mass of the best model are listed in columns 4 and 5, respectively. Columns 6 and 7 present the ranges of foreground extinction and stellar masses derived from the models in this group. Column 8 indicates the number of models in the group of best-fit models. The rest of the columns provide information related to whether the sources are likely to be MYSO candidates or not, and they are described further in Section 4.1.3.

4.1.1. Comparisons to S. Crowe et al. (2024) Sgr C SED Modeling Results

Contemporary to the publication of this paper is one by S. Crowe et al. (2024), in which the authors identify three MYSO candidates from a combination of JWST-NIRCam data as well as the same Spitzer, Herschel, and SOFIA data employed in this paper. They label these sources G359.44a, G359.44b, and G359.42a, which are the same as our sources Sgr C H3, Sgr C H4, and Sgr C 11, respectively. Comparing our results to the SED fitting from that work (which also employs the ZT MYSO SED models), we find that we both

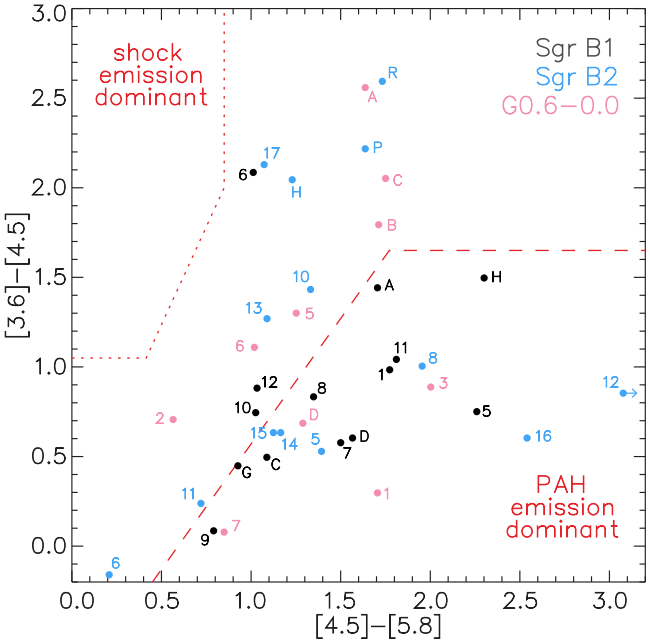

Figure 12. A color–color diagram for compact sources in Sgr B utilizing our background-subtracted Spitzer-IRAC 3.6, 4.5, and 5.8 μm source photometry to distinguish "shocked emission dominant" and "PAH emission dominant" YSO candidates from our list of compact subcomponents. Sources marked by black dots and labels are from within Sgr B1, those marked in blue are from Sgr B2, and those in magenta are from G0.0-0.6. Placement above (upper left) the dotted line indicates the shock-emission-dominant regime. Placement below (bottom right) the dashed line indicates the PAH-dominant regime. We adopt this metric from R. A. Gutermuth et al. (2009). Some sources are not included in this diagram, due to nondetection or saturation in the Spitzer-IRAC bands. The arrow for Sgr B2 12 indicates a high [4.5]–[5.8] value (4.07) that has been cropped off the plot.

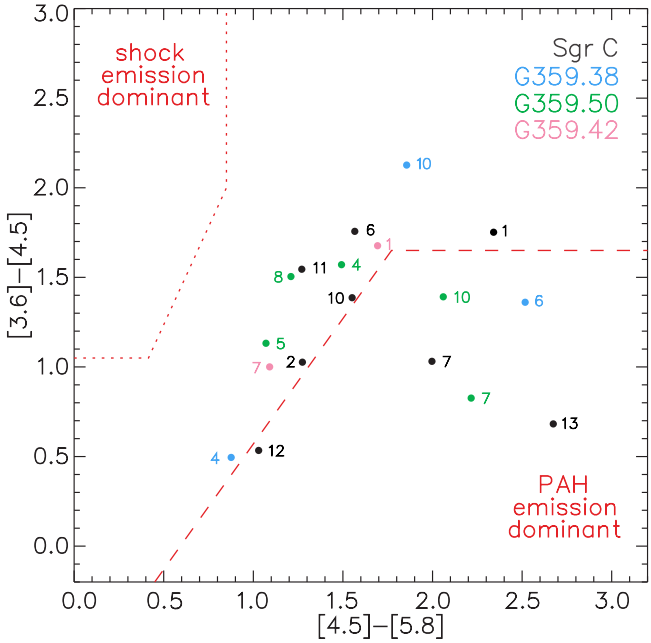

Figure 13. A color–color diagram for compact sources in Sgr C (black), G359.38-0.08 (blue), G359.50-0.09 (green), and G359.42-0.02 (magenta) utilizing our background-subtracted Spitzer-IRAC 3.6, 4.5, and 5.8 μm source photometry. See caption in Figure 12 for more information regarding plot labels.

derive answers consistent with MYSOs for all three sources, but our estimated physical values vary. For one thing, S. Crowe et al. (2024) report estimated values for stellar mass and other parameters by averaging over apparently dozens (perhaps hundreds) of models with a much wider range of goodness of fit, whereas we report the results of the best-fit model (as well as the range of our group of best fits, which all have similar goodness of fit and typically number ∼10 models in total; see Section 4.1.). However, from the figures in S. Crowe et al. (2024), one can see they get best-fit stellar masses of 12, 8, and 96 $M_{\odot}$ for Sgr C H3, Sgr C H4, and Sgr C 11, respectively, which one can compare to the 32, 8, and 24 $M_{\odot}$ that we derive. While the best-fit stellar mass value for Sgr C H4 seems to match in this comparison, the other two sources are quite different (especially Sgr C 11). If we instead compare averaged values, using their model averaging methodology S. Crowe et al. (2024) estimate stellar mass values of $20.7^{+14.1}_{-8.4}$, $20.4^{+24.1}_{-11.0}$, and $8.5^{+11.9}_{-5.0}$ $M_{\odot}$ for Sgr C H3, Sgr C H4, and Sgr C 11, respectively. If we average over our groups of approximately a half-dozen best-fit models for each source, we get mean stellar masses of $30.4^{+1.6}_{-3.5}$, $9.3^{+3.3}_{-1.3}$, and $15.3^{+7.1}_{-6.3}$ $M_{\odot}$ for Sgr C H3, Sgr C H4, and Sgr C 11, respectively. Thus, their averaged model masses are consistent with both our best-fit mass values and our averaged mass values to within their reported errors.

However, the main reason why we do not get exactly the same results using the same data is by and large the product of which data we use as nominal estimates of the source flux densities and which we set as upper limits. In S. Crowe et al. (2024), it is assumed that all flux data at wavelengths <10 μm are upper limits due to the possible presence of PAH contamination. Since these data have the best resolution for resolving sources, we instead choose to test our sources for possible PAH contamination (see Section 4.1) and include the near-infrared data when we can. This helps pin down the SEDs at the shortest wavelengths. For the three sources under discussion here, this methodology led to us being able to use all four Spitzer-IRAC bands in our fit of Sgr C 11 and use the 4.5 μm data as nominal data in the fits for Sgr C H3 (as the 4.5 μm IRAC filter does not encompass any bright PAH features; see W. T. Reach et al. 2006). We determined that we could not accurately isolate the near-infrared flux of source Sgr C H4 because it is too faint and unresolved due to crowding of nearby Sgr C H3 (as well as some extended emission), so we set all IRAC fluxes as upper limits. S. Crowe et al. (2024) measure IRAC fluxes for this source, though the errors are large and nearly the same value as the reported fluxes. Importantly, however, it should be noted that, for all flux densities ⩽37 μm, the reported values from S. Crowe et al. (2024) are very similar to ours, except for the 25 and 37 μm values for Sgr C 11, which are a factor of two lower due to the fact that they employed an aperture approximately half the size of the one we used for this source. This is the result of another difference in methodology, i.e., using resolution-dependent apertures versus fixed apertures for photometry. Since sources can intrinsically have different sizes as a function of wavelength and can be subject to source crowding at certain wavelengths but not others, and because of the large range in data resolutions being used (2″–35″), we chose to find the optimal aperture for each source at each wavelength independently. S. Crowe et al. (2024) used a method where they found the optimal aperture at 37 μm for each source and used that same aperture for all data at wavelengths ⩽37 μm. In the case of Sgr C 11, there is extended and complicated environmental emission around the source at 37 μm that makes the choice of

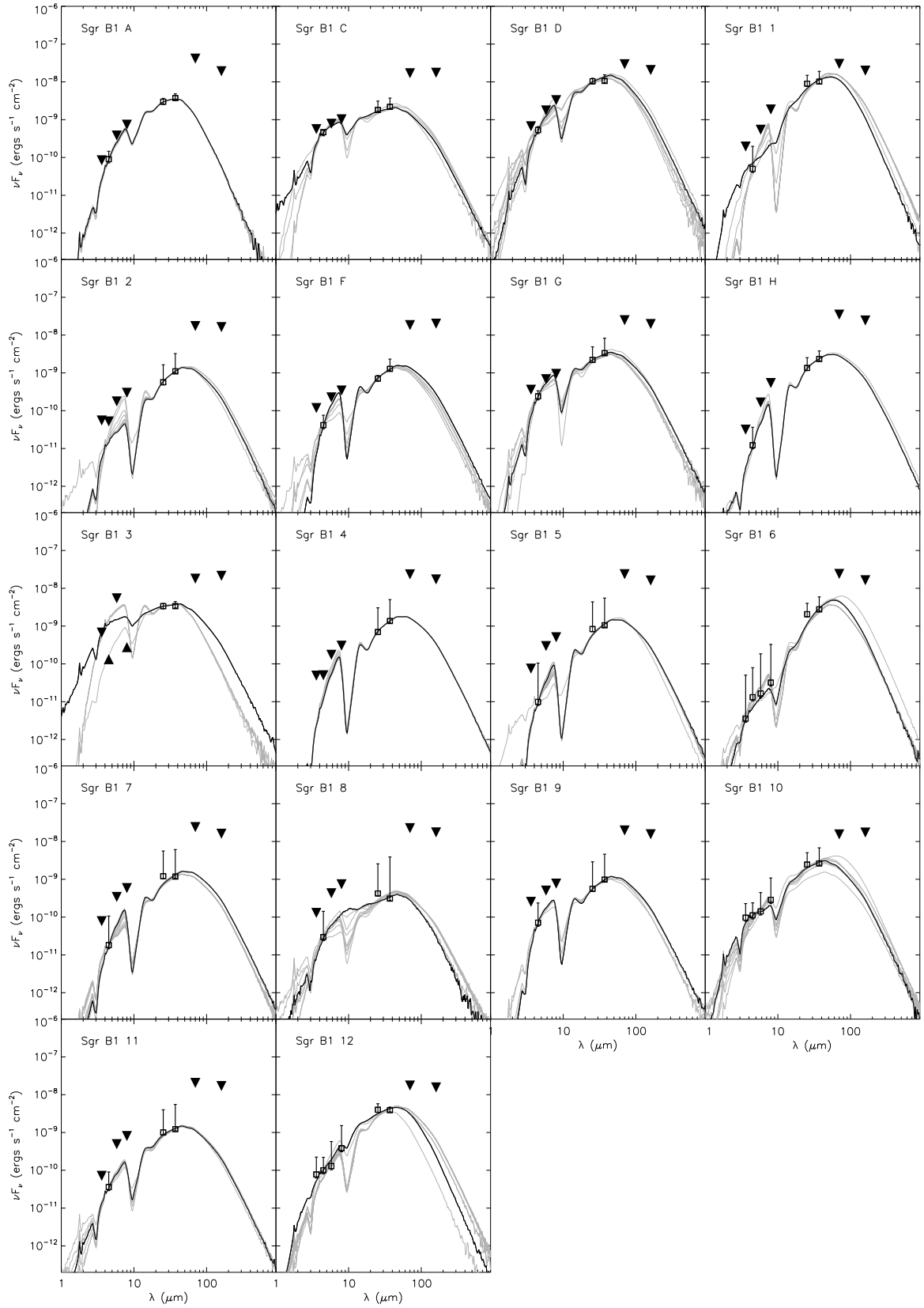

Figure 14. SED fitting with ZT model for compact sources in Sgr B1. Black lines indicate the best-fit model to the SEDs, and the system of gray lines show the remaining fits in the group of best fits (from Table 4). Upside-down triangles are data that are used as upper limits in the SED fits, and upward-pointing triangles are lower limits.

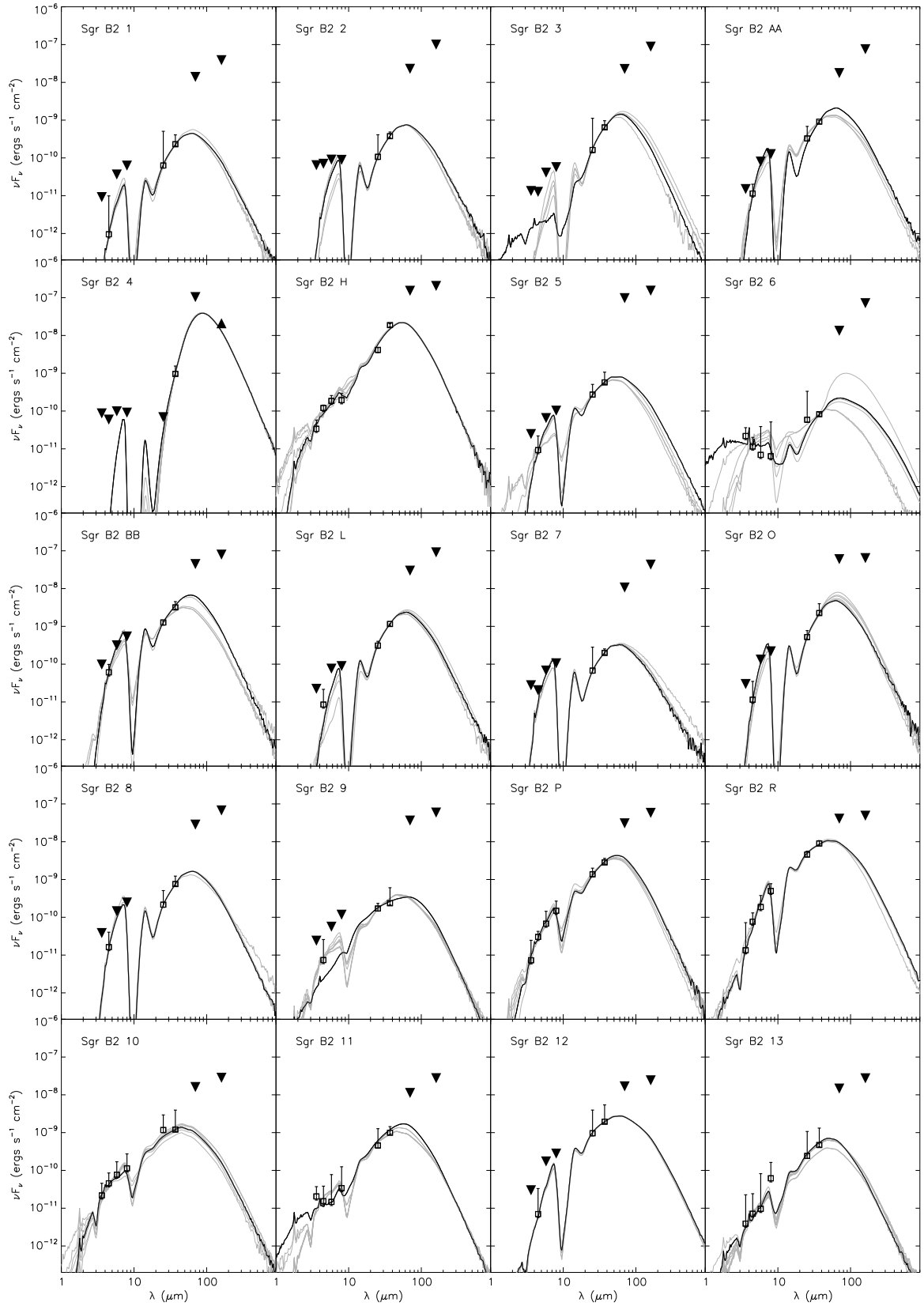

Figure 15. SED fitting with ZT model for compact sources in Sgr B2. Black lines indicate the best-fit model to the SEDs, and the system of gray lines show the remaining fits in the group of best fits (from Table 4). Upside-down triangles are data that are used as upper limits in the SED fits, and upward-pointing triangles are lower limits.

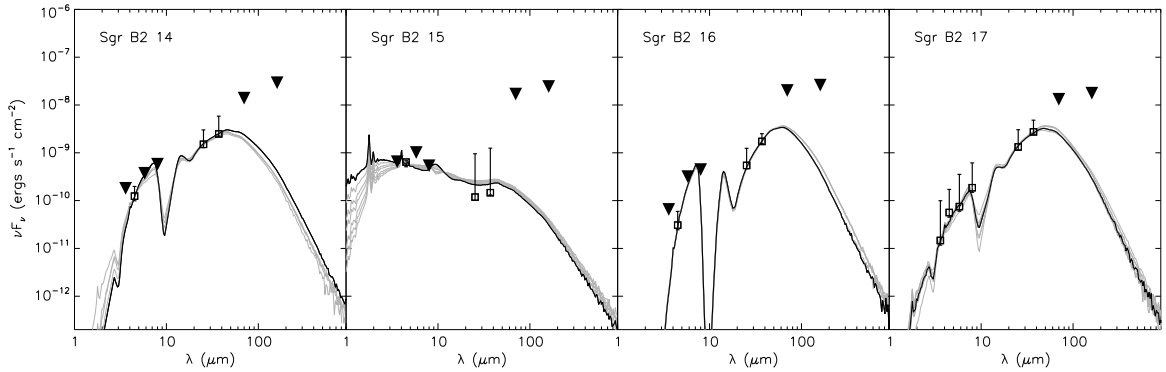

Figure 15. (Continued.)

optimal aperture size more subjective. However, the source is free of extended environmental emission at 25 μm, and a clear background sky level (and hence photometry aperture) can be ascertained. It is therefore evident that source flux is being missed in the smaller aperture of S. Crowe et al. (2024) at both SOFIA wavelengths.

At the longest wavelengths, S. Crowe et al. (2024) use the Herschel photometry as source flux estimates, whereas we choose to use these values as upper limits. While one can more confidently use Herschel photometry data in the case of isolated sources, GH II regions have many MYSOs, often very close to each other, and often embedded within or close to large extended dust substructures. With resolutions of 6, 12, 18, 24, and 35″ at 70, 160, 250, 350, and 500 μm with Herschel (S. Molinari et al. 2016), separate MYSOs and larger-scale structures near each other at shorter wavelengths merge into single sources due to lack of resolution. To address this, the method used by S. Crowe et al. (2024) involved making decisions about how much flux from the unresolved sources at longer wavelengths should be assigned to which sources based upon their ratio of resolved fluxes at a shorter wavelength. In the case of the close-together sources Sgr C H3 and Sgr C H4, they chose to apply the flux ratio between the sources at 37 μm (3:1) to their unresolved fluxes measured at all wavelengths $\geqslant$70 μm. This is likely to be a very rough approximation in general, as such a ratio likely does not hold constant at wavelengths both shorter than and longer than the SED turnover, especially if the real SEDs of the two sources peak at different wavelengths. Furthermore, estimating proper backgrounds at Herschel wavelengths on small scales is also difficult due to large-scale molecular cloud emission, as well as galactic cirrus that can dominate the observed emission, especially at $\lambda \geqslant 250$ μm. Where one should choose to select the background is often not at all obvious, but it has a huge influence on the values reported as a source's background-subtracted flux density (very much akin to the 37 μm photometry issue of Sgr C 11 just mentioned). Given all of these uncertainties, we choose to use the Herschel fluxes as upper limits in our modeling.

It is clear that, because of all of these differences in methodology, our SED fitting results and those of S. Crowe et al. (2024) should not be exactly the same even though the same data and models are being used. While it is encouraging that our results here agree with theirs to within the errors, this is a comparison of only three sources, and in general, such similarities may not always be the case.

4.1.2. Comparisons to A. S. Cotera et al. (2024) Source Catalog

When this paper was in an advanced state, a catalog of point sources derived from the SOFIA-FORCAST data of the Galactic center was published by A. S. Cotera et al. (2024). We cross-referenced the point sources found in that work with our list of sources for Sgr B and Sgr C produced from the same data. All of the sources we identified, except for source Sgr B2 11, are also found in the source list of A. S. Cotera et al. (2024). However, the A. S. Cotera et al. (2024) catalog had far more sources than we found: 127 sources total in Sgr B (compared to our 58) and 84 in Sgr C (compared to our 47). We checked the observational properties of all A. S. Cotera et al. (2024) sources not in common with our lists, and the reasons why they were not included in our list were as follows: (1) the source was not detected at shorter or longer wavelengths than SOFIA (i.e., either in the Spitzer 8 and 5.8 μm images, the Herschel 70 μm images, or the cm radio continuum images); (2) the source was unresolved from another nearby source or from the larger extended emission at multiple wavelengths (in these cases, our photometry generally covered the entire emitting region under the assumption that the source was a single elongated compact source, rather than multiple sources); (3) multiple close-together sources were part of what we considered to be a single extended source (and thus we report it as an extended source in our tables); (4) the source had a very broad peak at multiple wavelengths and was embedded in extended emission (thus making it difficult to determine if it is actually an independent source or simply a slightly more condensed part of a larger diffuse emission region); and (5) the source peak moved around as a function of wavelength (indicating it is not likely to be internally heated). Related to points 2–4 above, the source selection methodology used by A. S. Cotera et al. (2024) is likely to give false positives for elongated and extended sources, as the algorithm tends to try to break these structures up into multiple point sources, which is often unlikely to be correct.

In all cases, if there was a peak detected at 70 μm at the location of a SOFIA source or peak, it is included in our list, as the object of our source selection was not to find all the peaks in the SOFIA data (which was the object of A. S. Cotera et al. 2024), but to find compact sources likely to be internally heated MYSOs. Therefore, we believe that our selection of MYSO candidates in this work is complete to within the detection limits and resolution of the SOFIA data.

Additionally, we randomly selected several of the sources from our lists and spot-checked their photometry with the values reported in A. S. Cotera et al. (2024). In all cases, the

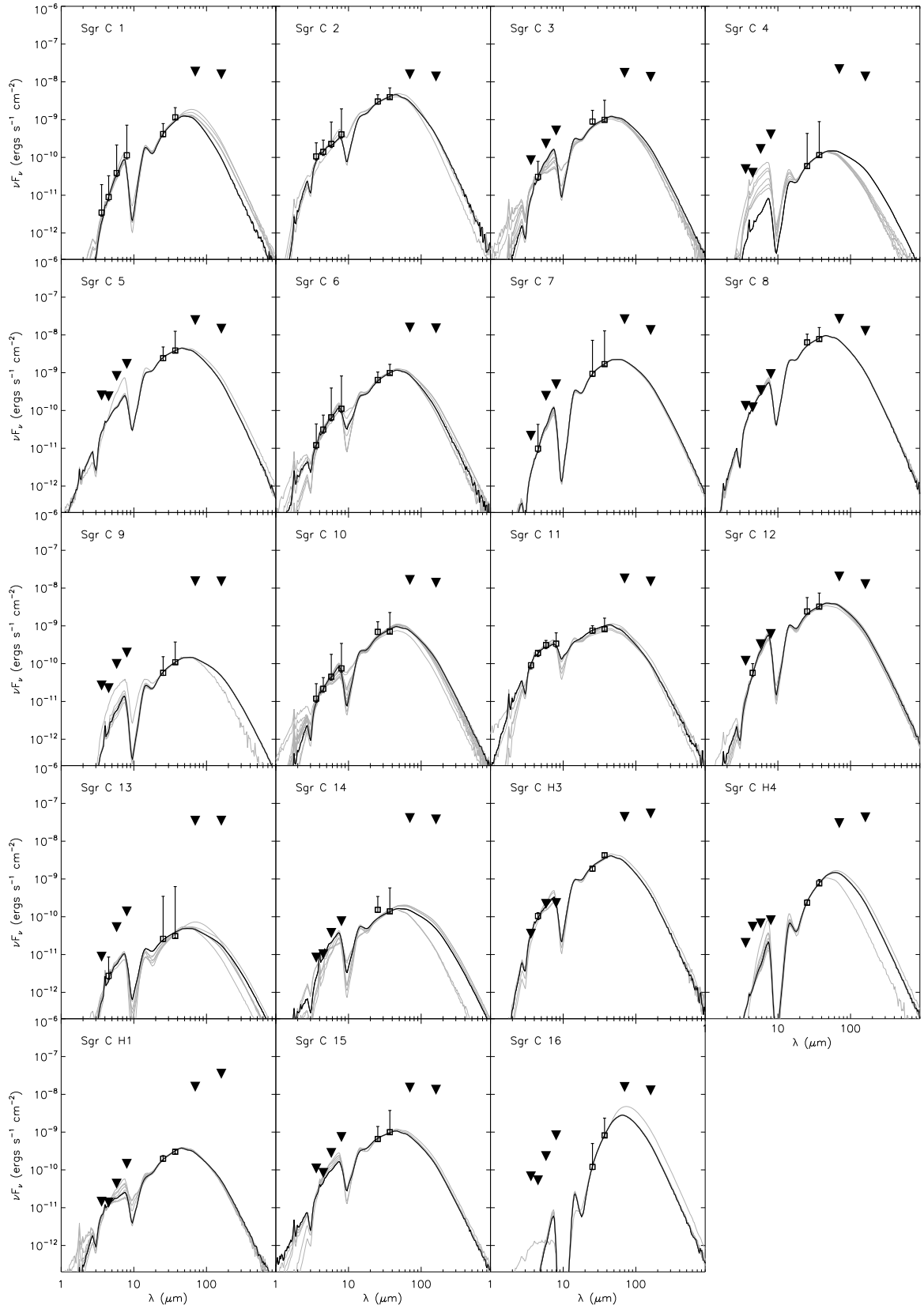

Figure 16. SED fitting with ZT model for compact sources in Sgr C. Black lines indicate the best-fit model to the SEDs, and the system of gray lines show the remaining fits in the group of best fits (from Table 5). Upside-down triangles are data that are used as upper limits in the SED fits, and upward-pointing triangles are lower limits.

Table 2
SOFIA Observational Parameters of Sources in Sgr B2

Source	R.A. (J2000)	Decl. (J2000)	25 μm			37 μm			Aliases
			R_{int} (arcsec)	F_{int} (Jy)	F_{int-bg} (Jy)	R_{int} (arcsec)	F_{int} (Jy)	F_{int-bg} (Jy)	
Compact Sources									
Sgr B2 1	17 47 12.42	−28 24 15.2	6.1	4.28	0.532	6.1	5.06	2.85	SSTGC772151[a]
Sgr B2 2	17 47 17.65	−28 24 01.9	6.9	3.45	0.903	7.7	6.01	4.65	...
Sgr B2 3	17 47 18.53	−28 24 23.4	10.0	9.47	1.37	10.0	12.0	7.94	SSTGC784931[b]
Sgr B2 AA	17 47 19.53	−28 24 39.5	6.9	5.77	2.76	7.7	11.9	11.3	SSTGC787884[b]
Sgr B2 4	17 47 19.72	−28 22 18.2	6.1	<0.58	UD	8.4	19.3	11.9	...
Sgr B2 H	17 47 20.38	−28 23 42.6	8.4	40.3	35.0	9.2	254	232	South, S
Sgr B2 5	17 47 20.62	−28 23 53.3	5.4	4.28	2.30	5.4	13.3	7.10	SSTGC790317[a]
Sgr B2 6	17 47 21.97	−28 24 37.1	6.1	2.81	0.497	6.1	1.14	1.02	SSTGC793536[b]
Sgr B2 BB	17 47 22.17	−28 22 18.9	10.0	11.4	10.7	11.5	56.0	39.3	SSTGC793867[b]
Sgr B2 L	17 47 22.45	−28 21 55.8	7.7	3.40	2.62	7.7	14.4	14.3	...
Sgr B2 7	17 47 22.78	−28 25 37.0	5.4	2.38	0.569	6.1	3.13	2.46	SSTGC795418[b]
Sgr B2 O	17 47 22.93	−28 22 48.0	8.4	6.53	4.40	10.0	49.2	27.8	...
Sgr B2 8	17 47 23.18	−28 23 54.8	6.1	4.29	1.82	8.4	15.2	9.34	SSTGC796410[b]
Sgr B2 9	17 47 23.57	−28 22 33.4	6.9	1.97	1.44	6.1	7.50	2.92	SSTGC797252[b]
Sgr B2 P	17 47 23.70	−28 23 35.6	8.4	16.8	11.6	9.2	44.8	35.1	SSTGC797384[a]
Sgr B2 R	17 47 26.12	−28 22 04.9	11.5	47.3	38.6	12.3	132	111	SSTGC803187[a]
Sgr B2 10	17 47 26.57	−28 24 45.3	10.0	24.8	9.88	11.5	48.8	14.9	SSTGC803471[a]
Sgr B2 11	17 47 27.14	−28 27 27.4	7.7	10.7	3.85	11.5	17.9	12.3	SSTGC805200[b]
Sgr B2 12	17 47 27.58	−28 25 47.5	10.7	33.3	8.13	10.7	67.1	24.1	...
Sgr B2 13	17 47 27.64	−28 26 29.0	6.9	9.01	2.04	7.7	16.3	5.80	SSTGC806191[a,b]
Sgr B2 14	17 47 27.98	−28 22 00.9	10.7	25.4	12.7	12.3	72.3	30.7	...
Sgr B2 15	17 47 28.45	−28 25 56.7	5.4	8.09	1.00	5.4	15.4	1.81	...
Sgr B2 16	17 47 31.08	−28 26 41.9	8.4	10.5	4.59	11.5	31.1	21.4	...
Sgr B2 17	17 47 34.06	−28 27 17.8	10.0	25.7	11.2	11.5	59.6	33.9	...
Extended Sources									
Sgr B2 V	17 47 13.18	−28 24 42.1	27.0	177	118	27.0	390	353	...
Sgr B2 Main	17 47 20.43	−28 23 01.9	27.0	139	95.4	27.0	1330	1200	M
Sgr B2 Ext1	17 47 29.89	−28 26 05.1	28 × 50	112	69.0	28 × 50	269	253	...
Sgr B2 Ext2	17 47 34.52	−28 26 50.9	19.0	124	85.5	19.0	200	160	...

Notes. UD means the source is undetected, and the 5σ upper limit on a detection is given. For this source, the F_{int} value is used as an upper limit in the SED modeling.
[a] From D. An et al. (2011).
[b] From F. Yusef-Zadeh et al. (2009).

values appear to be in agreement to within their combined errors.

4.1.3. Potential Contaminants to the MYSO Candidates

Unlike many of our GH II regions previously studied, this study is not the first mid-infrared survey looking for YSOs in the Galactic center CMZ. Most similar to the work presented here (in terms of spatial resolution and wavelength) is that of F. Yusef-Zadeh et al. (2009), which leverages Spitzer 24 μm data in addition to the four Spitzer-IRAC bands in a search for MYSOs via SED fitting. That work covered not only Sgr B and Sgr C, but the entire CMZ. Though plagued with saturation issues, especially in Sgr B1 and Sgr C, many of the sources identified in that survey are found in ours (see Tables 2 and 3). However, we do identify far more MYSO candidates within the three GH II regions than in that work.

Since the publication of F. Yusef-Zadeh et al. (2009), it has been pointed out by several authors that the shapes of near-to-far-infrared SEDs of MYSOs created via broadband photometry are not unique, and that other objects can have very similar SEDs. These mostly involve far more evolved stellar objects like red giant stars and asymptotic giant branch (AGB) stars, post-AGB stars, including proto-planetary nebulae (proto-PNe), planetary nebulae (PNe), and even heavily extinguished main-sequence stars. In our previous studies of Galactic GH II regions, we ignored the possible contamination of such evolved sources, since they are not commonly found in young massive star formation regions. However, the closeness of Sgr B1, Sgr B2, and Sgr C to the Galactic center means that these regions are subject to rapid dynamical and environmental changes atypical for GH II regions farther out in the Galactic plane. As a consequence, more evolved interlopers are far more common in the CMZ (see Section 4.2.1), and thus possible contamination of these sources in the MYSO counts is possible. We will discuss these potential sources of contamination in our MYSO survey in more detail below.

Main-sequence Stars. It has been argued that main-sequence stars with heavy foreground extinction (C. M. Koepferl et al. 2015) may masquerade as YSOs, with their near-to-mid-infrared SEDs appearing similar to YSO SEDs. In particular, the models assume the main-sequence stars sit in a medium with a typical molecular cloud density range, and we see that (peculiar to these Galactic center GH II regions) most of our

Table 3
SOFIA Observational Parameters of Sources in Sgr C

Source	R.A. (J2000)	Decl. (J2000)	25 μm			37 μm			Aliases
			R_{int} (arcsec)	F_{int} (Jy)	F_{int-bg} (Jy)	R_{int} (arcsec)	F_{int} (Jy)	F_{int-bg} (Jy)	
Compact Sources									
Sgr C 1	17 44 31.39	−29 27 39.1	7.7	6.61	3.50	10.0	25.8	14.2	SSTGC343554[a,b]
Sgr C 2	17 44 33.15	−29 26 59.2	12.3	38.5	25.5	14.6	85.7	49.0	SSTGC348392[a]
Sgr C 3	17 44 33.39	−29 29 00.6	9.2	14.9	7.53	9.2	40.4	12.2	...
Sgr C 4	17 44 34.15	−29 27 36.1	3.8	3.64	0.498	3.8	11.0	1.42	...
Sgr C 5	17 44 34.15	−29 28 32.9	10.7	40.4	20.5	11.5	155	47.7	...
Sgr C 6	17 44 34.56	−29 26 07.8	8.4	8.80	5.44	8.4	20.6	12.2	SSTGC351441[b]
Sgr C 7	17 44 35.86	−29 27 44.5	9.2	60.9	7.94	9.2	159	20.9	SSTGC354683[a]
Sgr C 8	17 44 36.50	−29 28 06.8	9.2	88.7	53.6	9.2	194	96.2	...
Sgr C 9	17 44 36.74	−29 25 22.4	4.6	1.29	0.482	5.4	4.61	1.35	...
Sgr C 10	17 44 37.79	−29 25 44.7	8.4	10.8	5.86	8.4	28.0	8.72	SSTGC360055[a]
Sgr C 11	17 44 38.33	−29 29 12.8	6.1	8.49	6.32	6.1	19.9	10.1	G359.42a
Sgr C 12	17 44 38.97	−29 27 29.9	8.4	47.4	20.3	7.7	91.4	39.9	...
Sgr C 13	17 44 39.74	−29 28 27.5	3.1	2.93	0.220	3.1	7.77	0.380	...
Sgr C 14	17 44 40.03	−29 28 22.9	3.1	2.90	1.29	3.1	7.18	1.72	...
Sgr C H3	17 44 40.21	−29 28 14.5	5.4	18.7	15.8	5.4	62.8	52.4	G359.44a
Sgr C H4	17 44 40.56	−29 28 15.2	3.1	2.38	1.99	3.1	12.0	9.45	G359.44b, C103
Sgr C H1	17 44 41.09	−29 27 56.0	4.6	2.02	1.67	3.8	4.29	3.72	C102
Sgr C 15	17 44 42.73	−29 26 37.7	9.2	11.9	5.55	10.0	46.4	12.3	...
Sgr C 16	17 44 43.62	−29 26 18.5	7.7	4.24	1.01	9.2	29.0	10.1	...
Extended Sources									
Sgr C H II	17 44 36.45	−29 27 59.7	83.6	1630	1440	83.6	4570	4540	...

Notes. Source names and aliases: H names are the compact H II regions found at 1.3 cm from X. Lu et al. (2019b); C names are from *C*-band (6 cm) detections from X. Lu et al. (2019a); and G names are from the shortened Galactic coordinate labels given by S. Crowe et al. (2024).
[a] From D. An et al. (2011).
[b] From F. Yusef-Zadeh et al. (2009).

compact mid-infrared sources do not appear to be within molecular clouds. One advantage our survey has over the F. Yusef-Zadeh et al. (2009) survey is that we additionally have a 37 μm photometry point. The models for non-YSO stars presented by C. M. Koepferl et al. (2015) show flat or decreasing flux from 25 to 37 μm, while our sources have increasing fluxes. Moreover, many of our sources are resolved in the SOFIA data (i.e., $\gtrsim$0.2 pc), indicating a large and extended dust envelope, which is more in line with the sizes of star-forming cores/clumps, and much larger than a main-sequence star would appear. It is this dense envelope that is the origin of the 70 μm flux seen ubiquitously from MYSOs, as predicted by the SED models for early B- and O-type MYSOs. Significant 70 μm flux is not expected for a main-sequence star (especially one not surrounded by a dense dusty medium, which appears to be the general case for the MYSOs in Sgr B and Sgr C). While we use the 70 μm fluxes as an upper limit in our model fitting, all but a very few of our compact SOFIA sources are undetected at this wavelength (see Tables 9, 10, and 11). Additionally, some of our sources also have extended green object (EGO) emission, which is almost exclusively associated with YSOs (C. J. Cyganowski et al. 2008), and others have methanol maser emission or formaldehyde maser emission, both of which are only associated with MYSOs (S. L. Breen et al. 2013; E. D. Araya et al. 2015). Overall, we consider contamination by main-sequence stars in the regions we are studying to be unlikely.

Red Giant and AGB Stars. It has been argued (M. Schultheis et al. 2003) that YSOs can look the same in infrared colors and SEDs as red giant stars and AGB stars if heavily extinguished ($A_V \sim 30$). Additionally, like YSOs, AGB stars can occasionally have OH and water masers (e.g., L. Uscanga et al. 2012), as well as PAH emission (e.g., E. Marini et al. 2023). However, while red giant and AGB stars can take on a wide variety of SED shapes, observationally only a small subset appear to mimic YSOs (e.g., J. A. D. L. Blommaert et al. 2006; M. Busso et al. 2007; M. A. T. Groenewegen 2022), with most having their SEDs turn over at $\lesssim$20 μm (e.g., R. J. Sylvester et al. 1999; K. Volk et al. 2000). Indeed, mid-infrared color–color diagrams using MSX (e.g., M. N. Sevenster 2002) and WISE data (e.g., K.-W. Suh 2024) have been shown to effectively separate YSO populations from proto-PNe, AGB stars, and post-AGB star populations. More specifically, different color criteria are explored by K.-W. Suh (2024, see their Figure 8), where they find that using the longer wavelengths of WISE (i.e., 12 and 22 μm) most clearly separates populations, indicating that the more evolved objects will for the most part appear different in their mid-infrared emission from MYSOs. Additionally, SiO masers are also often found in AGB stars, whereas this species of maser is very rarely seen in YSOs (e.g., S.-H. Cho et al. 2016), and thus if present, these masers would indicate a likely AGB star. However, many of our sources have bright cm radio continuum emission, whereas red giant and AGB stars would not show detectable emission within the sensitivity of our radio data (see,

for instance, G. R. Knapp et al. 1994; L. D. Matthews & M. J. Reid 2007). In fact, the presence of bright cm radio continuum in post-AGB stars is defined as the beginning of the PNe phase (L. Cerrigone et al. 2017; R. A. Cala et al. 2022). We have cross-correlated our sample with as many red giant, AGB star, and SiO maser surveys as we could find, and have discovered that two sources are spectroscopically confirmed red giant stars (G359.42-0.02 2 and G359.0-0.09 8) and that three sources are associated with SiO maser emission (Sgr B1 3, Sgr B2 15, and G359.50-0.09 9) and thus likely to be AGB stars. In fact, Sgr B1 3 is a confirmed AGB star (more specifically an OH/IR star; S. Shiki et al. 1997). As predicted, none of these sources have cm radio continuum emission, and only G359.0-0.09 8 (and maybe Sgr B1 3) has an SED like that of an MYSO. We consider further contamination of our MYSO candidates by red giant and AGB stars to be the largest contaminant, being more likely than main-sequence stars but still minor.

Post-AGB Stars. Post-AGB stars, including proto-PNe and PNe, are perhaps the most difficult to distinguish from MYSOs. The outer dusty layers of gas ejected during the AGB phase will expand during this phase, often achieving sizes greater than our SOFIA resolution (i.e., $\gtrsim$0.2 pc; I. González-Santamaría et al. 2019), and thus PNe could appear either resolved or unresolved in their infrared emission with SOFIA at the CMZ distance. The PNe nucleus is hot enough to heat and ionize the material from these circumstellar ejecta, so they can be readily seen in cm radio continuum emission (L. Cerrigone et al. 2017), with about 50% of PNe having detectable cm radio continuum (I. S. Bojičić et al. 2011). Additionally, post-AGB stars and PNe can display water and hydroxyl masers (e.g., M. N. Sevenster 2002; O. Suárez et al. 2009) as well as PAH emission (e.g., S. A. Rinehart et al. 2002), all similar to those of YSOs. However, these similarities to YSOs are not the norm. Most importantly, only 10%–20% of PNe have detectable MIR emission with MSX (M. Cohen & Q. A. Parker 2003), which has a 22 μm detection limit comparable to the sensitivity of our 25 μm SOFIA data. Moreover, only a small subset of all post-AGB stars and PNe that have detectable mid-infrared emission have SEDs like those of MYSOs, as they display great variability in their SEDs as a class (e.g., K. Volk et al. 2002; B. J. Hrivnak 2000), with most SED turning over between 10 and 30 μm (Y. Zhang & S. Kwok 2009), unlike typical MYSOs. Indeed, as mentioned above, mid-infrared color–color diagrams using MSX data are used to separate star-forming clumps from proto-PNe, as well as post-AGB stars. Furthermore, unlike AGB stars, which are plentiful, proto-PNe and PNe are rare, owing to the short lifetimes of these phases, lasting only a few thousand years for the proto-PNe phase, with the entire PNe lifetime being roughly only 20,000 yr (L. Decin et al. 2020). Being in the turbulent CMZ, any PNe there may disperse even quicker, making this phase very short and thus the occurrence of such sources relatively rare. We believe that post-AGB stars, including proto-PNe and PNe, are unlikely to be a significant contaminant of our MYSO survey.

To avoid some of these issues of misidentifying MYSOs, D. An et al. (2011) used Spitzer IRS ($\sim$5–35 μm) spectra to search for signs of the 15.4 μm shoulder on the absorption profile of the CO_2 ice feature due to the mixing of CO_2 ice with methanol ice on grains. This is a signature known only to exist in the spectra of YSOs. However, while sources with this signature are extremely likely to be YSOs, sources without the feature may or may not be YSOs. In addition to variability of chemical abundances and potential environmental effects, MYSOs are known to generate very energetic outflows that clear out the overlying material, and thus at some orientations we would expect to not see such absorption features (i.e., when preferentially looking at pole-on or near-pole-on angles). Furthermore, such observations are extremely dependent upon proper background subtraction, which could erase such spectral signals in legitimate MYSOs. That being said, we believe that the majority of sources without this spectral feature are likely to not be MYSOs.

In light of all of this, we have defined our sources differently in this paper compared to our previous papers. We have tabulated in Tables 4 and 5 (as well as Table 15) several additional physical properties of our sources taken from the literature and our data. We indicate if the source is resolved or not in the SOFIA data, and if it is well-fit by the MYSO fitter. We further indicate if the source is detected at cm radio wavelengths and/or 70 μm. We tabulate which sources are known to have methanol, formaldehyde, hydroxyl, water, and/or SiO masers. We further indicate which sources have EGO emission. Additionally, if a source has been observed spectrally with Spitzer-IRS, we indicate if it was found to have a 15.4 μm shoulder or not. We also indicate which sources are known red giant and AGB stars from previous studies. Finally, we searched the GAIA Data Release 3 (DR3) catalog for coincidences (with separations $\lesssim$2″) with measured parallactic distances that might indicate a mid-infrared source is a field star unrelated to the CMZ population.

If a source is well-fit by the MYSO fitter, and it has either methanol masers, formaldehyde masers, or EGO emission, or was found to have a 15.4 μm shoulder in its IRS spectrum, then we definitely mark it as an "MYSO" on Tables 4, 5, and 15. These types of emissions are *only* found associated with YSOs. If it is not well-fit by the MYSO fitter or has model fits with masses $<8\,M_{\odot}$, it is not considered an MYSO (though in the latter case, it may still be a lower-mass YSO). If the source has flat or decreasing flux with wavelength, or was found by GAIA to have a distance indicating it is a field star, it is also not considered to be an MYSO. Additionally, if it has SiO maser emission, it is concluded to be an AGB star and not an MYSO. Of the remaining sources, all are either resolved at SOFIA wavelengths, have cm radio continuum, 70 μm, or EGO emission, or have masers, which means none are extinguished main-sequence stars. If the source is well-fit by the SED fitter and has cm radio continuum emission, it is likely not an AGB star, though there is still a relatively small chance it is a post-AGB star or PNe. We will identify such sources as "Likely MYSOs." All other sources will be considered "Possible MYSOs," as they, at a minimum, still are well-fit by the SED fitter.

What is the likelihood of these "Likely" (or "Possible") MYSO candidates being actual MYSOs? Unfortunately, there are no comprehensive direct measurements of the stellar density of AGB stars in the CMZ to understand better our most likely contaminant. According to D. An et al. (2011), they find that about half of the previously identified YSO candidates that they observed do not display the 15.4 μm shoulder, and thus are contaminants to the MYSO population. However, many of the claims for these YSOs were based upon less data than we present here, or come from surveys that covered fields throughout the CMZ and not just in the suspected star

Table 4
SED Fitting Parameters of Selected Compact Infrared Sources in Sgr B1 and Sgr B2

Source	L_{obs} ($\times 10^3 L_\odot$)	L_{tot} ($\times 10^3 L_\odot$)	A_v (mag)	M_{star} ($M_\odot$)	A_v Range (mag)	M_{star} Range ($M_\odot$)	Best Models	Well Fit?	Reso-lved?	Features	MYSO?
Sgr B1											
Sgr B1 A	9.36	102	27	16	27–27	16–16	5	Y	Y	ice,cm,70	Yes
Sgr B1 C	7.93	16.1	1.7	12	1.7–55	8–48	5	Y	Y	cm,70	Likely
Sgr B1 D	42.9	153	12	32	3.4–27	24–48	10	Y	Y	cm,70	Likely
Sgr B1 1	35.6	113	27	16	27–80	16–24	11	Y	Y	cm,70	Likely
Sgr B1 2	3.64	16.1	39	12	2.6–67	8–16	11	Y[a]	Y	cm,70	Likely
Sgr B1 F	4.62	9.67	51	8	7.9–51	8–24	6	Y	Y	cm,70,W,H	Likely
Sgr B1 G	10.8	31.5	22	16	12–81	12–48	7	Y	Y	cm,70	Likely
Sgr B1 H	8.65	10.5	0.8	8	0.8–6.7	8–8	5	Y	Y	ice,cm,70	Yes
Sgr B1 3	15.2	74.7	2.5	24	2.5–80	16–24	5	Y[a]	Y	S,70	No
Sgr B1 4	4.96	9.95	42	8	40–50	8–8	5	Y[a]	Y	cm,70	Likely
Sgr B1 5	4.02	9.67	45	8	17–53	8–8	13	Y	Y	cm,70	Likely
Sgr B1 6	10.8	49.1	53	12	19–67	8–16	9	Y	Y	cm,70	Likely
Sgr B1 7	4.52	9.67	31	8	14–37	8–8	13	Y	Y	cm,70?	Likely
Sgr B1 8	1.34	158	8.4	32	2.6–34	12–32	9	Y	Y	ice	Yes
Sgr B1 9	3.39	28.8	63	16	32–63	8–24	5	Y	Y	70	Possible
Sgr B1 10	8.57	74.7	9.2	24	3.4–31	8–32	10	Y	Y	cm,70,	Likely
Sgr B1 11	4.23	10.2	8.4	8	1.7–27	8–16	7	Y	Y	cm,70	Likely
Sgr B1 12	13.6	49.4	27	12	5.9–39	12–32	12	Y[b]	Y	no ice,cm,70	No?[g]
Sgr B2											
Sgr B2 1	1.00	19.6	140	12	130–196	8–24	5	Y	Y	ice,70	Yes
Sgr B2 2	1.72	81	204	24	160–243	16–24	6	Y[a]	Y	70	Possible
Sgr B2 3	2.88	11.8	8.4	8	8.4–212	8–48	5	Y[a]	Y	70,M,F,H	Yes
Sgr B2 AA	4.55	88.4	223	24	68–223	8–24	5	Y	Y	cm,70	Likely
Sgr B2 4	67.8	294	556	24	503–556	24–24	15	Y[c]	Y	70,M,F,W,H	Yes
Sgr B2 H	47.6	457	25	48	8.4–36	32–64	8	Y	Y	cm,70,M,F,H	Yes
Sgr B2 5	2.14	9.48	81	8	5.3–81	8–12	6	Y	Y	ice?	Possible
Sgr B2 6	0.67	0.57	3.4	2	3.4–77	2–16	6	Y[d]	N	70	No[e,h]
Sgr B2 BB	15.0	213	168	32	53–180	24–64	5	Y	Y	cm,70	Likely
Sgr B2 L	5.07	88.4	151	24	34–151	8–32	5	Y	Y	cm,70	Likely
Sgr B2 7	0.84	158	235	32	201–236	16–32	6	Y[a]	Y	70	Possible
Sgr B2 O	10.1	617	244	64	185–260	12–64	7	Y	Y	cm,70	Likely
Sgr B2 8	3.70	26.6	231	12	220–262	8–48	5	Y	Y	70	Possible?[h]
Sgr B2 9	1.07	2.59	27	2	19–46	2–16	8	Y	Y	70?	Possible?[e,f]
Sgr B2 P	9.99	196	59	32	29–80	12–32	7	Y	Y	ice,cm,70	Yes
Sgr B2 R	29.9	38.6	4.2	16	0.8–34	16–24	7	Y	Y	ice,cm,70,E	Yes
Sgr B2 10	3.80	28.8	18	16	5.3–29	8–24	9	Y	Y	ice,70	Yes
Sgr B2 11	4.20	11.8	8.4	8	2.6–17	8–16	8	Y	Y	70	Possible
Sgr B2 12	7.71	8.83	7.5	8	5.0–24	8–8	5	Y	Y	70	Possible
Sgr B2 13	1.68	11.2	17	8	8.4–34	8–16	10	Y	Y	ice?,70	Possible
Sgr B2 14	8.72	31.5	48	16	18–50	16–48	5	Y	Y	70?	Possible
Sgr B2 15	4.79	24.7	1.7	16	1.7–14	16–16	7	Y[d]	Y	S	No
Sgr B2 16	7.43	119	243	24	233–252	16–32	5	Y	Y	70	Possible
Sgr B2 17	7.97	158	24	32	19–34	16–32	8	Y	Y	70	Possible

Notes. Abbreviations in the "Features" column are defined as follows: cm = cm radio continuum emission; 70 = 70 μm emission; 70? = 70 μm emission present but unresolved from nearby sources; M = class II methanol maser (H. Nguyen et al. 2022); F = formaldehyde maser (D. M. Mehringer et al. 1994); W = water maser (A. J. Walsh et al. 2014; D. M. Mehringer et al. 1993a); H = hydroxyl maser (J. A. Green et al. 2015; D. M. Mehringer et al. 1993a); S = SiO maser (M. Messineo et al. 2002; S. Shiki et al. 1997); and E=EGO emission (F. Yusef-Zadeh et al. 2009). Abbreviations from D. An et al. (2011): ice = 15.4 μm ice feature; ice? = possible 15.4 μm ice feature; and no ice = no 15.4 μm ice feature.

[a] Only two nominal data points are used in the SED fitting, and thus the results of the modeling are less reliable.

[b] The extended emission from this source lies partially off-field at both 25 and 37 μm, which may affect the accuracy of the resultant parameters from the SED fits.

[c] Only one nominal data point is used in the SED fitting. However, since all resultant fits are poor (they all violate lower limit set at 160 μm), the results from the SED fitting are unreliable.

[d] This source has a flat or decreasing flux with wavelength and is thus likely not an MYSO.

[e] Has SED model fits less than 8 $M_\odot$. If fit well by the SED fitter, it may be a low-to-intermediate-mass YSO.

[f] Most fits imply an MYSO.

[g] Has no 15.4 μm ice feature, but no other indicators point to it not being an MYSO.

[h] Coincident with a GAIA source to within 2″ with a measured parallactic distance placing it in the foreground.

Table 5
SED Fitting Parameters of Selected Compact Infrared Sources in Sgr C

Source	L_{obs} ($\times 10^3 L_\odot$)	L_{tot} ($\times 10^3 L_\odot$)	A_v (mag)	M_{star} ($M_\odot$)	A_v Range (mag)	M_{star} Range ($M_\odot$)	Best Models	Well Fit?	Resolved?	Features	MYSO?
Sgr C											
Sgr C 1	3.29	40.7	84	12	37–84	8–12	7	Y	Y	no ice,cm,70	No?[a]
Sgr C 2	14.2	147	23	32	22–27	12–32	5	Y	Y	no ice	No?[d]
Sgr C 3	3.98	10.2	23	8	2.6–307	8–24	11	Y	Y	70	Possible
Sgr C 4	0.52	0.79	3.4	4	3.4–109	4–8	7	Y[b]	N	...	No[c]
Sgr C 5	14.0	33.1	3.4	16	2.5–5.0	12–16	6	Y	Y	cm,70	Likely
Sgr C 6	3.56	80.5	13	24	7.9–25	8–24	8	Y	Y	70	Possible
Sgr C 7	7.23	9.45	10	8	4.2–14	8–8	8	Y	Y	no ice,cm,70	No?[a]
Sgr C 8	29.1	82.0	16	24	16–22	24–24	7	Y	Y	cm,70	Likely
Sgr C 9	0.51	0.79	17	4	10–64	4–4	5	Y[b]	N	70	No[c]
Sgr C 10	3.05	9.48	17	8	5.3–40	8–24	15	Y	Y	no ice,cm,70?	No?[a]
Sgr C 11	4.02	71.4	6.7	24	0.8–59	8–24	6	Y	Y	70,W	Possible
Sgr C 12	13.3	19.9	15	12	5.9–39	12–16	7	Y	Y	70	Possible
Sgr C 13	0.19	0.24	9.2	2	9.2–134	2–4	7	Y	N	70?	No[c]
Sgr C 14	0.65	0.79	11	4	4.2–27	4–8	7	N[b]	Y	70?	No[c]
Sgr C H3	12.2	147	44	32	41–53	24–32	5	Y	Y	cm,70,M,F,E	Yes
Sgr C H4	3.72	11.7	66	8	56–212	8–16	6	Y[b]	Y	70?,M,F	Yes
Sgr C H1	1.16	13.6	27	12	2.6–34	12–16	8	Y[b]	Y	cm,70,M	Yes
Sgr C 15	3.66	9.48	0.8	8	0.8–42	8–16	6	Y[b]	Y	cm,70	Likely
Sgr C 16	6.15	33.8	186	12	25–193	8–16	7	Y[b]	Y	70	Possible

Notes. Notes are the same as for Table 4. "W" here is the water maser detection from X. Lu et al. (2019b).
[a] Has no 15.4 μm ice feature, but no other indicators point to it not being an MYSO.
[b] Only two nominal data points are used in the SED fitting, and thus the results of the modeling are less reliable.
[c] Has SED model fits less than 8 $M_\odot$. If fit well by the SED fitter, it may be a low-to-intermediate-mass YSO.
[d] Spectroscopically determined to be a K or M red giant by D. Jang et al. (2022).

formation regions, so 50% should be considered an extremely conservative upper limit on contaminants.

4.1.4. Identifying MYSO Candidates among the Compact Infrared Sources

Based upon the information compiled in Tables 4 and 5, we will discuss below the properties of the compact mid-infrared sources contained within the confines of Sgr B1, Sgr B2, and Sgr C individually. In particular, we will identify those sources thought to be MYSO or MYSO candidates and discuss estimates of the present MYSO stellar densities in each GH II region to compare to the values we have previously derived for other Milky Way GH II regions. As mentioned in our previous papers, given the angular resolution limitations of FORCAST ($\sim$3″) and the distance to these GH II regions ($\sim$8.0 kpc), we can only resolve structures as small as $\sim$0.11 pc. Therefore, it is likely that, in many cases, the infrared sources discussed here contain protobinaries or even protoclusters. While the assumption of a single MYSO is reasonable when the core contains a dominant primary MYSO, we cannot be certain that this would be the case in general. However, these CMZ GH II regions are all at a distance similar to the average distance of the regions we have studied so far (6.6 kpc), and thus we are making comparisons using approximately the same level of spatial information. With that caveat in mind, as we have done for our previously studied GH II regions, in this section, we will also discuss the brightest SOFIA source in each region, as our past observations have shown that the sources that are brightest at the wavelengths of our SOFIA data generally trace the most massive stars in the present MYSO population. We will additionally use the results from the SED fitting and give the derived mass estimates of these highest-mass sources in each GH II region. Since the stellar mass distribution function appears to be more or less universal from the more modest to the most massive star-forming clusters (R. E. Pudritz 2002), this would imply that the more massive the highest-mass member, the larger the underlying stellar cluster total mass in general. Therefore, we have previously used the masses of the most massive MYSOs as an additional rough proxy for understanding the relative sizes of the presently forming stellar populations within each GH II region we have studied. However, it is unknown if the stellar mass functions that seem universal in stellar clusters in the Galactic plane should even apply to those in the CMZ, given the unique environment and rapid dynamical evolution. With that caveat, and in keeping with our prior studies, we will report the highest-mass MYSO for each CMZ GH II region as well as their MYSO densities below, and compare and contrast them to our results from other GH II regions.

Sgr B1 Compact Sources. For the compact mid-infrared sources identified by SOFIA within the Sgr B1 GH II region, we conclude from the information compiled in Table 4 that there are 3 MYSOs (17%) and 12 Likely MYSOs (67%). One source falls into the Possible MYSO category, while two are found not to be MYSOs. This means that 83% of the compact mid-infrared sources in Sgr B1 are MYSOs or Likely MYSOs. The results in Table 4 show that the absolute best model fits for all the mid-infrared detected YSO candidates in all of Sgr B1 yield protostellar masses in the range $m_* = 8$–$32\,M_\odot$, which is approximately equivalent to a range of ZAMS spectral type B1–O7 stars (R. D. Blum et al. 2000).

Two sources, Sgr B1 D and Sgr B1 8, are tied for the highest best-fit mass of 32 $M_\odot$. To determine which one is most likely

the most massive, we calculated a nonweighted average mass from the group of best fits for each source, and find Sgr B1 D has by far the highest of all sources at 36.8 $M_{\odot}$ (Sgr B1 8 was 19.5 $M_{\odot}$). Though Sgr B1 D is categorized as a Likely MYSO, the values for its best-fit luminosity and average luminosity from all fits (1.5×10^5 and 2.5×10^5 $L_{\odot}$, respectively) are very large. These values are close to (or over, in the case of the average luminosity) the largest theoretical limit for AGB luminosity of $\sim 1.5 \times 10^5$ $L_{\odot}$, for the most massive AGB stars (ranging from metal-rich to metal-poor, i.e., $0.001 < Z < 0.04$; see P. Ventura et al. 2014, 2020). If this source is indeed at the distance of the CMZ, it could not be an AGB star, adding further confidence to it being a legitimate MYSO.

For the two sources that are labeled as not being MYSOs, the emission of Sgr B1 3 is coincident with the location of the OH/IR star OH 0.548-0.059 and has SiO masers (S. Shiki et al. 1997) typical of AGB stars. The infrared SED of this source is flat, with saturated fluxes at 4.5 and 8.0 μm, something not expected for MYSOs in highly extinguished environments. The other source, Sgr B1 12 was found to not have a 15.4 μm shoulder on the absorption profile of the CO_2 ice feature, but its infrared SED looks very similar to that of an MYSO.

Based upon the number of MYSOs and Likely MYSOs combined, we calculate an MYSO density of 0.13 MYSOs pc^{-2}. This would mean that Sgr B1 has an MYSO density slightly smaller than but similar to those of both W49A (Paper III) and W51A:G49.4-0.3 (Paper I) of 0.15 MYSOs pc^{-2}, but below the average of all GH II regions we have studied thus far (0.18 MYSOs pc^{-2}). Sgr B1 also has a total MYSO content (15) similar to those of both NGC 3603 (14; Paper IV) and W49A (22), which are the first and second most luminous GH II regions in the Galaxy. If we used our extremely conservative lower limit estimate that half of the unconfirmed MYSOs (i.e., the Likely plus Possible MYSOs) are true MYSO and add that number (6.5) to the three confirmed MYSOs, the MYSO density value for Sgr B1 would drop to 0.08 MYSOs pc^{-2}, which would place it on the lower-end range of GH II stellar densities, but still higher than the least dense Galactic plane GH II region we have studied (i.e., 0.05 MYSOs pc^{-2} in NGC 3603). At the upper limit, if we add in the one Possible MYSO with the confirmed and Likely MYSOs, this value basically stays the same at 0.13 MYSOs pc^{-2}.

While the more extended regions like the Ionized Rim and Sgr B1 E are the sources with the highest integrated intensity at 6 cm, the brightest compact source at 6 cm is Sgr B1 D (120 mJy; D. M. Mehringer et al. 1992), which, as we mentioned above, is the most massive source in the region, and which is also the brightest MIR source at both 25 (88 Jy) and 37 μm (131 Jy).

Besides the lettered sources in Table 4, which were defined via their radio continuum emission at cm wavelengths, there are additionally several of the MIR-defined compact sources (i.e., the numbered sources that do not already have radio labels) in Sgr B1 that are coincident with radio continuum peaks or sources. In total, 9 of the 12 sources identified in the mid-infrared are associated with 6 cm and/or 20 cm radio continuum peaks (see Table 4), with the definite exceptions being Sgr B1 3, Sgr B1 8, and Sgr B1 9. Sgr B1 3, as we have said, is an AGB star, but Sgr B1 8 is a confirmed MYSO. In our previous studies of the MYSO populations of GH II regions, we have cataloged many sources that appear to be MYSOs but do not have radio continuum emission, and we contend that these may be sources that are at a more youthful phase of stellar evolution, prior to the onset of compact H II regions. Sgr B1 8 is likely a similar object. Though we include Sgr B1 2 and Sgr B1 10 in the list of cm continuum emitters, we caution that they both have potential issues. Sgr B1 2 lies close to a brighter radio sources and appears as a tongue of emission extending out from that bright source, so its radio peak is not well-defined. The radio emission for Sgr B1 10 is weak and consistent with high-frequency noise artifacts seen across the radio image; however, we tentatively assert that this emission is real, due to its coincidence in location with the MIR source and the fact that it has a very similar shape and extent.

Sgr B1 E are the sources with the highest integrated intensity at 6 cm; they are not considered compact sources in our study. The brightest compact source at 6 cm is Sgr B1 D (120 mJy; D. M. Mehringer et al. 1992), and this is also the brightest MIR source at both 25 (88 Jy) and 37 μm (131 Jy).

Sgr B2 Compact Sources. For the Sgr B2 GH II region, of the 24 total mid-infrared compact sources found, we conclude (Table 4) that it contains seven MYSOs (29%) and four Likely MYSOs (17%). The larger number of confirmed MYSOs compared to Sgr B1 is a product of the larger number of sources with methanol and formaldehyde masers, as well as EGO-emitting sources. However, there are a large number of Possible MYSOs (10, or 42%) that require further confirming evidence to assess their true nature. The results in Table 4 show that the absolute best model fits for all the mid-infrared detected YSO candidates in all of Sgr B2 yield protostellar masses in the range $m_* = 2$–64 $M_{\odot}$, which is approximately equivalent to a range of ZAMS spectral type A2–O4 stars.

According to the best-fit SED models, the most massive source in Sgr B2 is Sgr B2 O, with a stellar mass of 64 $M_{\odot}$, or the equivalent of a spectral type O4 ZAMS star. However, Sgr B2 O is tied with Sgr B2 H (a.k.a. Sgr B2 South, or S) and Sgr B2 BB for having the highest top mass given by its mass range from the group of best fits at 64 $M_{\odot}$. Though Sgr B2 H has the second-highest best-fit mass in Sgr B2, all eight of the fits from the group of best fits lie within the range of 32–64 $M_{\odot}$. Furthermore, this source has the highest nonweighted average model fit (50.0 $M_{\odot}$) of all compact sources identified, and is thus likely to be the highest-mass source.

Perhaps consistent with this, Sgr B2 H has by far the brightest flux at 37 μm among all compact sources, and is also the brightest peak after Sgr B2 Main at 70 μm in the Herschel data. Indeed, though the peak of Sgr B2 Main is the brightest peak in the mid-infrared at the SOFIA and Herschel wavelengths, this source is extended in our images and is known to be comprised of multiple compact and ultracompact H II regions. Interestingly, the third-brightest peak at 70 μm is radio source Sgr B2 K (a.k.a. Sgr B2 North, or N), which we do not see in the SOFIA data, likely due to extremely high extinction.

For the two Sgr B2 mid-infrared sources that are labeled as not being MYSOs in Table 4, source Sgr B2 15 has an SED that is generally decreasing with wavelength from near- to mid-infrared, atypical of an MYSO. We also found it to be coincident (to within 2″) with SiO maser emission, which means that this source is most likely an AGB star. Similarly, source Sgr B2 6 has a strange but generally flat SED with wavelength, and most of the fits from the SED fitter imply a mass $\lesssim 4$ $M_{\odot}$ assuming a CMZ distance. However, this source is coincident with a GAIA object (Gaia DR3 4057530371326037248, with a separation of 0.″77, or

a single FORCAST pixel) that has a measured parallactic distance of 5078 pc, and thus it is likely a source in the foreground of the CMZ. Similarly, source Sgr B2 8 is also only 1.″72 from a GAIA source (Gaia DR3 4057530405685287424) that has a measured parallactic distance of only 588 pc. However, this source separation is at the limit of our expected astrometric error, and given the high stellar density of field stars toward the Galactic center, it may be a chance alignment with a foreground star, especially given that the SED fitter yielded good results and the SED is typical of an MYSO (as opposed to Sgr B2 6). We therefore label this source as a Possible MYSO, but with a question mark, in Table 4. Finally, like Sgr B2 6, Sgr B2 9 has a best fit of 2 $M_{\odot}$; however, unlike Sgr B2 6, Sgr B2 9 has an SED more typical of YSOs. Also, all fits for Sgr B2 9, except the best-fit SED, are $\gtrsim$12 $M_{\odot}$, implying that it is likely an MYSO, with an average mass from all fits of 12.9 $M_{\odot}$. However, given the higher uncertainty, we also label this source as a Possible MYSO, but with a question mark in Table 4.

Besides the two sources we identify as not being MYSOs (8%) in Sgr B2, there are significantly more Possible MYSOs than we tabulated for Sgr B1 with 11 (46%), mostly due to a higher portion of sources with no detected cm radio continuum emission. As we have stated before, our previous surveys have revealed a great number of MYSOs that are at such a youthful stage that they are being detected in the mid-infrared prior to the onset of their UCH II regions. This might point to Sgr B2 as having a more youthful population of MYSOs than Sgr B1, as further evidenced by the prolific number of observed UCH II regions (R. A. Gaume et al. 1995; F. Meng et al. 2022), masers (D. M. Mehringer & K. M. Menten 1997; E. J. McGrath et al. 2004; J. L. Caswell et al. 2010), and mm cores (A. Ginsburg et al. 2018) in Sgr B2.[9]

On a related note, several of the radio emitting sources in Sgr B2 are seen in the SOFIA data at one or both wavelengths (e.g., Figure 6). Radio sources that we detect clearly in the mid-infrared are AA, BB, H, L, O, P, and R (as well as V, but again, this source may not be related to Sgr B2, given its anomalous velocity). These sources are all well-fit as MYSOs, based on the SED fitting of their infrared emission, with three being confirmed MYSOs via other indicators. The other four of these radio continuum emitters are categorized as Likely MYSOs. Given their proximity to the molecular clump centered on Sgr B2 Main, their likelihood of being true MYSOs is further enhanced. Interestingly, we do not detect mid-infrared emission with SOFIA from radio sources K, Q, W, Y, or Z. Radio sources K, W, Y, and Z all lie north or west of the peak of Sgr B2 Main, which is thought to be the region of highest extinction, hence the reason for their nondetections (but these are all likely to house MYSOs). Source Q is perhaps barely detected at 37 μm at the two-sigma level, but the emission is point-like. Since it is not observed at any shorter wavelengths, we did not try to fit it with our SED models. Radio source K is a diffuse patch of extended radio continuum, and we detect slightly extended mid-infrared emission from Sgr B2 4 on the southwest edge of its emission in the SOFIA data, but only at 37 μm. It is unclear if this is emission leaking out of a less-extinguished part of radio source K, or is in fact a true MYSO (it is not coincident with any compact radio or mm cores, of which there are many in this general area; F. Meng et al. 2022; A. Ginsburg et al. 2018). Under the assumption that Sgr B2 4 is an independent source, it is tenuously found to be an MYSO from the SED fitting because said fits are based upon a single nominal data point at 37 μm (but it has highly constraining upper and lower limits at the other wavelengths). However, the source is coincident to within 2″ with methanol, formaldehyde, water, and hydroxyl masers, so its categorization as such an MYSO seems more certain.

In total, Sgr B2 has 11 sources identified as either MYSOs or Likely MYSO (46%). Based upon this number, we calculate an MYSO density of 0.07 MYSOs pc^{-2}, which is consistent with the value for NGC 3603 of 0.05 MYSOs pc^{-2}, the least mid-infrared MYSO-dense Galactic plane GH II region we have studied. This is also almost half what we calculated for Sgr B1. This total number of confirmed and Likely MYSOs (11) is comparable to the MYSO content of the less prolific GH II regions W51A:G49.4-0.3 (10) and K3-50 (8). However, using our worst-case lower-limit scenario (as we discuss for Sgr B1 above), we derive a slightly higher value of 0.09 MYSOs pc^{-2}, similar to the lower limit we calculated for Sgr B1. For the upper limit, if we include the Possible MYSOs with the confirmed and Likely MYSOs (22 total), the value for Sgr B2 would rise to 0.14 MYSOs pc^{-2}, comparable to the Sgr B1 upper limit and just below the average for Galactic plane GH II regions. Also, at 22 MYSOs, the total number of MYSOs would be the same as one of the most prolific GH II regions we have studied, W49A.

Sgr C Compact Sources. For the Sgr C GH II region we find that, based upon the results reported in Table 5, of the 19 infrared compact sources identified, 3 are confirmed to be MYSOs (16%) and another 3 are Likely MYSOs (16%). All three of the confirmed MYSOs are sources found within the IRDC located here, and all have methanol maser emission (and/or formaldehyde masers and EGO emission), which are tracers of current massive star formation. Sgr C also has five Possible MYSOs (26%). We do caution that one Likely MYSO (Sgr C 15) and one Possible MYSO (Sgr C 16) are well-fit with MYSO SED models, but only two nominal data points were used in the SED fitting, so their confidence is less robust than the others in their categories.

The absolute best model fits for the mid-infrared detected sources in all of the Sgr C GH II region yield protostellar masses in the range $m_{*} = 2$–$32\,M_{\odot}$ (Table 5), which is approximately equivalent to a range of ZAMS spectral type A2–O7 stars. Sgr C H3 and Sgr C 2 are tied for being the highest-mass sources at 32 $M_{\odot}$ for their absolute best-fit mass; however, if we calculate the nonweighted average mass from their groups of best-fit models, Sgr C H3 is clearly more massive (30.4 $M_{\odot}$) than the rest of the sources in the region. Consistent with this, the brightest peak in the mid-infrared is Sgr C H3 (572 mJy pix^{-1} at 25 μm and 1305 mJy pix^{-1} at 37 μm). However, in terms of integrated brightness, Sgr C 8 is the brightest source in the mid-infrared. Sgr C 8 is also the brightest peak at 6 cm, which may not be surprising, as it lies near the center of the extended Sgr C H II region.

If we count just the confirmed and Likely MYSOs (six), we measure an MYSO density of 0.08 MYSOs pc^{-2}, which is comparable to the value for confirmed and Likely MYSOs in Sgr B2. For further comparison, having six confirmed and Likely MYSOs would be comparable to the MYSO content of the less prolific GH II regions M17 (seven) and K3-50 (eight).

[9] Of all the mm cores identified by A. Ginsburg et al. (2018), Sgr B2 2 is the only compact mid-infrared-identified source coincident with a small cluster of these cores. Unresolved and extended mid-infrared emission is also present in and around the cluster of cores in Sgr B2 Main.

Deriving our worst-case lower-limit MYSOs scenario (as we discuss for Sgr B1 above), we derive a value of 0.09 MYSOs pc^{-2}, very similar to the lower limit values we derived for Sgr B2 (0.09 MYSOs pc^{-2}) and Sgr B1 (0.08 MYSOs pc^{-2}), but again, still higher than the value of 0.05 MYSOs pc^{-2} in NGC 3603, which we derived in the least dense Galactic plane GH II region we have studied. In our upper limit case where all Likely and Possible MYSOs (eight) are counted along with the three confirmed MYSOs, we get a value of 0.14 MYSOs pc^{-2}, which again is similar to the upper limit cases for both Sgr B2 (0.14 MYSOs pc^{-2}) and Sgr B1 (0.13 MYSOs pc^{-2}) and a little below the average of all GH II regions we have studied thus far (0.18 MYSOs pc^{-2}).

Despite these similarities, Sgr C is different than Sgr B1 and Sgr B2 in that it has a high incidence of mid-infrared sources that are suspected to not be MYSOs (eight, compared to two each for Sgr B1 and Sgr B2). The two reasons for this are that half of these sources (Sgr C 1, Sgr C 2, Sgr C 7, and Sgr C 10) have been observed spectroscopically by D. An et al. (2011) and shown not to have the 15 μm ice shoulder indicative of an MYSO, and the remaining four sources (Sgr C 4, Sgr C 9, Sgr C 13, and Sgr C 14) not only have SED fits less than 8 $M_\odot$ but they all have an average mass from all fits of less than 8 $M_\odot$ (with Sgr C 9 and Sgr C 13 both having maximum masses of only 4 $M_\odot$ in their range of best fits). These four sources with lower-mass fits are all well-fit by the YSO fitting algorithm, and thus may be legitimate low-mass YSOs. However, this higher incidence of mid-infrared sources not being MYSOs may mean Sgr C has an intrinsically different stellar population than Sgr B1 and Sgr B2, with potentially more interlopers and/or low-mass YSOs present.

Of the 11 MYSO candidates (i.e., confirmed, Likely, and Possible combined) in Sgr C, five (45%) are associated with obvious 6 cm and/or 20 cm continuum peaks: Sgr C 5, Sgr C 8, Sgr C H3, Sgr C H1, and Sgr C 15 (Table 5). This again provides confirming evidence of the MYSO nature of these sources. However, Sgr C 1, Sgr C 7, and Sgr C 10 also have cm radio continuum but do not have detected 15 μm ice shoulders indicative of YSOs (D. An et al. 2011). Again, there are likely occasional exceptions to the rule, and a small subset of legitimate YSOs may lack this spectral ice feature, but it is unlikely that this is the case for all three sources. It would also be surprising if all sources were (proto)PNe, given their rarity. Therefore, these sources would be interesting to follow up in order to determine their true nature.

There are only a few radio-defined sources in Sgr C (see Figure 10), the main Sgr C H II region, and the UCH II regions G359.436-0.102 (our source Sgr C H3) and G359.425-0.111 (J. R. Forster & J. L. Caswell 2000). Of these, the G359.425-0.111 UCH II region is the only source without a detected mid-infrared component in the SOFIA data. Sgr C 6 is interesting in that there is no radio continuum emission detected at its mid-infrared peak; however, this source lies near (at least in projection) the nonthermal radio filament, and there appears to be a ring of radio continuum emission around the source at both 6 and 20 cm (Figure 10). However, Sgr C 15 is also coincident with the nonthermal filament and has peaks at both 6 and 20 cm, but the third mid-infrared source in/near the nonthermal filament is Sgr C 16, which has no obvious radio emission.

When this manuscript was in an advanced state, a study by S. Crowe et al. (2024) that was based upon SED modeling using a combination of these SOFIA-FORCAST data and JWST-NIRCam data, claimed that Sgr C H3 (their G359.44a), Sgr C H4 (their G359.44b), and Sgr C 11 (their G359.42a) are MYSOs. In the work presented here, the first two are confirmed MYSOs, and the third is considered a Possible MYSO.

4.2. Physical Properties of Extended Subregions: Evolutionary Analysis and Status

In our previous studies, we used the radio continuum maps to help us determine the locations of the different extended subregions that make up the larger GH II region. These subregions were believed to be the star-forming molecular clumps within the larger molecular cloud hosting the GH II because they had similar morphologies not only in their mid-infrared emission but in their CO emission (e.g., ^{13}CO $J = 1$–0) and cold dust (far-infrared continuum) emission as well. The CO and mid- to far-infrared data allowed us to derive kinematic and evolutionary information for each subregion. The relative ages of these regions were then used to infer something about the origin of the GH II region and/or how it has evolved to its present appearance.

However, we see that the radio continuum regions within Sgr B1, Sgr B2, and Sgr C have little to no correspondence to the clumps and structures seen in CO emission data, nor in the far-infrared/submm continuum. In particular, we find that there is no CO or far-infrared emission corresponding directly with any large radio structure in the GH II regions of Sgr B1 or Sgr C. Sgr C does have CO and far-infrared emission corresponding to the IRDC, but this structure itself has no radio continuum emission, and more importantly, no mid-infrared emission for us to perform our normal analyses.

We identified two molecular clumps in Sgr B2, Sgr B2 Main and Sgr B2 V, suitable for an evolutionary analysis similar to that applied to our GH II regions. Notably, Sgr B2 V is likely unassociated with Sgr B2 (Section 3.1.2), leaving Sgr B2 Main as the sole clump for analysis. Our methodology involved deriving clump masses through pixel-by-pixel graybody fits to Herschel data and calculating bolometric luminosities with two-temperature fits across various bands. Background fluxes were adjusted per resolution and environmental emission, with virial properties calculated from ^{13}CO(1-0) data (T. Oka et al. 1998). For further details of the methodologies, refer to previous papers (e.g., Paper I).

Sgr B2 Main has an unusually low virial parameter ($\alpha_{\rm vir} \approx 0.23$), suggesting it may be among the youngest molecular clumps in our sample of all GH II regions. It also has extreme extinction and a high mass surface density of approximately 3.5 g cm^{-2}, which aligns with its early evolutionary state near an IRDC. Notably, this mass surface density corresponds to an approximate extinction of ~787 mag in A_V (adopting 1 g cm^{-2} = A_V/224.8 mag; J. Kainulainen & J. C. Tan 2013; W. Lim et al. 2016). This extinction value aligns well with the high extinction ($A_V > 500$ mag) derived for a nearby point source Sgr B2 4 from YSO fitting results (see Table 4). However, Sgr B2 Main's high L / M value (≈580) contrasts with other low-$\alpha_{\rm vir}$ clumps, such as G49.5-0.4 b of W51A (where $\alpha_{\rm vir} \approx 0.18$ and $L/M \approx 26$), and is likely due to contamination from photodissociation regions (PDRs). The bright mid-infrared and 20 cm emissions in Sgr B2 Main support this interpretation, as PDR influence can artificially raise near- and mid-infrared fluxes, increasing the bolometric luminosity—a trend also noted in our previous GH II studies (e.g., Paper II).

The evolutionary histories of Sgr B and Sgr C are much harder to understand from the present observations than our previous studies of GH II regions far from the Galactic center and in the spiral arms of the Galactic disk. This is because, for regions farther out in the Galactic plane, young stars do not stray from their birthplaces within the host giant molecular cloud. However for Sgr B and Sgr C, which are only 100 and 90 pc, respectively, from the Galactic center (Paper IV), this does not seem to be the case. It only takes ∼5 Myr for an object at the locations of Sgr B and Sgr C to rotate around the Galactic center, assuming both regions have a circular velocity of ∼110 km s^{-1} (M. C. Sormani et al. 2022), which is fraction of a stellar lifetime. At these Galactic center distances, stars will stray much quicker from their birthplaces; even bound star clusters could dissolve in ∼30 Myr (S. F. Portegies Zwart et al. 2001). Furthermore, the turbulent crossing time of typical molecular clouds in the CMZ is ∼0.3 Myr (J. Kauffmann et al. 2017), and therefore the feedback from star formation will change them over timescales longer than this (X. Lu et al. 2019b). This indicates that, although many of the MYSOs we are detecting are likely young and may still be in a phase before the onset of radio continuum emission—making them too youthful to have strayed far from their birthplaces—their natal environments may have already undergone significant changes. This could potentially be one reason behind the lack of correlation of molecular material and the mid-infrared and radio continuum.

4.2.1. The Nature of the Ionized Emission in Sgr B1, Sgr B2, and Sgr C

In our previous studies, the GH II regions were ionized and heated primarily by revealed or nascent massive stars that were born in situ within the molecular clouds hosting the GH II regions. However, it appears that in Sgr B there are several ionizing Wolf–Rayet (WR) and O supergiant stars that are sufficiently evolved that they have lived long enough to have at least encircled the Galactic center once. Likewise, J. S. Clark et al. (2021) find that Sgr C contains two highly ionizing WR stars.

In just Sgr B1, J. C. Mauerhan et al. (2010) and J. S. Clark et al. (2021) find a total of three WR and one O supergiant star, which are visible as point sources in the IRAC data. One is situated in the center of the shell of Source I, and the other is situated west of the Ionized Rim (Figure 4). Given their locations on the sky, it may be that these two evolved but powerful objects are ionizing Source I and the Ionized Rim. J. P. Simpson et al. (2021) state that the four evolved stars in Sgr B1 account for a combined Lyman continuum photon rate of 1.4×10^{50} s^{-1}. They state that this is half the amount needed to power the entire Sgr B1 GH II region, which they claim has a total of 3×10^{50} s^{-1}. However, we calculate, based on radio continuum observations, an observed Lyman continuum photon rate for Sgr B1 of $N'_{LyC} = 2.0 \times 10^{50}$ s^{-1} in Paper IV, meaning the WR stars would account for almost three quarters of the total ionizing photons in the Sgr B1 GH II region. Though observations by F. Nogueras-Lara et al. (2022) suggest that Sgr B1 may have an excess of stars <60 Myr old, J. P. Simpson et al. (2018) speculate that Sgr B1 is not ionized by a central cluster, and they instead claim that these interlopers are now presently ionizing the molecular material and may be triggering present star formation. It is likely that these more evolved stars were formed in a different cluster elsewhere in the CMZ, already orbited the GC, and are now recent interlopers to the Sgr B1 region.

In Sgr C, one of the two WR stars (2MASS J17443734-2927557) is fairly centrally located within the main Sgr C H II region and visible in the Spitzer IRAC images (Figure 10). This star is believed to be a WC8-9 star, and these stars typically have luminosities of 2.5–4.0 $\times$ 10^5 $L_\odot$, which alone is similar to the luminosity of the entire Sgr C H II region ($L_{\rm H\,II} = 4 \times 10^5\,L_\odot$; H. S. Liszt & R. W. Spiker 1995). The second WR star is similarly thought to be a WC8-9 star, and it lies 75″ northeast of the center of the Sgr C H II region (i.e., just outside its ∼70″ radio continuum radius). Though F. Nogueras-Lara (2024) find the Sgr C region has a significant population of young stars around 20 Myr old, like Sgr B1, Sgr C may not be predominantly ionized by a stellar cluster, but rather the two evolved stars alone could be responsible for the vast majority of the ionization within the Sgr C GH II region. Given that the WC stars discussed have ages of about 3–8 Myr (G. Meynet 1995), these two stars, as is the case for Sgr B1, likely did not form in situ to the clumps they are now ionizing. The relationship between the tip finger-shaped IRDC and the H II region is not well understood, but it may be that the WC interloper is externally heating and ionizing this IRDC finger, creating the H II region we see, and perhaps even triggering the star formation in the IRDC.

As we have just suggested for Sgr C, there is also some speculation (J. C. Mauerhan et al. 2010; J. S. Clark et al. 2021) that perhaps these interloper stars in Sgr B1 have triggered the collapse of that region's clouds and clumps on their journeys through the Sgr B1 region. Though all of Sgr B1 and the ionized regions of Sgr C appear to lack dense molecular material and cold dust, they may have had widespread but diffuse materials that were held apart by high turbulence, which were then triggered to collapse by these passing interloper stars. Additionally, these interlopers are massive enough to ionize these regions as they move through them, and as we mentioned, this may be causing much of the more widespread radio continuum emission we see.

The situation is different for Sgr B2. There is one evolved O supergiant star located almost equidistant between Sgr B2 7, Sgr B2 10, and Sgr B2 12 (Figure 6). However, this star is located ∼2.′5 southeast of Sgr B2 Main and is coincident with an extended infrared emission region but no substantial radio continuum emission. It therefore likely contributes little to the radio-defined Lyman continuum photon rate of Sgr B2, which is dominated by the contributions from the many compact H II regions. An additional WR star is also found in G0.6-0.0.

Finally, though GH II regions are dominated by thermal emission, there is increasing evidence that the integrated radio flux of H II regions in general may have a substantial nonthermal component (e.g., G. Garay et al. 1996; A. Mücke et al. 2002). Cosmic-ray ionization is potentially one of the leading sources of nonthermal emission (M. Padovani et al. 2019), and it may be particularly enhanced in CMZ H II regions (F. Meng et al. 2019; J. Bally et al. 2024). Indeed, the CMZ on large scales has been measured to have typically 2 orders of magnitude higher cosmic-ray ionization rates than in the solar Galactic environment (J. D. Henshaw et al. 2023). However, this cosmic-ray flux becomes too attenuated when penetrating the embedded star-forming environments of molecular clouds, and instead it is believed that relativistically accelerated electrons within H II region shocks may be a dominant source

of locally generated nonthermal emission (M. Padovani et al. 2019). Since the strength of this nonthermal emission is dependent upon magnetic field strength, it has been conjectured that the generally stronger magnetic fields of the CMZ (~1 mG versus 1−100 μG in the solar neighborhood; J. D. Henshaw et al. 2023) may lead to an enhanced nonthermal component in CMZ GH II regions (J. Bally et al. 2024). Evidence supporting this idea comes from F. Meng et al. (2019), who measured a 60% nonthermal component to the radio flux of Sgr B2 DS, as well as J. Bally et al. (2024), who find that the Sgr C GH II region seems to be riddled with small-scale (subparsec) nonthermal filaments. Therefore, in addition to the ionizing emission contributed by evolved interloper stars, another difference in the total measured ionized flux in CMZ GH II regions versus Galactic plane GH II regions is the potentially much larger level of nonthermal emission that comes from cosmic rays accelerated locally.

4.2.2. Are Sgr B1, Sgr B2, and Sgr C Bona Fide GH II Regions?

The most basic definition of a GH II region is a source that exceeds a Lyman continuum photon rate of $N_{LyC} = 10^{50}$ photons s^{-1}. However, the naive assumption is that, when a region has this Lyman continuum photon flux, it is due to the presence of a cluster of massive ionizing stars either recently formed from or presently forming within a host giant molecular cloud. Thus, the moniker "GH II regions" is generally taken to be synonymous with young H II regions hosting the most powerful sites of massive star formation in a galaxy (e.g., L. F. Smith et al. 1978; P. S. Conti & P. A. Crowther 2004).

With their lack of molecular material and scarcity of cold dust, both Sgr B1 and Sgr C are peculiar compared to GH II regions that are located in the Galaxy's spiral arms. As we have mentioned, for all seven GH II regions in our prior studies, emission from the material of the host giant molecular cloud (as traced by Herschel 160, 250, 350, and 500 μm dust emission as well as emission lines of molecular species) was intermingled with the radio continuum and/or mid-infrared continuum emission, and for all GH II regions even had very similar morphology. A lack of molecular gas and cold dust is usually associated with older and evolved massive star clusters. Indeed, P. S. Conti & P. A. Crowther (2004) rejected some bright radio sources from their final GH II census due to them being much older regions that lacked molecular gas (i.e., Westerlund 1). Given their high levels of present star formation and the rapidity with which these CMZ regions evolve, it would be hard to classify Sgr B1 and Sgr C as old GH II regions. Therefore, one could make an argument that these sources may represent a new class of GH II region. Conversely, however, if we combine the lack of cold dust/molecular material with the fact that the origin of the high Lyman continuum photon rate for both of these regions is due to evolved interloper stars, Sgr B1 and Sgr C do not fit the classical picture of GH II regions, nor our previous observations of GH II regions. Therefore, even though Sgr B1 and Sgr C contain MYSOs at stellar densities similar to those of previously studied GH II regions, based upon these other nonconformant properties, one could reasonably argue that Sgr B1 and Sgr C are not legitimate GH II regions.

Sgr B2, on the other hand, which was not in our prior GH II region census, is rich in molecular material and surrounded by cold dust, and it is presently undergoing very rigorous massive star formation. However, though it is extremely bright in its radio continuum emission and has a very high Lyman continuum photon rate ($\log(N_{LyC}) = 51.04$ s^{-1}), it appears to have relatively little mid-infrared emission. This could be due to the fact that there is an extremely high level of local and Galactic extinction toward this region, or because it is a very youthful starburst region in the process of generating its first-generation massive star cluster out of an infrared dark cloud (or a combination of both). In any case, this lack of bright near-to-mid-infrared emission was the original reason for it being excluded from our GH II source list. Given all of the observable characteristics of Sgr B2 other than its overall level of mid-infrared emission (i.e., very high N_{LyC}; typical MYSO stellar density; coincidence of mid-infrared, far-infrared, cm radio continuum, and molecular material), it certainly seems to better fit the classical definition of a GH II region than Sgr B1 or Sgr C. Or perhaps, given the fact that there is so little extended radio continuum emission, and given its apparent extreme youth, one might instead consider Sgr B2 to be a proto-GH II region.

Since massive star-forming regions are typically quite bright in the mid-infrared, one may assume that identifying GH II regions based in part on their 12–100 μm fluxes, as was done by P. S. Conti & P. A. Crowther (2004), would seem reasonable. However, Sgr B1, Sgr B2, and Sgr C show the limitations of using this method when trying to determine whether a source fits this classical idea of a GH II region. These idiosyncrasies of Sgr B1, Sgr B2, and Sgr C compared to our previously studied GH II regions may be simply be due in large part to the bizarre environment of the Galactic central region. However, it may also be reasonable to conclude that any surveys searching for GH II regions (either within our Galaxy or in external galaxies) should cross-correlate the radio continuum data with molecular (e.g., CO) and/or cold dust (e.g., Herschel 250 μm) maps, which appear to be better indicators of host giant molecular clouds (and thus, ongoing massive star-forming regions) than the mid-infrared.

5. Summary

In this, our seventh paper from our mid-infrared imaging survey of Milky Way GH II regions, we used SOFIA-FORCAST 25 and 37 μm images with $\lesssim$3″ spatial resolution that covered the entire mid-infrared and radio continuum emitting areas of three GH II regions in the Milky Way's CMZ: Sgr B1, Sgr B2, and Sgr C. We compared these SOFIA-FORCAST images with previous multiwavelength observations from various ground- and space-based telescopes in order to discern the morphological and physical properties of these regions. Our previous studies of have shown that, at our SOFIA wavelengths, the majority of the compact mid-infrared sources we find are harboring massive young stars that are presently in the act of forming. However, the closeness of these particular GH II regions to the Galactic center means that these regions are subject to rapid dynamical and environmental changes atypical for GH II regions farther out in the Galactic plane. The practical upshot of this is that Sgr B and Sgr C may contain a much higher incidence of evolved interloper stars masquerading (in terms of their near-to-far-infrared SEDs) as MYSOs. We argue that, while the uncertainty of any particular source as an MYSO candidate in the Galactic center GH II regions is higher (in the absence of evidence beyond merely having an MYSO-like SED), overall we still expect the majority of our sources to indeed be MYSOs, and indeed, we have evidence for several sources indicating that they are in fact MYSOs.

Additionally, we compared the more global properties of these three CMZ GH II regions to the GH II regions we previously studied farther out in the Galactic plane. In many ways, the CMZ GH II regions are similar to those in the Galactic plane; however, Sgr B1 and Sgr C are fundamentally different in several respects. Below, we describe these results in more detail and itemize the other major takeaways from this study.

1) In the whole of Sgr B, which includes both Sgr B1 and Sgr B2 GH II regions, as well as their nearby surrounding areas, a total of 53 compact mid-infrared sources are found, of which 11 are considered to be confirmed MYSOs via SED fitting of their infrared photometry and the presence of definitive MYSO tracers, such as methanol masers. We categorize a further 20 sources as Likely MYSOs based upon SED fitting of their infrared photometry and the presence of cm continuum radio emission, with an additional 17 categorized as Possible MYSOs based solely upon SED fitting alone. In the whole of Sgr C, which includes the Sgr C GH II region and its nearby surroundings covered by the SOFIA data, a total of 47 compact mid-infrared sources are found, of which only 4 are considered to be confirmed MYSOs, with 7 categorized as Likely MYSOs, and 18 Possible MYSOs. In total, within all of the fields covered in our SOFIA-FORCAST data, we have identified 77 CMZ MYSO candidates.

2) Within the confines of just the Sgr B1 GH II region, we find 18 compact mid-infrared sources, of which we believe 16 (89%) to be either MYSOs (3) or MYSO candidates (12 Likely MYSOs and 1 Possible MYSO). Source Sgr B1 D has the highest mass at $32\,M_{\odot}$, as derived from the best-fit MYSO model, and the highest average mass ($37\,M_{\odot}$) among the group of best-fit models. It is also the brightest compact source at cm radio continuum wavelengths, as well as the brightest source at 25 and 37 μm. The extended radio continuum emission comprising the GH II region and the extended mid-infrared continuum emission as seen by SOFIA are fairly well-matched across all of Sgr B1.

3) Within the confines of just the Sgr B2 GH II region, we find 24 compact mid-infrared sources, of which we believe 16 (92%) to be either MYSOs (7) or MYSO candidates (4 Likely MYSOs and 11 Possible MYSO). Sgr B2 H (a.k.a. Sgr B2 South) has highest average mass ($50\,M_{\odot}$) among the group of best-fit models, and it is believed to be the most massive mid-infrared source in Sgr B2. Consistent with this claim, Sgr B2 H is the brightest peak at 37 μm as well as 70 μm (after Sgr B2 Main, which is not considered a compact source). Extinction appears to be extremely high to the west of Sgr B2 Main, as we do not see any mid-infrared emission from prominent radio continuum sources K, Q, W, Y, and Z, even at 37 μm. Furthermore, we have many more Possible MYSOs in Sgr B2 (46%) than in Sgr B1 (6%), mostly due to a higher proportion of compact mid-infrared sources with no detected cm radio continuum emission. This may mean that Sgr B2 has a larger percentage of MYSOs at a more youthful stage prior to the onset of a ultracompact H II region than Sgr B1, which is perhaps in keeping with the idea that Sgr B2 is a more youthful star-forming environment overall.

4) Within the confines of just the Sgr C GH II region, we find 19 compact mid-infrared sources, of which we believe 11 (58%) to be either MYSOs (3) or MYSO candidates (3 Likely MYSOs and 5 Possible MYSO). Sources Sgr C 2 and Sgr C H3 (a.k.a. G359.44a) are tied with the highest mass at $32\,M_{\odot}$ (as derived from the best-fit MYSO model). Sgr C H3, however, has the highest average mass fit ($30\,M_{\odot}$) and also has the highest peak brightness in the SOFIA data at 25 and 37 μm. Sgr C differs from Sgr B1 and Sgr B2 in having a much lower percentage of combined MYSO and MYSO candidates as well as a much higher percentage of mid-infrared sources that are confirmed as not being MYSOs (46%, compared to 11% for Sgr B1 and 8% for Sgr B2). Half (4) of the non-MYSO sources lack the 15.4 μm spectral ice feature indicative of an MYSO, and the other half (4) have SED fits that indicate they are low-mass YSOs (or perhaps red giant or AGB interlopers/foreground objects). Furthermore, the only mid-infrared sources confirmed to be MYSOs are all located within the tip of the IRDC present here.

5) Despite several distinct differences between the three regions, they all have very similar lower and upper limits for their MYSO stellar density estimates. Our worst-case scenario estimates yield MYSO stellar density values of 0.08, 0.09, and 0.09 MYSOs pc^{-2} for Sgr B1, Sgr B2, and Sgr C, respectively. Our most optimistic upper limit estimates are 0.13, 0.14, and 0.14 MYSOs pc^{-2}. Both limits are in the range (0.05–0.29 MYSOs pc^{-2}) of the GH II regions we have studied previously, but both are both also less than the average (0.18 MYSOs pc^{-2}). This result is consistent with the perception that CMZ star-forming regions do not appear to be as prolific as one might expect, but they are indeed presently producing MYSOs at a rate consistent with GH II regions farther out in the Galactic plane, albeit at a rate below the average. Additionally, the fact that MYSO stellar density values are comparable across all three CMZ GH II regions is perhaps surprising, given that Sgr B2 is thought to be a much more prolific star formation environment than the others, and the differences in extinction between the regions are surely a factor.

6) The MYSO with the highest best-fit mass of $64\,M_{\odot}$ for Sgr B2 is consistent with several of the other GH II regions we have studied farther out in the Galactic plane. In particular, W51A:G49.4-0.3, M17, and NGC 3603 all top out with MYSOs having $64\,M_{\odot}$ for their best-fit masses. However, the most massive MYSOs found in both Sgr B1 and Sgr C are only $32\,M_{\odot}$, which would place them at the bottom of the rankings —above only DR 7, whose status as a GH II region is questionable. Since the most massive member of a cluster informs us as to the likely underlying cluster mass function, this is another indication that the present star formation in Sgr B1 and Sgr C may be less prolific than Sgr B2. It may also indicate that, while the CMZ GH II regions appear similar in many ways to Galactic GH II regions, it may be more difficult to form the highest-mass O stars here.

7) For all of our previously studied GH II regions, their morphologies were similar in hot and cold dust emission (as traced by the SOFIA-FORCAST and Herschel-PACS/SPIRE data) and in their ionized gas emission (traced by cm radio continuum), as well as in their molecular gas emission (in maps like ^{13}CO $J = 1$–0). However, in Sgr B1 and Sgr C, as well as (but to a lesser degree) Sgr B2, we have good morphological correspondence between cm radio continuum emission and 25–70 μm emission, but sources and features seen at these these wavelengths do not display any emission from cold dust ($\gtrsim$160 μm) or molecular material. Sgr B2 and Sgr C do have molecular gas and cold dust reservoirs (in the form of IRDCs) for continued star formation, but Sgr B1 does not.

8) Sgr B1 contains three Wolf–Rayet and one evolved O supergiant, and Sgr C contains two Wolf–Rayet stars. In both Sgr B1 and Sgr C, it appears that the dominant contribution to the overall Lyman continuum photon rate to the GH II regions is by the ionization provided by these evolved interloper stars that were very likely not even formed from the same material as the presently forming stars in each region. It could be that the Sgr B1 GH II region and most of the Sgr C GH II region were interspersed by diffuse material held apart by high turbulence and were triggered to collapse into the present mid-infrared structures and MYSOs by the passing of these interloper stars. This could account for the lack of dense molecular material and cold dust directly associated with these features and MYSOs. Additionally, these interlopers are ionizing their immediate surroundings as they move through these regions, and they may be causing much of the more widespread radio continuum emission we see there.

9) For the Sgr B1 and Sgr C GH II regions, given the anticorrelation between the location of the overwhelming majority of their hot dust/ionized emission and the location of cold dust/molecular material, these two sources may represent a new category of GH II region. Further evidence of their nonconforming character comes from the fact that they are most likely predominantly ionized by stars not of their own making. Both characteristics may be in large part due to the fact that everything is moving swiftly around the Galactic center at the small Galactic radii of the Sgr B1 and Sgr C orbits, as well as the generally highly turbulent environment of the CMZ. On the other hand, since the naive assumption is that GH II regions are the result of clusters of massive stars forming from, and still residing within, their natal giant molecular clouds, one could argue that, instead of being a new category of GH II region, Sgr B1 and Sgr C are not legitimate GH II regions at all.

Acknowledgments

We would like to thank the anonymous referee for valuable input that helped improve the quality of the manuscript. This research is based on archival data from the NASA/DLR Stratospheric Observatory for Infrared Astronomy (SOFIA). SOFIA was jointly operated by the Universities Space Research Association, Inc. (USRA), under a contract with NASA, and the Deutsches SOFIA Institut (DSI), under a contract from DLR to the University of Stuttgart. This work is also based in part on archival data obtained with the Spitzer Space Telescope, which was operated by the Jet Propulsion Laboratory, California Institute of Technology under a contract with NASA. This work is also based in part on archival data obtained with Herschel, an European Space Agency (ESA) space observatory with science instruments provided by European-led Principal Investigator consortia and with important participation from NASA. This research has made use of Aladin Sky Atlas, CDS, Strasbourg Astronomical Observatory, France.

The lead author wishes to acknowledge NASA funding via an ADAP Award (80NSSC24K0640), which made this work possible.

W.L. is supported by Caltech/IPAC under contract No. 80GSFC21R0032 with the National Aeronautics and Space Administration.

Facilities: SOFIA, Spitzer, Herschel.

Software: sofia_redux (M. Clarke & R. Vander Vliet 2023).

Appendix A
Data Release

The FITS images used in this study are publicly available in the Dataverse (W. Lim 2019). This repository includes the versions of the SOFIA-FORCAST 25 and 37 μm final image mosaics (of both Sgr B and Sgr C and their exposure maps) that were used in our analyses presented here. The data for Sgr B were cropped from the larger Galactic center mosaic of M. J. Hankins et al. (2020) with additional background correction (see Section 2). However, the Sgr C mosaics were created specifically for this study, and they cover a larger area around Sgr C than was covered in the M. J. Hankins et al. (2020) mosaic.

Appendix B
Additional Photometry of Sources in Sgr B1, Sgr B2, and Sgr C

As stated in Section 4.1, in addition to the fluxes derived from the SOFIA-FORCAST data, we derived additional aperture photometry values for all compact sources using archival Spitzer-IRAC data at 3.6, 4.5, 5.8, and 8.0 μm, as well as Herschel-PACS data at 70 and 160 μm. Like the FORCAST data, we applied the same optimal extraction technique to the Spitzer data. However, performing the optimal extraction technique on the Herschel-PACS data failed for all sources, due to contamination from extended emission from other nearby sources and/or bright environmental emission. For the contaminated compact sources in the Herschel-PACS data, we used an aperture that best fit the largest size of the source at any wavelength to derive flux estimates within the aperture, but we did not derive background-subtracted photometry values.

Tables 6, 7, and 8 list the photometry values we derived from the Spitzer-IRAC data for all sources within Sgr B1, Sgr B2, and Sgr C, respectively. Tables 9, 10, and 11 give the photometry values from the Herschel-PACS data for all sources within Sgr B1, Sgr B2, and Sgr C, respectively.

Table 6
Spitzer-IRAC Observational Parameters of Sources in Sgr B1

Source	3.6 μm			4.5 μm			5.8 μm			8.0 μm		
	R_{int} (arcsec)	F_{int} (mJy)	F_{int-bg} (mJy)	R_{int} (arcsec)	F_{int} (mJy)	F_{int-bg} (mJy)	R_{int} (arcsec)	F_{int} (mJy)	F_{int-bg} (mJy)	R_{int} (arcsec)	F_{int} (mJy)	F_{int-bg} (mJy)
Compact Sources												
Sgr B1 A	4.8	101	51.0	6.0	218	135	6.0	736	412	6.0	1960	1270
Sgr B1 C	6.0	676	603	6.0	780	704	6.0	1510	1230	7.2	2730	1860
Sgr B1 D	8.4	803	626	8.4	989	800	9.6	3400	2160	9.6	8760	5740
Sgr B1 1	8.4	234	42.3	8.4	296	75.3	8.4	1050	247	8.4	4970	1190
Sgr B1 2	4.8	<65.5	UR	4.8	<77.5	UR	4.8	340	90.6	4.8	793	190
Sgr B1 F	4.8	<141	UR	4.8	114	62.3	4.8	435	206	4.8	912	405
Sgr B1 G	7.2	431	322	7.2	507	361	8.4	1320	542	8.4	2520	798
Sgr B1 H	4.8	37.9	6.63	4.8	54.6	18.4	6.0	319	98.0	8.4	1440	466
Sgr B1 3	6.0	808	746	sat	sat	sat	7.2	10500	9920	sat	sat	sat
Sgr B1 4	4.8	58.7	UD	4.8	<75.4	UD	4.8	336	44.9	4.8	808	20.0
Sgr B1 5	6.0	89.9	10.1	6.0	157	14.8	6.0	572	75.9	6.0	1350	277
Sgr B1 6	4.8	60.5	4.28	4.8	119	19.7	4.8	356	32.0	4.8	875	85.5
Sgr B1 7	4.8	93.4	21.9	4.8	159	27.3	6.0	659	69.3	6.0	1560	241
Sgr B1 8	7.2	155	28.6	7.2	213	44.6	7.2	827	98.7	7.2	1970	229
Sgr B1 9	7.2	304	130	7.2	354	107	7.2	970	141	7.2	2050	244
Sgr B1 10	7.2	273	116	7.2	357	167	7.2	862	274	9.6	2890	768
Sgr B1 11	4.8	85.6	29.0	4.8	135	54.4	7.2	948	184	7.2	2150	441
Sgr B1 12	8.4	268	93.3	8.4	330	151	8.4	1120	250	10.8	4060	1030
Extended Sources												
Ionized Bar	143 × 40	<8.15	UD	143 × 40	<8.01	con	143 × 40	<24.2	con	143 × 40	51000	41200
Ionized Rim	64 × 114	<7.97	con	64 × 114	<8.80	con	64 × 114	<28.7	con	64 × 114	65200	54500
Sgr B1 Ext1	26.0	<2.27	con	26.0	<2.54	con	26.0	8940	6610	26.0	21000	16300
Sgr B1 E	23.0	<3.18	con	23.0	4460	3250	23.0	15000	12200	23.0	36900	30600
Sgr B1 I	35.0	<5.12	con	35.0	7410	3920	35.0	21500	16800	35.0	49200	39000
Sgr B1 J	28 × 80	<2.03	UD	28 × 80	<2.13	UD	28 × 80	<6.67	UD	28 × 80	13900	8710

Note. Entries marked with "sat" indicate that the sources are themselves saturated in that band or are affected by array saturation effects from nearby bright sources. Entries marked with "con" indicate that the total measured emission is dominated by contamination from (most likely foreground) stars. For upper limits, UR means the source is unresolved from a much brighter nearby source or extended emission, and UD means the source is not undetected. For all undetected sources (as well as unresolved sources), there is significant background emission or contamination from nearby sources, such that the flux upper limit given is the measured flux in the indicated aperture. For saturated sources, we use the point source saturation fluxes of 190, 200, 1400, and 740 mJy at 3.6, 4.5, 5.8, and 8.0 μm, respectively (from the Spitzer Observer's Manual, Version 7.1.), as lower limits in the SED modeling.

Table 7
Spitzer-IRAC Observational Parameters of Sources in Sgr B2

Source	3.6 μm			4.5 μm			5.8 μm			8.0 μm		
	R_{int} (arcsec)	F_{int} (mJy)	$F_{int\text{-}bg}$ (mJy)	R_{int} (arcsec)	F_{int} (mJy)	$F_{int\text{-}bg}$ (mJy)	R_{int} (arcsec)	F_{int} (mJy)	$F_{int\text{-}bg}$ (mJy)	R_{int} (arcsec)	F_{int} (mJy)	$F_{int\text{-}bg}$ (mJy)
Compact Sources												
Sgr B2 1	4.8	<10.8	UD	4.8	14.9	1.43	4.8	70.5	10.7	4.8	167	34.4
Sgr B2 2	6.0	<77.3	UD	6.0	<105	UD	6.0	<174	UD	6.0	<237	UD
Sgr B2 3	4.8	<16.1	UD	4.8	<18.8	UD	4.8	<78.8	UD	4.8	<152	UD
Sgr B2 AA	4.8	<18.0	UD	4.8	30.2	17.2	6.0	155	62.3	6.0	336	153
Sgr B2 4	8.4	<104	UD	8.4	<88.5	UD	8.4	<190	UD	8.4	<242	UD
Sgr B2 H	6.0	69.3	40.7	6.0	216	181	6.0	496	359	6.0	772	517
Sgr B2 5	4.8	29.5	11.6	4.8	32.9	13.9	4.8	126	32.1	4.8	273	88.0
Sgr B2 6	4.8	43.6	26.2	4.8	30.2	17.3	4.8	75.1	13.4	4.8	138	17.0
Sgr B2 BB	9.6	<117	UD	9.6	148	91.1	12.0	610	273	12.0	1440	840
Sgr B2 L	6.0	<26.7	UD	6.0	32.2	12.8	7.2	147	41.5	7.2	237	69.4
Sgr B2 7	6.0	<33.2	UD	6.0	<30.6	UD	6.0	131	11.8	6.0	281	33.8
Sgr B2 O	7.2	<35.7	UD	7.2	52.6	17.2	8.4	255	58.9	8.4	581	166
Sgr B2 8	7.2	45.9	13.5	7.2	60.4	24.4	8.4	280	94.6	8.4	657	268
Sgr B2 9	4.8	<28.8	UD	4.8	38.7	11.1	4.8	109	29.4	6.0	312	90.9
Sgr B2 P	4.8	29.5	8.75	4.8	63.5	45.3	7.2	278	131	7.2	715	397
Sgr B2 R	9.6	86.1	16.1	9.6	196	115	10.8	729	362	10.8	2070	1330
Sgr B2 10	4.8	54.8	26.1	6.0	128	68.5	6.0	328	149	6.0	729	303
Sgr B2 11	4.8	44.6	24.6	6.0	57.6	22.9	6.0	150	28.4	6.0	333	90.9
Sgr B2 12	4.8	35.8	7.42	4.8	49.5	10.5	7.2	334	285	7.2	742	93.2
Sgr B2 13	4.8	27.1	4.69	4.8	36.1	10.7	4.8	159	18.6	7.2	674	165
Sgr B2 14	9.6	217	141	9.6	296	186	9.6	721	347	9.6	1540	586
Sgr B2 15	6.0	781	729	6.0	1020	958	6.0	1960	1730	6.0	1430	967
Sgr B2 16	6.0	78.4	35.8	6.0	89.2	46.0	8.4	614	305	8.4	1190	519
Sgr B2 17	8.4	120	17.6	9.6	257	84.5	9.6	683	145	9.6	1640	497
Extended Sources												
Sgr B2 V	27.0	<1.00	con	27.0	1760	1310	27.0	5290	3220	27.0	12800	10400
Sgr B2 Main	27.0	<0.918	UD	27.0	<0.983	con	27.0	<3.18	con	27.0	4860	2510
Sgr B2 Ext1	28x50	<0.831	UD	28x50	<1.02	con	28x50	3250	1910	28x50	7720	5260
Sgr B2 Ext2	197.0	<1.07	con	197.0	1540	1080	197.0	3720	2140	197.0	8010	6270

Note. See table notes from Table 6.

Table 8
Spitzer-IRAC Observational Parameters of Sources in Sgr C

Source	3.6 μm			4.5 μm			5.8 μm			8.0 μm		
	R_{int} (arcsec)	F_{int} (mJy)	$F_{int\text{-}bg}$ (mJy)	R_{int} (arcsec)	F_{int} (mJy)	$F_{int\text{-}bg}$ (mJy)	R_{int} (arcsec)	F_{int} (mJy)	$F_{int\text{-}bg}$ (mJy)	R_{int} (arcsec)	F_{int} (mJy)	$F_{int\text{-}bg}$ (mJy)
Compact Sources												
Sgr C 1	3.0	22.9	4.17	4.2	49.2	13.4	5.4	413	75.2	7.2	1910	304
Sgr C 2	8.4	292	128	9.0	431	211	10.8	1680	441	12.0	5130	1090
Sgr C 3	6.0	<101	UR	6.0	118	46.1	6.0	445	67.1	6.6	1370	113
Sgr C 4	4.8	<58.6	UR	4.8	<58.5	UR	4.8	322	41.6	5.4	1080	72.0
Sgr C 5	10.2	<3000	UR	10.2	<355	UD	10.2	1580	251	10.8	4540	632
Sgr C 6	4.8	53.0	14.5	6.0	113	46.9	7.8	764	128	8.4	2190	297
Sgr C 7	3.0	25.6	8.86	4.8	64.4	14.7	6.0	471	59.6	6.0	1310	157
Sgr C 8	7.2	<159	UD	7.2	<182	UD	7.2	668	98.4	8.4	2450	385
Sgr C 9	4.2	<31.7	UD	4.2	<33.5	UD	4.2	<189	UD	4.2	521	103
Sgr C 10	4.2	35.4	14.3	4.2	64.2	32.5	4.8	342	87.4	4.8	916	200
Sgr C 11	3.0	126	109	3.6	317	289	4.2	797	602	5.4	1750	903
Sgr C 12	4.8	142	81.4	4.8	151	85.6	6.0	631	142	6.0	1620	423
Sgr C 13	2.4	10.5	3.40	2.4	12.9	4.10	3.0	102	30.9	3.6	367	64.1
Sgr.C 14	3.0	<9.91	UD	3.0	<15.2	UR	3.0	71.7	15.7	3.0	202	31.4
Sgr C H3	4.8	<42.4	UR	4.8	192	157	4.8	421	274	4.8	610	218
Sgr C H4	3.6	<24.2	UR	3.6	<81.3	UR	3.6	<129	UR	3.6	<215	UD
Sgr C H1	3.0	<17.2	UR	3.0	<20.4	UR	3.0	83.3	27.1	4.2	384	93.9
Sgr C 15	7.2	<130	UR	7.2	<124	UR	7.2	540	25.1	8.4	1970	188
Sgr C 16	6.0	<80.9	UR	6.0	<79.0	UR	6.0	446	24.3	8.4	2180	628
Extended Sources												
Sgr C H II	83.6	20200	8480	83.6	21100	6560	83.6	82400	47300	83.6	212000	123000

Notes. UR and UD have the same meanings as given in the caption of Table 6. For these sources, the F_{int} value is used as the upper limit in the SED modeling.

Table 9
Herschel-PACS Observational Parameters of Sources in Sgr B1

Source	70 μm			160 μm		
	R_{int} (arcsec)	F_{int} (Jy)	$F_{int\text{-}bg}$ (Jy)	R_{int} (arcsec)	F_{int} (Jy)	$F_{int\text{-}bg}$ (Jy)
Compact Sources						
Sgr B1 A	22.4	<963	UR	22.4	<1020	UR
Sgr B1 C	16.0	<395	UR	22.4	<933	UD
Sgr B1 D	16.0	<685	UR	22.4	<1100	UR
Sgr B1 1	16.0	<699	UR	22.4	<1060	UD
Sgr B1 2	16.0	<404	UR	22.4	<868	UD
Sgr B1 F	16.0	<429	UR	22.4	<1070	UD
Sgr B1 G	16.0	<579	UR	22.4	<1050	UD
Sgr B1 H	22.4	<813	UR	22.4	<1300	UD
Sgr B1 3	16.0	<419	UR	22.4	<1140	UD
Sgr B1 4	16.0	<545	UR	22.4	<916	UR
Sgr B1 5	16.0	<550	UR	22.4	<856	UR
Sgr B1 6	16.0	<560	UR	22.4	<871	UR
Sgr B1 7	16.0	<561	UR	22.4	<857	UD
Sgr B1 8	16.0	<526	UD	22.4	<929	UD

Table 9
(Continued)

Source	70 μm			160 μm		
	R_{int} (arcsec)	F_{int} (Jy)	$F_{int\text{-}bg}$ (Jy)	R_{int} (arcsec)	F_{int} (Jy)	$F_{int\text{-}bg}$ (Jy)
Sgr B1 9	16.0	<457	UR	22.4	<829	UD
Sgr B1 10	16.0	<359	UR	22.4	<921	UD
Sgr B1 11	16.0	<479	UD	22.4	<903	UD
Sgr B1 12	16.0	<408	UR	22.4	<831	UR
Extended Sources						
Ionized Bar	143 × 40	4020	3180	143 × 40	<3580	UD
Ionized Rim	64 × 114	5320	2120	64 × 114	<4650	UD
Sgr B1 Ext1	26.1	1700	1280	26.1	<1450	UD
Sgr B1 E	23.0	1340	744	23.0	<1070	UD
Sgr B1 I	35.0	2580	1800	35.0	<2070	UD
Sgr B1 J	28 × 80	1160	699	28 × 80	<1390	UD

Notes. UR and UD have the same meanings as given in the caption of Table 6. For these sources, the F_{int} value is used as the upper limit in the SED modeling.

Table 10
Herschel-PACS Observational Parameters of Sources in Sgr B2

Source	70 μm			160 μm		
	R_{int} (arcsec)	F_{int} (Jy)	$F_{int\text{-}bg}$ (Jy)	R_{int} (arcsec)	F_{int} (Jy)	$F_{int\text{-}bg}$ (Jy)
Compact Sources						
Sgr B2 1	16.0	<325	UR	22.4	<2060	UD
Sgr B2 2	16.0	<533	UR	22.4	<5320	UD
Sgr B2 3	16.0	<528	UR	22.4	<4700	UR
Sgr B2 AA	16.0	<411	UR	22.4	<4020	UR
Sgr B2 4	19.2	<2420	UR	sat	sat	sat
Sgr B2 H	16.0	<3550	UR	22.4	<10900	UR
Sgr B2 5	16.0	<2270	UD	22.4	<8180	UD
Sgr B2 6	16.0	<310	UR	22.4	<3810	UR
Sgr B2 BB	16.0	<1040	UR	22.4	<4230	UR
Sgr B2 L	16.0	<695	UR	22.4	<4850	UR
Sgr B2 7	16.0	<249	UR	22.4	<2300	UR
Sgr B2 O	16.0	<1400	UR	22.4	<3410	UR
Sgr B2 8	16.0	<661	UR	22.4	<3590	UD
Sgr B2 9	16.0	<846	UR	22.4	<3150	UD
Sgr B2 P	16.0	<715	UR	22.4	<3090	UD
Sgr B2 R	19.2	<949	UR	22.4	<2600	UR
Sgr B2 10	16.0	<375	UR	22.4	<1510	UR
Sgr B2 11	16.0	<262	UR	22.4	<1470	UD
Sgr B2 12	16.0	<391	UR	22.4	<1290	UD
Sgr B2 13	16.0	<342	UR	22.4	<1460	UR
Sgr B2 14	16.0	<325	UR	22.4	<1560	UD
Sgr B2 15	16.0	<395	UD	22.4	<1300	UD
Sgr B2 16	19.2	<470	UR	22.4	<1390	UR
Sgr B2 17	16.0	<308	UR	22.4	<942	UR
Extended Sources						
Sgr B2 V	27.0	1250	905	27.0	2830	1100
Sgr B2 Main	27.0	13400	13100	27.0	sat	sat
Sgr B2 Ext1	28 × 50	783	545	28 × 50	<1150	UD
Sgr B2 Ext2	19.2	454	257	19.2	<724	UD

Note. UR and UD have the same meanings as given in the caption of Table 6. For these sources, the F_{int} value is used as the upper limit in the SED modeling. Sgr B2 K is saturated ("sat"), so for this target only, we use the point source saturation flux of 1125 Jy at 160 μm (from the PACS Observer's Manual, Version 2.5.1) as a lower limit in the SED modeling.

Table 11
Herschel-PACS Observational Parameters of Sources in Sgr C

Source	70 μm			160 μm		
	R_{int} (arcsec)	F_{int} (Jy)	$F_{int\text{-}bg}$ (Jy)	R_{int} (arcsec)	F_{int} (Jy)	$F_{int\text{-}bg}$ (Jy)
Compact Sources						
Sgr C 1	16.0	<433	UR	22.4	<841	UD
Sgr C 2	16.0	<368	UD	22.4	<737	UD
Sgr C 3	16.0	<402	UR	22.4	<721	UR
Sgr C 4	16.0	<505	UD	22.4	<736	UD
Sgr C 5	16.0	<573	UR	22.4	<776	UR
Sgr C 6	16.0	<365	UR	22.4	<794	UD
Sgr C 7	16.0	<605	UR	22.4	<717	UD
Sgr C 8	16.0	<618	UR	22.4	<681	UD
Sgr C 9	16.0	<352	UR	22.4	<798	UR
Sgr C 10	16.0	<382	UR	22.4	<736	UD
Sgr C 11	16.0	<417	UR	22.4	<794	UR
Sgr C 12	16.0	<470	UR	22.4	<674	UD
Sgr C 13	16.0	<805	UR	22.4	<1850	UD
Sgr C 14	16.0	<951	UR	22.4	<2000	UD
Sgr C H3	16.0	<1020	UR	28.8	<2870	UR
Sgr C H4	16.0	<696	UR	22.4	<2270	UR
Sgr C H1	16.0	<369	UR	22.4	<1860	UR
Sgr C 15	16.0	<350	UR	22.4	<703	UD
Sgr C 16	16.0	<363	UR	22.4	<676	UD
Extended Sources						
HII Region	83.2	13000	12200	83.2	12000	11700

Note. UR and UD have the same meanings as given in the caption of Table 6. For these sources, the F_{int} value is used as the upper limit in the SED modeling.

Appendix C
Observational and Derived Parameters for Other Regions Covered in the SOFIA Data

Within the confines of the FORCAST data covering the Sgr B1 and Sgr B2 GH II regions, there is an additional region named G0.6-0.0 where we find several MYSO candidates. Since

Table 12
SOFIA Observational Parameters of Sources in Other Regions

Source	R.A. (J2000)	Decl. (J2000)	25 μm			37 μm			Aliases
			R_{int} (arcsec)	F_{int} (Jy)	F_{int-bg} (Jy)	R_{int} (arcsec)	F_{int} (Jy)	F_{int-bg} (Jy)	
G0.6-0.0 Compact Sources									
G0.6-0.0 1	17 47 09.90	−28 27 54.2	14.6	62.1	30.8	16.9	139	73.8	...
G0.6-0.0 A	17 47 11.28	−28 26 31.2	8.4	24.0	12.6	10.0	57.9	37.8	...
G0.6-0.0 2	17 47 13.08	−28 26 05.0	6.1	4.49	1.19	6.1	8.19	3.17	SSTGC773332[b]
G0.6-0.0 3	17 47 13.15	−28 27 00.3	5.4	13.7	4.36	5.4	42.5	21.0	...
G0.6-0.0 B	17 47 13.73	−28 26 53.4	6.9	68.9	45.9	6.9	158	106	...
G0.6-0.0 C	17 47 14.67	−28 26 48.7	7.7	103	78.0	7.7	228	168	...
G0.6-0.0 D	17 47 15.42	−28 26 42.5	6.1	22.5	14.5	6.1	48.7	21.6	...
G0.6-0.0 4	17 47 15.76	−28 26 10.3	6.1	7.11	2.14	6.9	18.6	5.24	SSTGC779211[b]
G0.6-0.0 5	17 47 16.81	−28 26 11.0	10.7	25.5	13.5	10.7	46.1	22.5	...
G0.6-0.0 6	17 47 18.75	−28 27 28.5	11.5	35.8	23.4	12.3	83.3	53.9	...
G0.6-0.0 7	17 47 20.13	−28 26 06.3	6.9	6.57	2.01	8.4	11.6	5.06	...
G359.38-0.08 Compact Sources									
G359.38-0.08 1	17 44 22.68	−29 32 09.5	12.3	19.0	8.38	15.3	43.0	32.2	...
G359.38-0.08 2	17 44 23.33	−29 31 01.1	10.0	15.6	6.67	9.2	25.3	9.24	...
G359.38-0.08 3	17 44 23.92	−29 30 44.3	3.1	1.48	0.403	5.4	7.83	1.37	...
G359.38-0.08 4	17 44 24.86	−29 29 34.4	4.6	2.13	0.80	3.8	1.37	0.659	...
G359.38-0.08 5	17 44 25.80	−29 30 46.6	15.3	61.5	26.6	15.3	144	59.3	...
G359.38-0.08 6	17 44 26.57	−29 30 02.8	9.2	14.6	3.03	10.0	38.3	6.99	SSTGC330325[b]
G359.38-0.08 7	17 44 28.74	−29 29 55.1	12.3	33.3	13.6	13.8	73.1	22.0	...
G359.38-0.08 8	17 44 29.10	−29 30 29.7	6.9	5.31	1.09	6.9	15.2	4.81	...
G359.38-0.08 9	17 44 31.27	−29 29 36.7	9.2	11.3	1.79	10.7	33.5	4.68	...
G359.38-0.08 10	17 44 33.45	−29 29 50.5	10.7	20.2	8.72	10.7	37.6	13.4	...
G359.38-0.08 Extended Sources									
G359.38-0.08 HII	17 44 28.03	−29 30 19.2	82.1	731	550	82.1	1300	1270	...
G359.42-0.02 Compact Sources									
G359.42-0.02 1	17 44 11.22	−29 26 38.4	8.4	7.14	7.12	8.4	16.3	10.4	SSTGC293528[a]
G359.42-0.02 2	17 44 12.69	−29 26 56.1	5.4	5.82	5.50	6.9	7.59	5.02	...
G359.42-0.02 3	17 44 17.69	−29 27 12.3	10.7	23.3	20.1	11.5	53.2	44.6	...
G359.42-0.02 4	17 44 19.10	−29 27 26.1	7.7	3.34	1.83	7.7	8.96	3.05	...
G359.42-0.02 5	17 44 21.45	−29 27 36.9	13.8	32.2	21.5	15.3	81.0	59.3	...
G359.42-0.02 6	17 44 22.57	−29 25 17.9	10.0	5.92	5.80	10.0	9.11	8.07	SSTGC320517[b]
G359.42-0.02 7	17 44 22.98	−29 27 04.6	5.4	3.01	1.67	6.9	4.78	3.09	
G359.42-0.02 8	17 44 28.21	−29 26 33.1	3.1	1.44	0.833	3.8	1.41	1.18	SSTGC335380[b]
G359.50-0.09 Compact Sources									
G359.50-0.09 1	17 44 41.38	−29 25 12.4	10.0	10.0	4.44	10.0	30.2	10.2	...
G359.50-0.09 2	17 44 41.55	−29 24 30.2	14.6	38.9	25.5	15.3	97.5	44.1	SSTGC368854[a]
G359.50-0.09 3	17 44 41.79	−29 23 31.8	6.1	3.57	2.12	9.2	14.4	6.97	SSTGC370438[a,b]
G359.50-0.09 4	17 44 42.73	−29 23 15.7	6.1	3.00	1.89	6.9	7.62	3.27	SSTGC372630[a,b]
G359.50-0.09 5	17 44 44.49	−29 23 21.0	3.8	0.887	0.518	3.8	1.81	0.576	...
G359.50-0.09 6	17 44 46.78	−29 23 44.8	6.1	9.15	5.82	6.1	16.1	11.5	...
G359.50-0.09 7	17 44 47.02	−29 23 35.6	6.1	8.15	5.35	6.1	14.4	8.39	...
G359.50-0.09 8	17 44 48.84	−29 23 41.7	7.7	12.7	7.04	7.7	22.0	12.7	SSTGC388790[a]
G359.50-0.09 9	17 44 51.19	−29 24 52.4	5.4	17.2	15.8	6.1	9.16	8.24	
G359.50-0.09 10	17 44 53.13	−29 24 31.6	3.8	3.27	1.55	6.1	4.67	3.25	SSTGC400062[b]

Notes.
[a] From D. An et al. (2011).
[b] From F. Yusef-Zadeh et al. (2009).

knowledge of the existence of any YSOs in the Galactic CMZ is of interest, we have derived photometry values and run SED models for all MYSO candidates in G0.6-0.0. Likewise, we defined three regions likely not directly related to the Sgr C GH II region but close enough to be within the confines of our FORCAST maps: G359.38-0.08, G359.42-0.02, and G359.50-0.09. All four of these satellite regions also contain MYSO candidates, and so they too have had their photometry values measured and modeled.

For all four regions, Table 12 gives the photometry data for all sources identified in the SOFIA-FORCAST data.

Table 13
Spitzer-IRAC Observational Parameters of Sources in Other Regions

Source	3.6 μm			4.5 μm			5.8 μm			8.0 μm		
	R_{int} (arcsec)	F_{int} (mJy)	$F_{int\text{-}bg}$ (mJy)	R_{int} (arcsec)	F_{int} (mJy)	$F_{int\text{-}bg}$ (mJy)	R_{int} (arcsec)	F_{int} (mJy)	$F_{int\text{-}bg}$ (mJy)	R_{int} (arcsec)	F_{int} (mJy)	$F_{int\text{-}bg}$ (mJy)
G0.6-0.0 Compact Sources												
G0.6-0.0 1	4.8	51.1	7.31	4.8	58.3	7.17	4.8	197	22.0	4.8	811	309
G0.6-0.0 A	4.8	17.2	8.26	6.0	77.7	57.4	6.0	272	165	6.0	907	635
G0.6-0.0 2	4.8	16.2	2.99	4.8	22.1	4.18	4.8	89.3	4.49	4.8	203	9.18
G0.6-0.0 3	4.8	50.8	12.9	4.8	79.0	21.1	4.8	341	85.2	4.8	837	156
G0.6-0.0 B	6.0	137	84.0	6.0	405	301	6.0	1430	930	7.2	5000	3150
G0.6-0.0 C	7.2	229	148	7.2	806	662	7.2	2720	2120	7.2	7490	6210
G0.6-0.0 D	4.8	81.9	55.3	4.8	138	75.9	4.8	398	159	4.8	985	420
G0.6-0.0 4	4.8	<19.6	UD	4.8	35.7	7.58	4.8	141	12.3	4.8	345	63.2
G0.6-0.0 5	7.2	76.6	20.8	7.2	115	48.6	8.4	494	98.5	8.4	1170	285
G0.6-0.0 6	7.2	99.6	21.2	7.2	133	41.9	7.2	546	68.3	7.2	1360	161
G0.6-0.0 7	8.4	225	167	8.4	190	136	8.4	494	190	8.4	970	304
G359.38-0.08 Compact Sources												
G359.38-0.08 1	12.0	<388	UR	12.0	<445	UR	12.0	1480	335	12.0	3910	683
G359.38-0.08 2	3.0	<17.4	UD	3.0	<22.6	UD	5.4	252	34.9	6.6	999	82.5
G359.38-0.08 3	6.0	<55.4	UD	6.0	76.3	15.2	6.6	359	48.1	7.2	1200	121
G359.38-0.08 4	3.6	700	669	3.6	708	678	4.2	1140	980	4.2	913	539
G359.38-0.08 5	4.8	<87.3	UD	5.4	150	90.3	7.8	756	246	10.8	3480	603
G359.38-0.08 6	3.0	14.3	3.03	4.2	34.9	6.80	6.6	379	44.7	7.2	1230	141
G359.38-0.08 7	12.0	<4900	UR	12.0	<556	UR	12.0	<1310	UD	12.0	<2830	UD
G359.38-0.08 8	6.6	<73.1	UR	6.6	<70.3	UD	6.6	417	93.4	7.2	1320	333
G359.38-0.08 9	9.0	<1600	UR	9.0	<169	UD	9.0	<579	UD	9.0	<1680	UD
G359.38-0.08 10	5.4	75.3	20	10.8	348	90.9	10.8	1310	321	10.8	3520	835
G359.38-0.08 Extended Sources												
G359.38-0.08 H II	82.2	14800	3460	82.2	16100	2580	82.2	55600	20300	82.2	141000	51300
G359.42-0.02 Compact Sources												
G359.42-0.02 1	3.6	32.8	10.4	7.8	141	31.5	7.8	588	95.5	8.4	1860	360
G359.42-0.02 2	sat	sat	sat	sat	sat	sat	6.6	5330	4860	sat	sat	sat
G359.42-0.02 3	sat	sat	sat	sat	sat	sat	6.0	2270	1920	6.6	3670	2610
G359.42-0.02 4	3.6	<29.0	UR	3.6	38.6	13.6	4.2	197	27.4	4.2	546	84.2
G359.42-0.02 5	10.8	<385	UR	10.8	396	184	12.0	1630	423	13.8	5470	852
G359.42-0.02 6	9.6	883	UR	9.6	<761	UR	9.6	<1380	UR	9.6	2660	709
G359.42-0.02 7	3.6	25.1	9.85	4.2	38.1	15.9	4.2	138	27.7	5.4	629	63.5
G359.42-0.02 8	4.8	<38.8	UR	4.8	66.2	40.0	4.8	209	90.6	4.8	626	243
G359.50-0.09 Compact Sources												
G359.50-0.09 1	10.2	<330	UR	10.2	<320	UR	10.2	1790	384	10.2	3860	327
G359.50-0.09 2	12.0	<598	UR	12.0	<595	UR	12.0	2360	433	14.4	8690	1520
G359.50-0.09 3	5.4	<59.4	UR	5.4	71.0	21.3	5.4	344	39.7	6.0	1190	194
G359.50-0.09 4	4.2	62.7	23.8	6.0	150	64.8	7.2	693	164	7.2	1850	402
G359.50-0.09 5	3.6	318	282	4.2	558	509	4.8	1100	869	5.4	1490	656
G359.50-0.09 6	5.4	<500	UR	5.4	519	406	5.4	1040	552	5.4	2030	1060
G359.50-0.09 7	4.2	107	51.2	4.2	129	70.1	5.4	691	345	5.4	1670	660
G359.50-0.09 8	3.6	82.8	45.4	4.8	170	115	4.8	479	223	5.4	1470	579
G359.50-0.09 9	sat	sat	sat	sat	sat	sat	sat	sat	sat	sat	sat	sat
G359.50-0.09 10	4.8	46.0	7.46	4.8	59.5	17.2	6.6	416	73.0	6.0	972	156

Note. See table notes from Table 6.

Tables 13 and 14 give the photometry information for those same sources from the Spitzer-IRAC data and Herschel-PACS data, respectively. While the resultant physical values of the SED model fitting are given in Table 15 for all satellite regions, Figure 17 displays the SED plots for all compact mid-infrared sources in G0.6-0.0, whereas Figure 18 displays them for all of the compact sources in G359.38-0.08, G359.42-0.02, and G359.50-0.09.

The results of these SED model fits imply that there is a significant level of massive star formation that may be occurring outside of but near the major sites of star formation (i.e., Sgr B1, Sgr B2, and Sgr C). In total, 39 compact mid-

Table 14
Herschel-PACS Observational Parameters of Sources in Other Regions

Source	70 μm			160 μm		
	R_{int} (arcsec)	F_{int} (Jy)	$F_{int\text{-}bg}$ (Jy)	R_{int} (arcsec)	F_{int} (Jy)	$F_{int\text{-}bg}$ (Jy)
G0.6-0.0 Compact Sources						
G0.6-0.0 1	16	<409	UR	22.4	<1030	UD
G0.6-0.0 A	16	<618	UR	22.4	<2190	UR
G0.6-0.0 2	16	<486	UD	22.4	<1920	UD
G0.6-0.0 3	16	<972	UR	22.4	<2090	UD
G0.6-0.0 B	16	<1300	UR	22.4	<2370	UD
G0.6-0.0 C	16	<1440	UR	22.4	<2610	UR
G0.6-0.0 D	16	<1110	UR	22.4	<2520	UR
G0.6-0.0 4	16	<434	UR	22.4	<1910	UD
G0.6-0.0 5	16	<392	UR	22.4	<2200	UD
G0.6-0.0 6	16	<462	UR	22.4	<1530	UR
G0.6-0.0 7	16	<317	UR	22.4	<2440	UR
G359.38-0.08 Compact Sources						
G359.38-0.08 1	22.4	<491	UR	22.4	<585	UD
G359.38-0.08 2	16.0	<306	UR	22.4	<766	UD
G359.38-0.08 3	16.0	<342	UR	22.4	<786	UR
G359.38-0.08 4	16.0	<281	UR	22.4	<688	UD
G359.38-0.08 5	16.0	<378	UR	22.4	<786	UD
G359.38-0.08 6	16.0	<345	UR	22.4	<688	UD
G359.38-0.08 7	16.0	<317	UR	22.4	<650	UD
G359.38-0.08 8	16.0	<331	UR	22.4	<710	UR
G359.38-0.08 9	16.0	<316	UR	22.4	<641	UD
G359.38-0.08 10	16.0	<356	UR	22.4	<670	UD
G359.38-0.08 Extended Sources						
G359.38-0.08 HII	83.2	8250	7520	83.2	9710	8910
G359.42-0.02 Compact Sources						
G359.42-0.02 1	16.0	<269	UR	22.4	<674	UD
G359.42-0.02 2	16.0	<284	UR	22.4	<699	UD
G359.42-0.02 3	19.2	<379	UR	22.4	<659	UR
G359.42-0.02 4	16.0	<264	UD	22.4	<628	UD
G359.42-0.02 5	16.0	<312	UR	22.4	<686	UD
G359.42-0.02 6	16.0	<210	UR	22.4	<474	UD
G359.42-0.02 7	16.0	<252	UR	22.4	<720	UD
G359.42-0.02 8	16.0	<233	UR	22.4	<853	UD
G359.50-0.09 Compact Sources						
G359.50-0.09 1	16.0	<362	UR	22.4	<723	UD
G359.50-0.09 2	22.4	<737	UR	22.4	<758	UR
G359.50-0.09 3	22.4	<648	UR	22.4	<877	UD
G359.50-0.09 4	16.0	<345	UR	22.4	<871	UD
G359.50-0.09 5	16.0	<320	UD	22.4	<745	UD
G359.50-0.09 6	16.0	<339	UR	22.4	<617	UD
G359.50-0.09 7	16.0	<332	UR	22.4	<618	UD
G359.50-0.09 8	16.0	<307	UR	22.4	<642	UD
G359.50-0.09 9	16.0	<254	UR	22.4	<898	UD
G359.50-0.09 10	16.0	<268	UR	22.4	<883	UR

Note. UR and UD have the same meanings as given in the caption of Table 6. For these sources, the F_{int} value is used as the upper limit in the SED modeling.

infrared sources are found throughout the combined area of these four (non-GH II) regions, with 1 confirmed MYSO, 8 Likely MYSOs, and 18 Possible MYSOs (see Table 15).

C.1. G0.6-0.0 MYSO Candidates

The close (but likely separate) region just to the south of Sgr B2, G0.6-0.0, has 11 compact mid-infrared sources, of which 4 were previously identified in radio cm continuum (e.g., D. M. Mehringer et al. 1992). We identify seven new compact infrared sources, one (G0.6-0.0 2) which is likely a low- or intermediate-mass YSO (based on the SED fitting) and one with radio continuum that was not previously identified in radio studies (G0.6-0.0 4). In this area alone, we find one confirmed MYSO, four Likely MYSOs, and five Possible MYSOs (Table 15). In all, 91% of the mid-infrared sources in G0.6-0.0 are MYSOs or MYSO Candidates. The most massive MYSO candidates are G0.6-0.0 B and G0.6-0.0 C, each with a best-fit mass of 64 $M_{\odot}$, with G0.6-0.0 C having the highest fit of all sources we studied in the CMZ, with a value of 96 $M_{\odot}$ in its range of best-fit masses.

C.2. G359.38-0.08 MYSO Candidates

Southwest of the Sgr C GH II region, G359.38-0.08 has 10 compact mid-infrared sources among some faint and extended dust emission regions (interspersed with diffuse cm radio continuum emission as well), which may signal that this is a legitimate star-forming region. There are no confirmed MYSOs among the mid-infrared sources, but we do find four sources that we consider to be Likely MYSOs based on the presence of cm radio continuum emission (Table 15). An additional three sources are listed as Possible MYSOs. We include G359.38-0.08 6 among the Possible MYSO candidates, even though its best-fit model is only 2 $M_{\odot}$, because the other 14 fits in the group of best fits are 8–16 $M_{\odot}$. In all, 70% of the mid-infrared sources in G359.38-0.08 are MYSOs or MYSO Candidates. The most massive MYSO candidate is G359.38-0.08 10 with a best-fit mass of 48 $M_{\odot}$.

C.3. G359.42-0.02 MYSO Candidates

G359.42-0.02 is located west of the Sgr C GH II region, and while we find eight compact mid-infrared sources here, it does not contain any other star formation region signatures (e.g., an IRDC, molecular cloud, extended cm radio continuum or mid-infrared continuum regions, or masers). This region has no confirmed MYSOs or Likely MYSOs, and only contains four Possible MYSOs. The other half (four) of the mid-infrared sources are not thought to be MYSOs. G359.42-0.02 1, though it is well-fit with MYSO models and is the only source in the region with cm radio continuum emission, was not found to have a 15.4 μm ice feature in its spectrum, which is a YSO indicator (D. An et al. 2011). It may be a rare MYSO without this spectral feature, and thus it is labeled as not being an MYSO with a question mark in Table 15. G359.42-0.02 2 has a decreasing flux with infrared wavelength, atypical of MYSOs, and indeed is coincident with a (likely foreground) KM giant star (D. Jang et al. 2022). Sources G359.42-0.02 6 and G359.42-0.02 8 have flat fluxes with wavelength, again atypical of MYSOs, along with SED fits that are less than 8 $M_{\odot}$, and thus they are not likely to be MYSOs. In all, 50% of the mid-infrared sources in G359.42-0.02 are MYSO Candidates, with the most massive being G359.42-0.02 3 with a mass of 32 $M_{\odot}$.

Table 15
SED Fitting Parameters of Compact Infrared Sources in Other Region

Source	L_{obs} ($\times 10^3 L_\odot$)	L_{tot} ($\times 10^3 L_\odot$)	A_v (mag)	M_{star} ($M_\odot$)	A_v Range (mag)	M_{star} Range ($M_\odot$)	Best Models	Well Fit?	Reso-lved?	Features	MYSO?
G0.6-0.0											
G0.6-0.0 1	23.3	38.1	7.9	12	5.3–13	12–12	12	Y	Y	70	Possible
G0.6-0.0 A	10.2	189	53	24	27–92	8–32	8	Y	Y	ice,cm,70	Yes
G0.6-0.0 2	0.78	1.69	8.4	4	8.4–63	4–8	6	Y	Y		No[a]
G0.6-0.0 3	5.49	158	130	32	98–212	12–32	5	Y	Y	70	Possible
G0.6-0.0 B	31.4	858	53	64	50–80	16–64	5	Y	Y	cm,70	Likely
G0.6-0.0 C	39.1	858	53	64	1.7–67	24–96	9	Y	Y	cm,70	Likely
G0.6-0.0 D	6.87	17.0	3.4	12	3.4–16	12–16	6	Y	Y	cm,70?	Likely
G0.6-0.0 4	1.46	19.6	40	12	27–76	8–12	6	Y	Y	cm,70	Likely
G0.6-0.0 5	6.22	17.0	9.2	12	8.4–13	12–12	6	Y	Y	70	Possible
G0.6-0.0 6	13.8	49.1	27	12	2.6–80	12–24	13	Y	Y	ice?,70	Possible
G0.6-0.0 7	1.55	31.4	109	16	55–151	12–32	5	Y	Y	70	Possible
G359.38-0.08											
G359.38-0.08 1	13.3	22.9	74	12	62–183	12–24	8	Y[e]	Y	cm,70	Likely
G359.38-0.08 2	2.80	9.48	24	8	20–27	8–8	7	N[e]	Y	70	No
G359.38-0.08 3	0.69	1.69	159	4	85–204	2–32	12	Y	Y	70	No[a]
G359.38-0.08 4	4.34	24.7	1.7	4	0.8–8.4	2–16	7	N[b]	N	70	No[a]
G359.38-0.08 5	17.6	34.2	4.2	16	3.4–7.5	16–16	7	Y	Y	70	Possible
G359.38-0.08 6	3.83	4.76	27	2	25–106	2–16	15	Y	Y	70	Possible?[a,c]
G359.38-0.08 7	7.52	16.1	5.9	12	5.9–46	8–48	7	Y[e]	Y	cm,70	Likely
G359.38-0.08 8	1.67	11.7	64	8	64–176	8–16	10	Y[e]	Y	cm,70	Likely
G359.38-0.08 9	1.62	31.4	103	16	98–143	16–32	7	Y[e]	Y	cm,70	Likely
G359.38-0.08 10	4.16	344	37	48	6.7–53	8–48	11	Y	Y	70	Possible
G359.42-0.02											
G359.42-0.02 1	5.20	9.67	5.9	8	1.7–23	8–8	7	Y	Y	no ice,cm,70	No?[d]
G359.42-0.02 2	5.28	1200	93	96	8.4–130	2–96	9	Y[b,e]	Y	70	No[a,f]
G359.42-0.02 3	14.9	147	63	32	29–82	12–32	5	Y[e]	Y	70	Possible
G359.42-0.02 4	1.07	13.6	38	12	7.9–38	12–16	7	Y	Y		Possible
G359.42-0.02 5	19.8	47.3	59	12	59–78	12–32	5	Y	Y	70	Possible
G359.42-0.02 6	4.94	3.33	27	4	13–42	4–16	9	Y[b,e]	Y	70	No[a]
G359.42-0.02 7	1.04	31.4	16	16	0.8–52	8–16	11	Y	Y	70	Possible
G359.42-0.02 8	0.69	1200	90	96	37–106	1–96	8	Y[b]	N	70	No[a]
G359.50-0.09											
G359.50-0.09 1	3.36	71.4	46	24	24–83	8–24	7	Y[e]	Y	70	Possible
G359.50-0.09 2	11.6	102	27	16	4.2–34	12–32	15	Y[e]	Y	no ice,70	No?[d]
G359.50-0.09 3	1.90	71.4	70	24	32–80	8–24	7	Y[e]	Y	ice?,70	Possible
G359.50-0.09 4	1.41	158	25	32	8.4–53	12–32	8	Y[e]	Y	ice?,70	Possible
G359.50-0.09 5	3.41	2.31	25	2	17–34	1–16	10	N[b]	N		No[a]
G359.50-0.09 6	4.05	71.4	29	24	13–92	8–24	14	Y	Y	70	Possible
G359.50-0.09 7	2.76	71.4	21	24	1.7–38	8–24	10	Y	Y	70?	Possible
G359.50-0.09 8	3.19	71.4	11	24	2.5–25	16–24	6	Y	Y	no ice,70	No?[f]
G359.50-0.09 9	12.7	1200	16	96	2.6–72	32–96	8	Y[b,e]	N	S,70	No
G359.50-0.09 10	1.03	13.6	55	12	34–140	12–16	9	Y	Y	70	Possible

Notes. Notes are the same as for Table 4. However, in this table, S=SiO masers from T. Fujii et al. (2006).
[a] Has SED model fits less than 8 $M_\odot$. If fit well by the SED fitter, it may be a low-to-intermediate-mass YSO.
[b] This source has a flat or decreasing flux with wavelength and is thus likely not an MYSO.
[c] Most fits imply an MYSO.
[d] Has no 15.4 μm ice feature, but no other indicators point to it not being an MYSO.
[e] Only two nominal data points are used in the SED fitting, and thus the results of the modeling are less reliable.
[f] Spectroscopically determined to be a K or M red giant by D. Jang et al. (2022).

C.4. G359.50-0.09 MYSO Candidates

Located northeast of the Sgr C GH II region, G359.50-0.09 hosts 10 compact mid-infrared sources here, but like G359.42-0.02, it does not contain very many other star formation region signatures, except perhaps some faint and diffuse cm radio continuum emission. This region has no confirmed MYSOs or Likely MYSOs, and only contains six Possible MYSOs. The other four sources are believed to not be MYSOs (Table 15). Both G359.50-0.09 2 and G359.50-0.09 8 were found to not

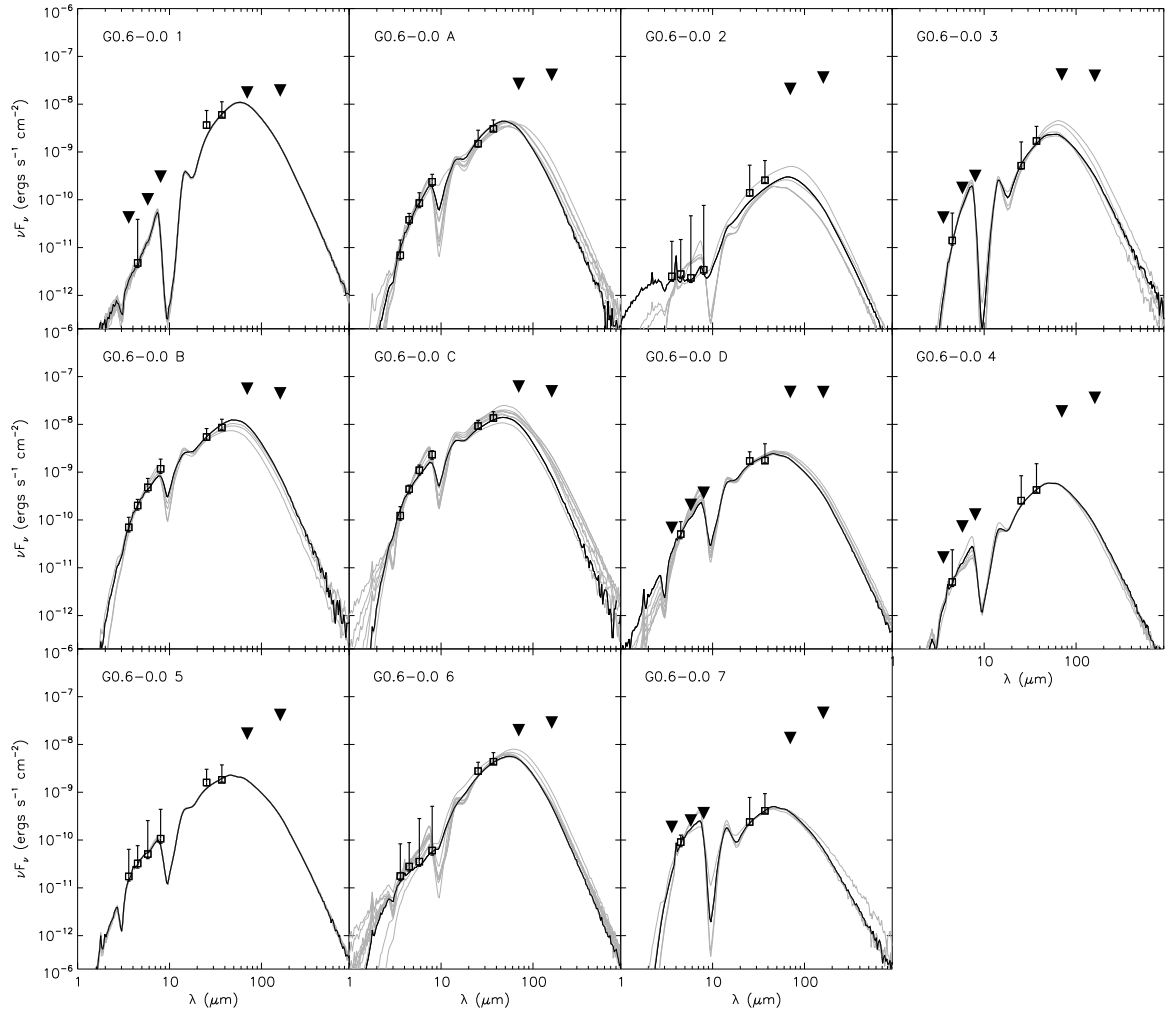

Figure 17. SED fitting with the ZT model for compact sources in G0.6-0.0. Black lines are the best-fit models for the SEDs, and the system of gray lines indicates the remaining fits in the group of best fits (from Table 5). Upside-down triangles are data that are used as upper limits in the SED fits, and upward-facing triangles are lower limits.

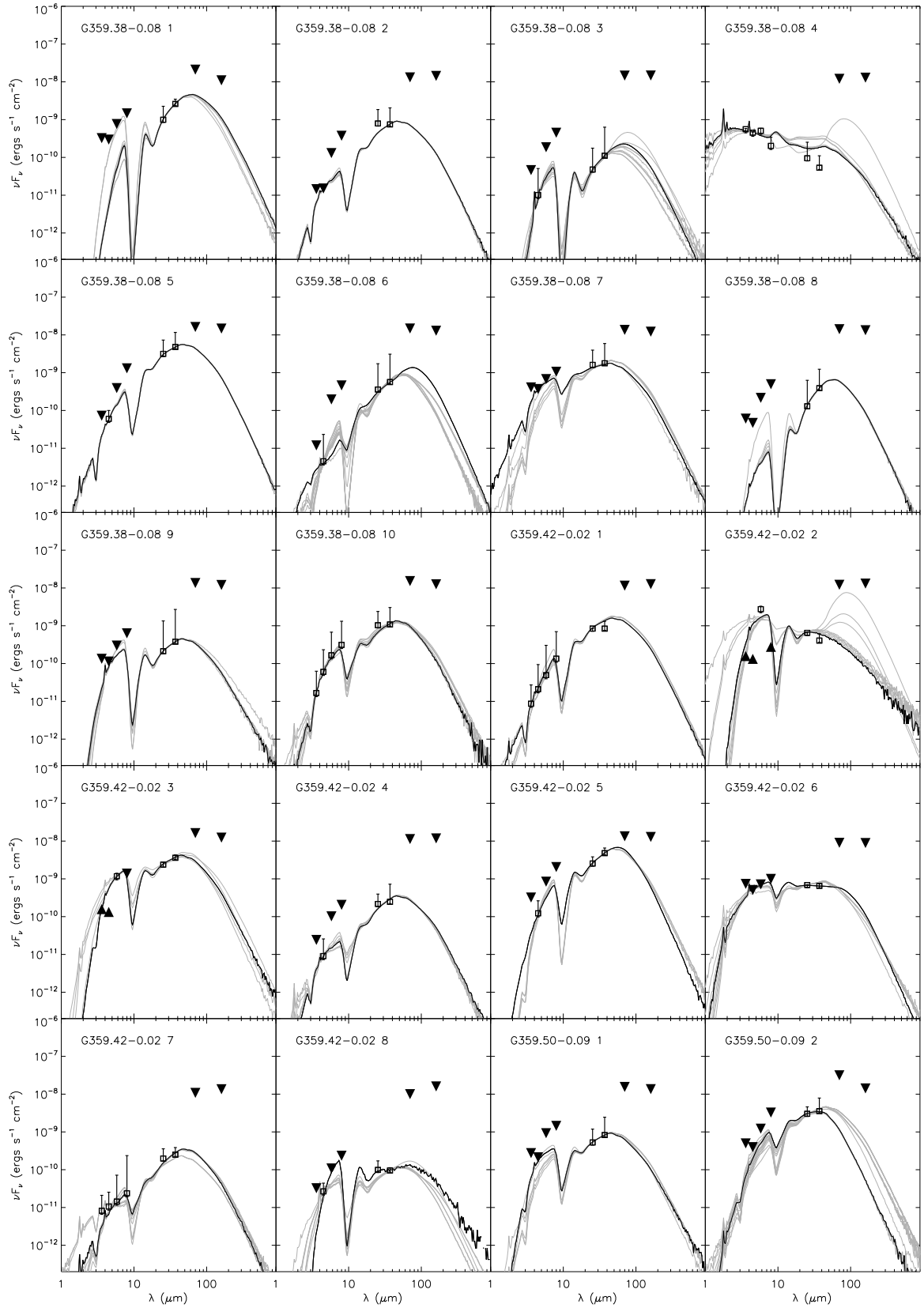

Figure 18. SED fitting with the ZT model for compact sources in G359.38-0.08, G359.42-0.02, and G359.50-0.09. Black lines indicate the best-fit models for the SEDs, and the system of gray lines represent the remaining fits in the group of best fits (from Table 5). Upside-down triangles are data that are used as upper limits in the SED fits, and upward-facing triangles are lower limits.

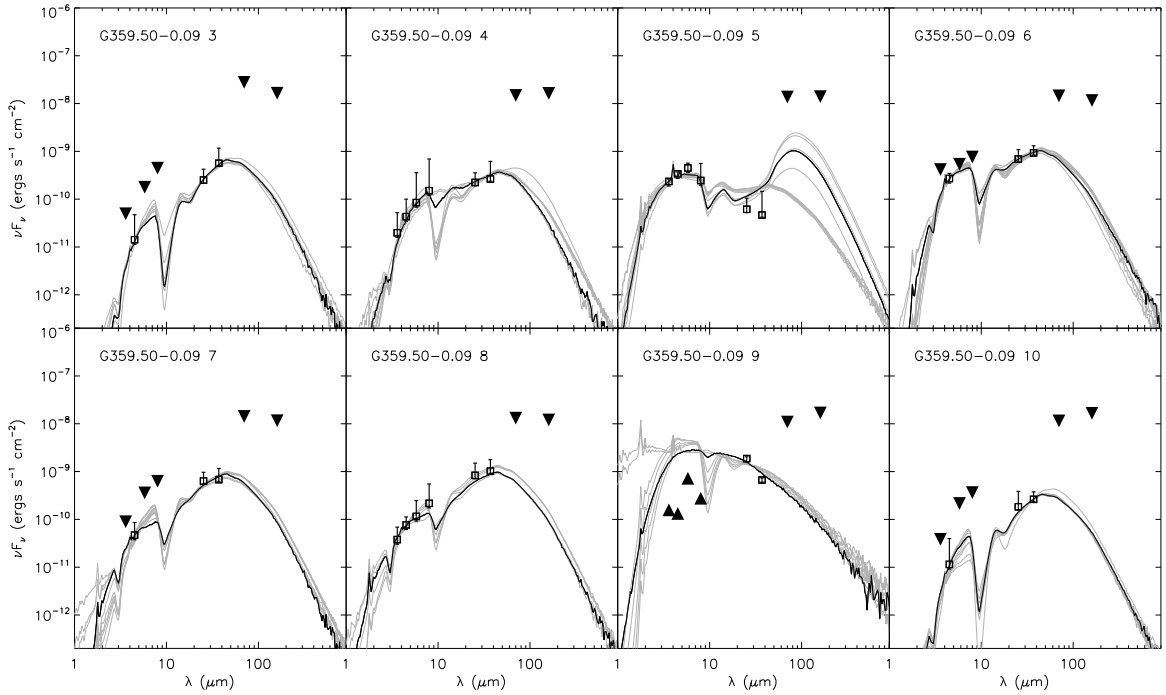

Figure 18. (Continued.)

have 15.4 μm ice features in their spectra (D. An et al. 2011), indicating they are likely not YSOs. Indeed, G359.50-0.09 8 was found by D. Jang et al. (2022) to be a KM giant star. Both G359.50-0.09 5 and G359.50-0.09 9 were found to have decreasing flux with increasing infrared wavelength, atypical of MYSOs, with the latter source also having SiO maser emission more typical of a AGB star. In all, 60% of the mid-infrared sources in G359.50-0.09 are MYSO Candidates, with the most massive being G359.50-0.09 4 with a mass of 32 $M_{\odot}$.

ORCID iDs

James M. De Buizer https://orcid.org/0000-0001-7378-4430
Wanggi Lim https://orcid.org/0000-0003-4243-6809
James T. Radomski https://orcid.org/0000-0003-0740-2259
Nicole Karnath https://orcid.org/0000-0003-3682-854X

References

An, D., Ramírez, S. V., Sellgren, K., et al. 2011, ApJ, 736, 133
Ao, Y., Henkel, C., Menten, K. M., et al. 2013, A&A, 550, A135
Araya, E. D., Olmi, L., Morales Ortiz, J., et al. 2015, ApJS, 221, 10
Bally, J., Crowe, S., Fedriani, R., et al. 2024, arXiv:2412.10983
Balser, D. S., Rood, R. T., Bania, T. M., & Anderson, L. D. 2011, ApJ, 738, 27
Benson, J. M., & Johnston, K. J. 1984, ApJ, 277, 181
Bieging, J., Downes, D., Wilson, T. L., Martin, A. H. M., & Guesten, R. 1980, A&AS, 42, 163
Blommaert, J. A. D. L., Groenewegen, M. A. T., Okumura, K., et al. 2006, A&A, 460, 555
Blum, R. D., Conti, P. S., & Damineli, A. 2000, AJ, 119, 1860
Bojičić, I. S., Parker, Q. A., Filipović, M. D., & Frew, D. J. 2011, MNRAS, 412, 223
Breen, S. L., Ellingsen, S. P., Contreras, Y., et al. 2013, MNRAS, 435, 524
Busso, M., Guandalini, R., Persi, P., Corcione, L., & Ferrari-Toniolo, M. 2007, AJ, 133, 2310
Cala, R. A., Gómez, J. F., Miranda, L. F., et al. 2022, MNRAS, 516, 2235
Caswell, J. L., & Haynes, R. F. 1987, A&A, 171, 261
Caswell, J. L., Fuller, G. A., Green, J. A., et al. 2010, MNRAS, 404, 1029
Cerrigone, L., Umana, G., Trigilio, C., et al. 2017, MNRAS, 468, 3450
Cho, S.-H., Yun, Y., Kim, J., et al. 2016, ApJ, 826, 157
Clark, J. S., Patrick, L. R., Najarro, F., Evans, C. J., & Lohr, M. 2021, A&A, 649, A43
Clarke, M., & Vander Vliet, R. 2023, FIA-USRA/sofia_redux: v1.3.3, Zenodo, doi:10.5281/ZENODO.8219569
Cohen, M., & Parker, Q. A. 2003, in IAU Symp. 209, Planetary Nebulae: Their Evolution and Role in the Universe, ed. S. Kwok, M. Dopita, & R. Sutherland (Cambridge: Cambridge Univ. Press), 33
Conti, P. S., & Crowther, P. A. 2004, MNRAS, 355, 899
Conti, P. S., & McCray, R. 1980, Sci, 208, 9
Cotera, A. S., Hankins, M. J., Bally, J., et al. 2024, ApJ, 973, 110
Cox, P., & Laureijs, R. 1989, in IAU Symp. 136, The Center of the Galaxy, ed. M. Morris (Cambridge: Cambridge Univ. Press), 121
Crowe, S., Fedriani, R., Tan, J. C., et al. 2024, arXiv:2410.09253
Cyganowski, C. J., Brogan, C. L., Hunter, T. R., & Churchwell, E. 2011, ApJ, 743, 56
Cyganowski, C. J., Whitney, B. A., Holden, E., et al. 2008, AJ, 136, 2391
De Buizer, J. M., Lim, W., Karnath, N., & Radomski, J. T. 2024, ApJ, 963, 55
De Buizer, J. M., Lim, W., Karnath, N., Radomski, J. T., & Bonne, L. 2022, ApJ, 933, 60
De Buizer, J. M., Lim, W., Liu, M., Karnath, N., & Radomski, J. T. 2021, ApJ, 923, 198
De Buizer, J. M., Lim, W., Radomski, J. T., & Liu, M. 2023, ApJ, 949, 82
De Buizer, J. M., & Vacca, W. D. 2010, AJ, 140, 196
Decin, L., Montargès, M., Richards, A. M. S., et al. 2020, Sci, 369, 1497
Downes, D., Goss, W. M., Schwarz, U. J., & Wouterloot, J. G. A. 1979, A&AS, 35, 1
Downes, D., Wilson, T. L., Bieging, J., & Wink, J. 1980, A&AS, 40, 379
Ferrière, K. 2009, A&A, 505, 1183
Forster, J. R., & Caswell, J. L. 2000, ApJ, 530, 371
Fujii, T., Deguchi, S., Ita, Y., et al. 2006, PASJ, 58, 529
Garay, G., Ramirez, S., Rodriguez, L. F., Curiel, S., & Torrelles, J. M. 1996, ApJ, 459, 193
Gatley, I., Becklin, E. E., Werner, M. W., & Harper, D. A. 1978, ApJ, 220, 822
Gaume, R. A., & Claussen, M. J. 1990, ApJ, 351, 538
Gaume, R. A., Claussen, M. J., de Pree, C. G., Goss, W. M., & Mehringer, D. M. 1995, ApJ, 449, 663
Gautier, T. N., Hauser, M. G., Beichman, C. A., et al. 1984, ApJL, 278, L57
Ginsburg, A., Henkel, C., Ao, Y., et al. 2016, A&A, 586, A50
Ginsburg, A., Bally, J., Barnes, A., et al. 2018, ApJ, 853, 171
González-Santamaría, I., Manteiga, M., Manchado, A., Ulla, A., & Dafonte, C. 2019, A&A, 630, A150
Green, J. A., Caswell, J. L., & McClure-Griffiths, N. M. 2015, MNRAS, 451, 74

Groenewegen, M. A. T. 2022, A&A, 659, A145
Gutermuth, R. A., Megeath, S. T., Myers, P. C., et al. 2009, ApJS, 184, 18
Hankins, M. J., Lau, R. M., Radomski, J. T., et al. 2020, ApJ, 894, 55
Harris, A. I., Güsten, R., Requena-Torres, M. A., et al. 2021, ApJ, 921, 33
Harvey, P. M., Campbell, M. F., & Hoffmann, W. F. 1977, ApJ, 211, 786
Henshaw, J. D., Barnes, A. T., Battersby, C., et al. 2023, in ASP Conf. Ser. 534, Protostars and Planets VII, ed. S. Inutsuka et al. (San Francisco, CA: ASP)
Hoffmann, W. F., Fredrick, C. L., & Emery, R. J. 1971, ApJL, 170, L89
Hrivnak, B. J. 2000, in ISO Beyond the Peaks: The 2nd ISO Workshop on Analytical Spectroscopy, ed. A. Salama et al., 191
Israel, F. P. 1980, A&A, 90, 246
Jang, D., An, D., Sellgren, K., et al. 2022, ApJ, 930, 16
Jones, D. I., Crocker, R. M., Ott, J., Protheroe, R. J., & Ekers, R. D. 2011, AJ, 141, 82
Jones, P. A., Burton, M. G., Cunningham, M. R., Tothill, N. F. H., & Walsh, A. J. 2013, MNRAS, 433, 221
Kainulainen, J., & Tan, J. C. 2013, A&A, 549, A53
Kauffmann, J., Pillai, T., Zhang, Q., et al. 2017, A&A, 603, A89
Kendrew, S., Ginsburg, A., Johnston, K., et al. 2013, ApJL, 775, L50
Knapp, G. R., Bowers, P. F., Young, K., & Phillips, T. G. 1994, ApJL, 429, L33
Koepferl, C. M., Robitaille, T. P., Morales, E. F. E., & Johnston, K. G. 2015, ApJ, 799, 53
Kramer, C., Staguhn, J., Ungerechts, H., & Sievers, A. 1998, in IAU Symp. 184, The Central Regions of the Galaxy and Galaxies, ed. Y. Sofue (Cambridge: Cambridge Univ. Press), 173
Kruijssen, J. M. D., Dale, J. E., & Longmore, S. N. 2015, MNRAS, 447, 1059
Kuchar, T. A., & Clark, F. O. 1997, ApJ, 488, 224
Lee, B., Giavalisco, M., Williams, C. C., et al. 2013, ApJ, 774, 47
Lim, W. 2019, Surveying the Giant HII Regions of the Milky Way with SOFIA, V5, Harvard Dataverse, doi:10.7910/DVN/POYMK5
Lim, W., & De Buizer, J. M. 2019, ApJ, 873, 51
Lim, W., De Buizer, J. M., & Radomski, J. T. 2020, ApJ, 888, 98
Lim, W., Tan, J. C., Kainulainen, J., Ma, B., & Butler, M. J. 2016, ApJL, 829, L19
Lis, D. C., & Carlstrom, J. E. 1994, ApJ, 424, 189
Lis, D. C., Carlstrom, J. E., & Keene, J. 1991, ApJ, 380, 429
Liszt, H. S., & Spiker, R. W. 1995, ApJS, 98, 259
Little, S. J., & Price, S. D. 1985, AJ, 90, 1812
Lu, X., Cheng, Y., Ginsburg, A., et al. 2020, ApJL, 894, L14
Lu, X., Mills, E. A. C., Ginsburg, A., et al. 2019a, ApJS, 244, 35
Lu, X., Zhang, Q., Kauffmann, J., et al. 2019b, ApJ, 872, 171
Lu, X., Li, S., Ginsburg, A., et al. 2021, ApJ, 909, 177
Mangilli, A., Aumont, J., Bernard, J. P., et al. 2019, A&A, 630, A74
Marini, E., Dell'Agli, F., Kamath, D., et al. 2023, A&A, 670, A97
Matthews, L. D., & Reid, M. J. 2007, AJ, 133, 2291
Mauerhan, J. C., Muno, M. P., Morris, M. R., Stolovy, S. R., & Cotera, A. 2010, ApJ, 710, 706
McGrath, E. J., Goss, W. M., & De Pree, C. G. 2004, ApJS, 155, 577
Mehringer, D. M., Goss, W. M., & Palmer, P. 1994, ApJ, 434, 237
Mehringer, D. M., & Menten, K. M. 1997, ApJ, 474, 346
Mehringer, D. M., Palmer, P., & Goss, W. M. 1993a, ApJL, 402, L69
Mehringer, D. M., Palmer, P., & Goss, W. M. 1995, ApJS, 97, 497
Mehringer, D. M., Palmer, P., Goss, W. M., & Yusef-Zadeh, F. 1993b, ApJ, 412, 684
Mehringer, D. M., Yusef-Zadeh, F., Palmer, P., & Goss, W. M. 1992, ApJ, 401, 168
Meng, F., Sánchez-Monge, Á., Schilke, P., et al. 2019, A&A, 630, A73
Meng, F., Sánchez-Monge, Á., Schilke, P., et al. 2022, A&A, 666, A31
Messineo, M., Habing, H. J., Sjouwerman, L. O., Omont, A., & Menten, K. M. 2002, A&A, 393, 115
Meynet, G. 1995, A&A, 298, 767
Mills, E. A. C., Ginsburg, A., Immer, K., et al. 2018, ApJ, 868, 7
Molinari, S., Schisano, E., Elia, D., et al. 2016, A&A, 591, A149
Morris, M., & Serabyn, E. 1996, ARA&A, 34, 645
Mücke, A., Koribalski, B. S., Moffat, A. F. J., Corcoran, M. F., & Stevens, I. R. 2002, ApJ, 571, 366
Nguyen, H., Rugel, M. R., Murugeshan, C., et al. 2022, A&A, 666, A59
Nogueras-Lara, F. 2024, A&A, 681, L21
Nogueras-Lara, F., Schödel, R., & Neumayer, N. 2022, NatAs, 6, 1178
Oka, T., & Geballe, T. R. 2022, ApJ, 927, 97
Oka, T., Hasegawa, T., Sato, F., Tsuboi, M., & Miyazaki, A. 1998, ApJS, 118, 455
Padovani, M., Marcowith, A., Sánchez-Monge, Á., Meng, F., & Schilke, P. 2019, A&A, 630, A72
Peeters, E., Martín-Hernández, N. L., Damour, F., et al. 2002, A&A, 381, 571
Portegies Zwart, S. F., Makino, J., McMillan, S. L. W., & Hut, P. 2001, ApJL, 546, L101
Pudritz, R. E. 2002, Sci, 295, 68
Reach, W. T., Rho, J., Tappe, A., et al. 2006, AJ, 131, 1479
Reid, M. J., Menten, K. M., Brunthaler, A., et al. 2014, ApJ, 783, 130
Reid, M. J., Menten, K. M., Zheng, X. W., Brunthaler, A., & Xu, Y. 2009, ApJ, 705, 1548
Ridley, M. G. L., Sormani, M. C., Treß, R. G., Magorrian, J., & Klessen, R. S. 2017, MNRAS, 469, 2251
Rinehart, S. A., Houck, J. R., Smith, J. D., & Wilson, J. C. 2002, MNRAS, 336, 66
Schultheis, M., Lançon, A., Omont, A., Schuller, F., & Ojha, D. K. 2003, A&A, 405, 531
Scoville, N. Z., Solomon, P. M., & Penzias, A. A. 1975, ApJ, 201, 352
Sevenster, M. N. 2002, AJ, 123, 2772
Shiki, S., Ohishi, M., & Deguchi, S. 1997, ApJ, 478, 206
Simpson, J. P., Colgan, S. W. J., Cotera, A. S., Kaufman, M. J., & Stolovy, S. R. 2018, ApJL, 867, L13
Simpson, J. P., Colgan, S. W. J., Cotera, A. S., Kaufman, M. J., & Stolovy, S. R. 2021, ApJ, 910, 59
Smith, L. F., Biermann, P., & Mezger, P. G. 1978, A&A, 66, 65
Sofue, Y. 2024, MNRAS, 532, 4187
Sormani, M. C., Gerhard, O., Portail, M., Vasiliev, E., & Clarke, J. 2022, MNRAS, 514, L1
Staguhn, J., Benford, D., Morris, M., & Uchida, K. 2004, in Proc. of the Cologne-Bonn-Zermatt Symp. 4, The Dense Interstellar Medium in Galaxies, ed. S. Pfalzner et al. (Berlin: Springer), 277
Suárez, O., Gómez, J. F., Miranda, L. F., et al. 2009, A&A, 505, 217
Suh, K.-W. 2024, JKAS, 57, 123
Sylvester, R. J., Kemper, F., Barlow, M. J., et al. 1999, A&A, 352, 587
Uscanga, L., Gómez, J. F., Suárez, O., & Miranda, L. F. 2012, A&A, 547, A40
Ventura, P., Dell'Agli, F., Lugaro, M., et al. 2020, A&A, 641, A103
Ventura, P., Dell'Agli, F., Schneider, R., et al. 2014, MNRAS, 439, 977
Volk, K., Kwok, S., Hrivnak, B. J., & Szczerba, R. 2002, ApJ, 567, 412
Volk, K., Xiong, G.-Z., & Kwok, S. 2000, ApJ, 530, 408
Walsh, A. J., Purcell, C. R., Longmore, S. N., et al. 2014, MNRAS, 442, 2240
Westbrook, W. E., Werner, M. W., Elias, J. H., et al. 1976, ApJ, 209, 94
Whitworth, A. P., Bhattal, A. S., Chapman, S. J., Disney, M. J., & Turner, J. A. 1994, A&A, 290, 421
Yusef-Zadeh, F., Arendt, R. G., Wardle, M., Heywood, I., & Cotton, W. 2022, MNRAS, 517, 294
Yusef-Zadeh, F., Hewitt, J. W., Arendt, R. G., et al. 2009, ApJ, 702, 178
Yusef-Zadeh, F., Wardle, M., Arendt, R., et al. 2024, MNRAS, 527, 1275
Zhang, Y., & Kwok, S. 2009, ApJ, 706, 252
Zhang, Y., & Tan, J. C. 2011, ApJ, 733, 55
Zinnecker, H., & Yorke, H. W. 2007, ARA&A, 45, 481